APPLIED COMPUTATIONAL ELECTROMAGNETICS SOCIETY JOURNAL

Special Issue on Electromagnetic Diffraction Modeling and Simulation

Guest Editor:
Levent Sevgi
Okan University, Istanbul

July 2017
Vol. 32 No. 7
ISSN 1054-4887

THE APPLIED COMPUTATIONAL ELECTROMAGNETICS SOCIETY

JOURNAL

TABLE OF CONTENTS

Electromagnetic Diffraction Modeling:
High Frequency Asymptotics vs. Numerical Techniques

Levent Sevgi

Department of Electrical and Electronics Engineering
Okan University, Tuzla Campus, Istanbul, 34959, Turkey
ls@leventsevgi.net

Abstract ─ Electromagnetic diffraction modelling and recent numerical simulation approaches, on the canonical 2D non-penetrable wedge scattering problem, are reviewed in this introduction paper.

Index Terms ─ Diffraction, electromagnetics, finite element method (FEM), geometric optics (GO), geometric theory of diffraction (GTD), method of moments (MoM), physical optics (PO), physical theory of diffraction (PTD), simulation, time domain finite difference method (FDTD), wave scattering.

I. INTRODUCTION

We have witnessed transformation from engineering electromagnetics to electromagnetic engineering [1-4]. This is merely because of technological developments we have had for the last two-three decades. Understanding and using electromagnetic theory has become a must in many engineering disciplines. One important topic is electromagnetic scattering, and diffraction is the most critical phenomena that has been investigated analytically and numerically for a long time [5-36].

Electromagnetic (EM) scattering from wave – object interactions using analytical solutions is limited to structures whose surfaces can be described by orthogonal curvilinear coordinates. Most of these solutions are in the form of infinite series, which are poorly convergent when the dimensions of the object are greater than a few wavelengths. Many practical scattering problems have no closed-form solutions. Because of this, high frequency asymptotic (HFA) techniques have been used when the dimensions of the scattering object are many wavelengths. Both ray-type *Geometrical Theory of Diffraction* (GTD) [5-8] and the wave- (i.e., induced-source)-based *Physical Theory of Diffraction* (PTD) [9-11] have received considerable attention in the past several decades. A short summary on HFA is given in [13].

Diffraction from a two-dimensional (2D) non-penetrable wedge is a canonical structure for all these HFA methods (see, Fig. 1). The source locations 1 and 2 belong to single-side (SSI) and double-side (DSI) illuminations, respectively. Note that, there is a shadow region for SSI where only diffraction fields exist. The two critical angles reflection-shadow boundary (RSB) and incident-shadow boundary (ISB) separate three regions. In Region I, incident, reflected, and diffracted fields exist. In Region II, only incident and diffracted fields exist. In Region III (i.e., in the shadow region) only diffracted fields exist. In the DSI scenario, there are two RSBs which separate regions with and without reflected fields.
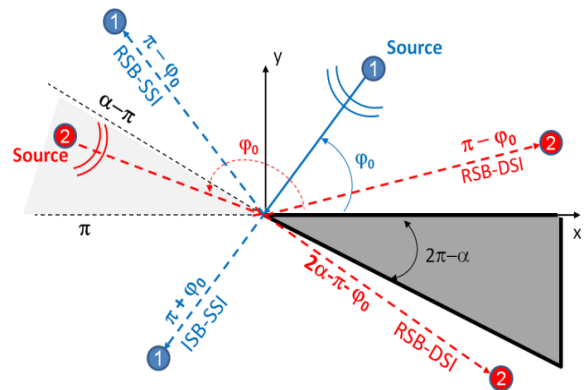
Fig. 1. Wedge scattering scenarios (1: single side illumination; 2: double side illumination).

In the case of acoustic waves, the two boundary conditions (BC) appropriate for the non-penetrable wedge are acoustically soft (SBC) and hard (HBC) wedges. In electromagnetics, they correspond to transverse magnetic (SBC $\rightarrow$ TM) and transverse electric (HBC $\rightarrow$ TE) cases, respectively. The field components used in these two cases, respectively, are the z-components of electric (E_z) and magnetic field (H_z) intensities. Mathematically, they are Dirichlet and Neumann BCs, respectively.

Wedge scattering has also been modeled with numerical models such as the Finite-Difference Time-Domain (FDTD) [16,17], Method of Moments (MoM)

[18-23], and Finite Element Method [33,34]. The following sections summarize these models and techniques with characteristic applications.

II. NUMERICAL MODELING OF DIFFRACTED WAVES

A. FDTD approach

Wedge scattering can be modeled with the FDTD method [20-28] and scattered, reflected and diffracted fields can be separated in both time and frequency domains. Early approaches were based on the separation of incident, reflected, and diffracted pulses in the time domain using time-gating approach [20-22].

The methods discussed in [23-29] use multi-step techniques in separation of both diffracted and fringe fields as pictured in Fig. 2. Here, scenario (a) yields total fields; incident, reflected, and diffracted field components in Region I; incident and diffracted field components in Region II; and only the diffracted fields in Region III.
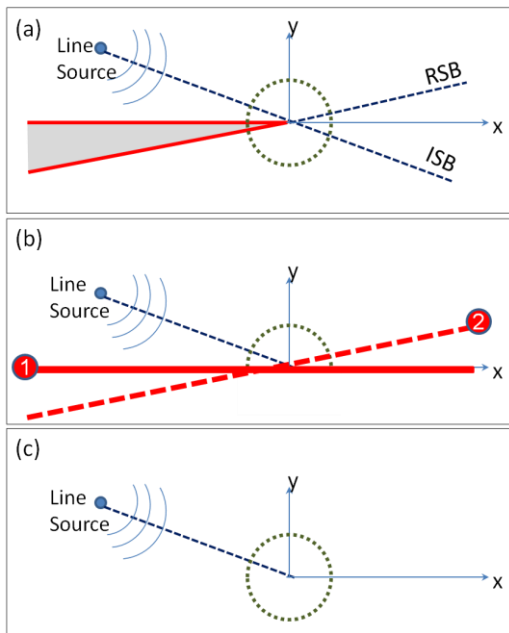
Fig. 2. Multi-step FDTD-based diffraction approach: (a) the wedge scenario, (b) infinite-plane problem, and (c) free-space scenario [25].

Scenario (b) in the figure is the infinite-plane scenario ($\alpha = 180°$, Plane-1) which yields total fields on the upper half plane ($0 \le \varphi < \pi$). Since there is no edge or tip, the total fields include only incident and reflected fields; and do not contain diffracted fields. Finally, scenario (c) yields only the incident fields in the free-space.

The FDTD simulation is run separately for each of these three scenarios and time-domain data are recorded. Subtracting the time data of the second scenario from the first scenario in Region I ($0 \le \varphi < \pi - \varphi_0$); and the time data of the third scenario from the first scenario in Region II ($\pi - \varphi_0 \le \varphi < \pi + \varphi_0$) will yield diffracted-only fields all around the wedge [23-25].

B. MoM approach

Diffracted fields can also be obtained with the two-step MoM approach as introduced in [30-32]. Figure 3 shows the two (i.e., the wedge and infinite-plane) scenarios used for this purpose.

MoM is a general procedure and frequency domain approach for solving linear equations. Many problems that cannot be solved exactly can be solved approximately by this method. It has been applied to a broad range of EM problems since the publication of the book by Harrington [37]. A useful tutorial has just been published [38]. MoM is a semi-analytical-numerical model which needs the Green's function solution of the problem at hand.
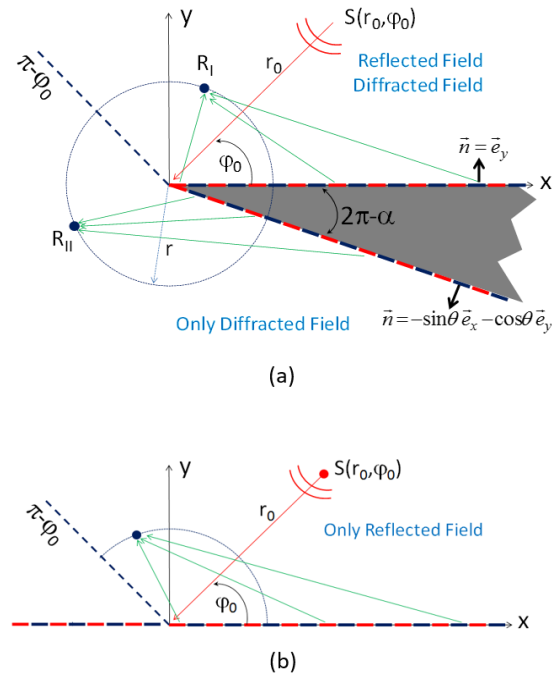
Fig. 3. The two-step MoM-based diffraction approach: (a) the wedge scenario, and (b) infinite-plane problem [30].

The two-step MoM approach [30] is applied as follows. In Fig. 3 (a), incident fields are injected analytically, therefore MoM solutions directly yield the scattered fields which contains reflected and diffracted fields. The MoM solution of the half-plane scenario in Fig. 3 (b) yields the reflected fields in the region

up to the critical angle $\varphi = \pi - \varphi_0$. During the MoM implementation of the wedge scattering first, incident fields upon segments are calculated using the Green's function of the problem and the impedance matrix is formed. Then 2N by 2N matrix system is solved and source-induced segment currents are obtained. Finally, scattered fields on the chosen observation points are calculated from the superposition of segment radiations using the Green's function. Total fields are obtained by adding the direct wave from the source to the receiver. The diffracted-only fields can be obtained using the MoM procedure if reflected fields in ($0 \le \varphi < \pi - \varphi_0$) are subtracted. The reflected fields in this region) can be obtained with the scenario in Fig. 3 (b).

C. FEM approach

Field components around the 2D non-penetrable wedge can also be extracted via FEM [33-34]. FEM is a variational method that is developed for approximate solution of boundary value problems governed by partial differential equations. It has been widely used due to its flexibility in handling arbitrary geometries and material non-homogeneities.

Consider, the wedge problem in Fig. 4 (a). The open-region of the computational domain is terminated by PML blocks. The dotted observation circle represents the positions of receivers all of which will record the scattered fields. The three-step diffracted field extraction is as follows:

(i) FEM is run for the structure in Fig. 4 (a) and the scattered fields are recorded on the observation circle.

(ii) FEM is run for the problem in Fig. 4 (b), where the right edge of the object is extended over the vertical direction, and the scattered fields are recorded only on the blue-dotted part of the observation circle. These fields correspond to the reflected fields from the top face of the wedge.

(iii) The same is repeated for the problem in Fig. 4 (c) and fields reflected from the bottom face of the wedge are obtained.

Finally, the diffracted field is obtained by subtracting the fields in steps (ii) and (iii) from the scattered fields in step (i).

III. NUMERICAL MODELING OF FRINGE WAVES

Electromagnetic and/or acoustic waves interact with objects and induce surface currents. These surface currents contain both uniform (PO) and non-uniform (PTD) currents if there is an edge and/or tip. The non-uniform currents are called fringe currents and fields generated by these currents are called fringe fields. In order to calculate fringe waves, one needs to separate source-induced non-uniform and uniform currents.
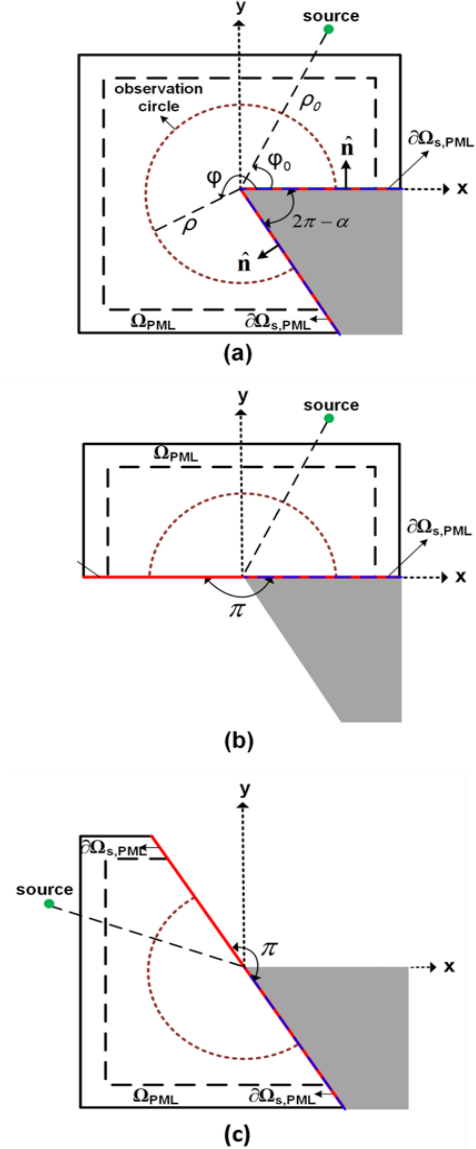
Fig. 4. FEM-based diffraction modeling: (a) original geometry, (b) modified geometry for obtaining the PO currents for SSI, and (c) modified geometry for obtaining the PO currents for SSI [34].

Fringe currents can be extracted with all these three methods (FDTD [29], MoM [31], and FEM [35]) by using similar multi-step procedures. First, standard procedures are applied to the wedge problem and surface currents are obtained. The currents on the illuminated face of the wedge contain both uniform and non-uniform currents; only non-uniform currents exist on the shadow face. Then, infinite-plane scenario is used and (since there is no edge or tip type discontinuity) only uniform currents are obtained. Subtracting (that part of corresponding) infinite-plane currents from the

illuminated face wedge currents yields the non-uniform currents on the top face. The bottom face of the wedge already has non-uniform currents. The scattered waves superposed using non-uniform currents then yield the fringe waves.

Note that, the infinite-plane scenario must be repeated for the other face of the wedge for the DSI in both diffracted and fringe field simulations.

IV. NUMERICAL EXAMPLES

The tutorial in [15] summarizes HFA models and the MATLAB based virtual diffraction tool presented in [16] can be used to visualize total and diffracted fields around a 2D non-penetrable wedge. The front panel of this virtual tool is shown in Fig. 5.
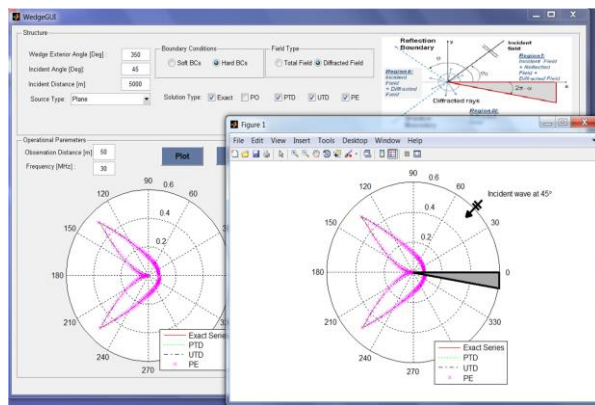
Fig. 5. The front panel of the WedgeGUI tool [16].

The top block of the panel is reserved for the structure. The wedge figure is shown on the top right. The wedge exterior angle, incident distance/angle are supplied on the top left. The user also selects either of the Soft and Hard BCs; total and diffracted fields in this block. A pop-up menu allows the user to choose a plane wave or a line source excitation. For each source type the methods used in simulations are given with tick boxes. Multiple selection is possible. An example generated with this tool is given in Fig. 6. Here, total and diffracted fields for both SBC and HBC cases are shown.

The next examples belong to numerical techniques. In Fig. 7, electromagnetic scattering around a 60°-wedge with non-penetrable boundaries is shown.

Here, MoM results are compared with HFA results. On the left, total fields around the wedge is presented. On the right, only diffracted fields are plotted. The angle of incidence is 60°; this corresponds to SSI.

As observed in the total fields plot, strong interference occurs between incident and reflected fields and lobes are formed. The total field on the shadow region only contains diffracted fields. As observed in

the diffracted fields plot, maximum diffraction occurs along the two critical angles.
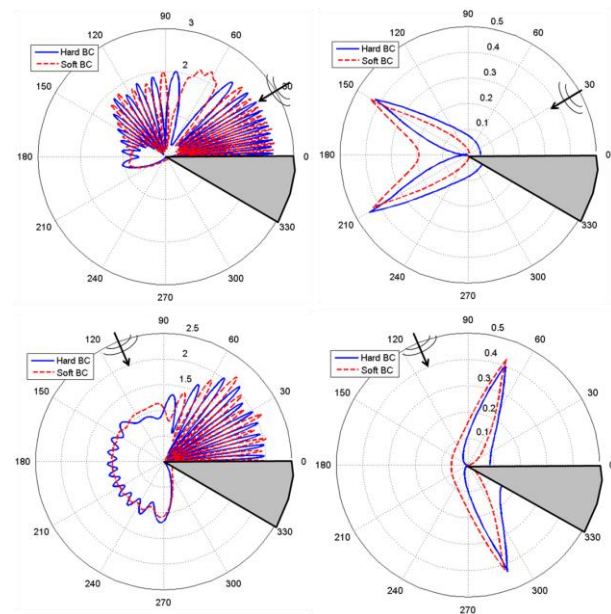
Fig. 6. EM scattering around a 30°-wedge, (Left) total fields, (Right) diffracted fields (r=5λ, kr=31.4).
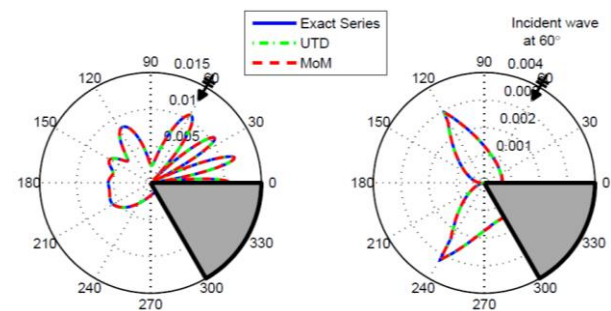
Fig. 7. EM scattering around a 60°-wedge, (Left) total fields, (Right) diffracted fields (TE/HBC case). The receivers are located on a circle around the wedge with radius r=2λ. Plane wave excitation is used [30].

Figure 8 belongs to the same wedge with similar comparisons but for DSI. Here, φ_0=150° and r=2λ. The results belong to HFA, MoM, and FDTD simulations. As observed, there is a perfect agreement among the results.

Fringe waves represent the part of the total edge-diffracted waves generated by source-induced fringe surface currents. These waves can be generated directly using fringe currents. Fringe fields around a 60°-wedge for both SBC and HBC cases are plotted in Fig. 9. Here, only PTD and MoM results are given for a clear visualization.
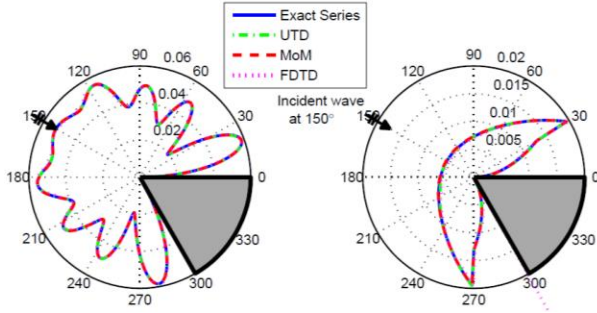
Fig. 8. EM scattering around a 60°-wedge, (Left) total fields, (Right) diffracted fields (TE/HBC case). Plane wave excitation is used [30].
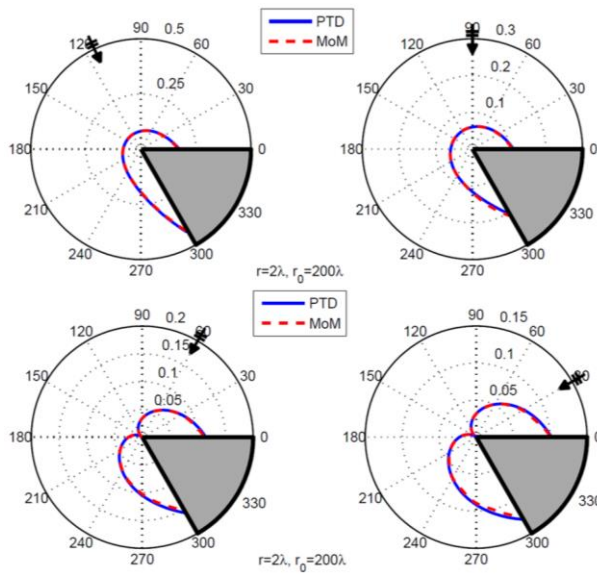
Fig. 9. Fringe fields vs. angle around a 60°-wedge. (Top) TM/SBC case, (Bottom) TE/HBC case. A line source excitation is used [31].

The last example in Fig. 10 belongs to fringe fields around a 30°-wedge with non-penetrable hard boundaries. All the methods are used here. As observed, PTD, MoM, FDTD, and FEM results agree very well; the incorrect result belongs to MTPO [36].

Note that, the free virtual tools presented in [26] (based on FDTD method), [30] and [32] (based on MoM) can also be used to visualize EM scattering around the 2D non-penetrable wedge comparatively.

V. CONCLUSION

Understanding electromagnetic wave scattering is critical in many applications, especially in designing reliable surveillance systems and low visible air and surface targets. This used to be done using approximate analytical models such as GO, GTD, UTD and PO, PTD, widely known as high frequency asymptotics.
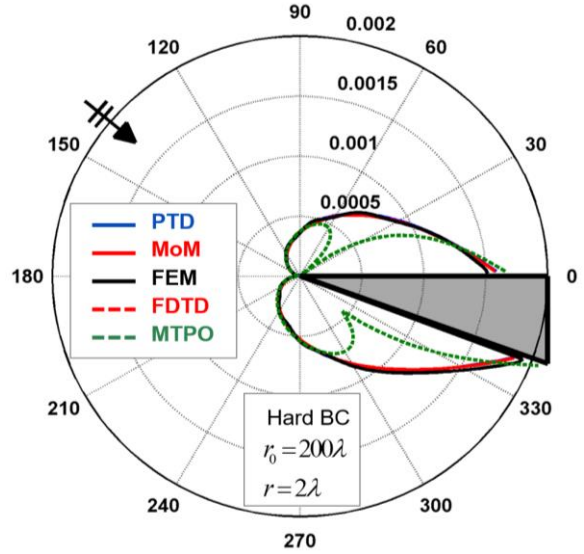
Fig. 10. Fringe fields vs. angle around a 30°-wedge (TE/HBC case).

The GO can model reflections and refractions but fails to account for the field intensity in shadow regions. GTD describes diffraction everywhere except at and near incidence and reflection shadow transitions; UTD removes the discontinuities along these shadow boundaries. However, GO/GTD/UTD fails near caustics. The PTD supplements PO to provide corrections that are due to diffractions at edges of conducting surfaces. Ufimtsev suggested the existence of nonuniform (*fringe*) edge currents in addition to the uniform physical optics surface currents.

Note that, GO/GTD/UTD is simple to apply, can be used to solve complicated problems that do not have exact solutions, provides physical insight into the radiation and scattering mechanisms from the various parts of the structure and can be combined with other techniques, such as MoM, to form a hybrid method. On the other hand, PO/PTD provides correctly only the first asymptotic terms for main components of the scattered field in 3D problems, allows constructing relatively simple solutions of various practical problems, provides uniform asymptotics for the scattered field which are valid both in the ray regions and in the vicinity of foci and caustics, clarifies the physical structure of the scattered field, establishes the diffraction limit of reduction of scattering by absorbing coatings, and can be utilized to develop efficient hybrid techniques.

Parallel to the use of high speed, huge memory computers, novel numerical models have also begun to be used in scattering modeling. Recent studies have focused on the identification and isolation of diffracted and fringe wave components using well-known numerical models such as FDTD, MoM, and FEM. The

use and success of these numerical models are promising in modeling and simulation realistic objects in 3D.

REFERENCES

[1] L. B. Felsen and L. Sevgi, "Electromagnetic engineering in the 21st century: Challenges and perspectives," (introductory paper) Special issue of *ELEKTRIK, Turkish J. of Electrical Engineering and Computer Sciences*, vol. 10, no. 2, pp. 131-145, Feb. 2002.

[2] L. Sevgi, "Virtual tools/labs in electrical engineering education," *ELEKTRIK, Turkish J. of Electrical Engineering and Computer Sciences* (Special issue on Electrical and Computer Engineering Education in the 21st Century: Issues, Perspectives and Challenges), vol. 14, no. 1, pp. 113-127, 2006.

[3] L. Sevgi, "Electrical and computer engineering education in the 21st century: Issues, perspectives and challenges: Preface," *ELEKTRIK, Turkish J. of Electrical Engineering and Computer Sciences*, vol. 14, no. 1, pp. 1-5, 2006.

[4] L. Sevgi, "From engineering electromagnetics towards electromagnetic engineering," *ELEKTRIK, Turkish Journal of Electrical Engineering and Computer Sciences*, vol. 16, no. 1, pp. i-v, Jan. 2008.

[5] F. M. Grimaldi, *Physico-Mathesis de Lumine, Coloribus at Iride*. Bonomiae, 1665.

[6] J. B. Keller, "Diffraction by an aperture," *J. Appl. Phys.*, vol. 28, no. 4, pp. 426-444, 1957.

[7] J. B. Keller, "Geometrical theory of diffraction," *J. Opt. Soc. Amer.*, vol. 52, no. 2, pp. 116-130, 1962.

[8] R. G. Kouyoumjian and P. H. Pathak, "A uniform geometrical theory of diffraction for an edge in a perfectly conducting surface," *Proc. IEEE*, vol. 62, no. 11, pp. 1448-1461, 1974.

[9] P. Y. Ufimtsev, "Approximate computation of the diffraction of plane electromagnetic waves at certain metal bodies," *Sov. Phys.—Tech. Phys.*, pp. 1708-1718, 1957.

[10] P. Y. Ufimtsev, "Method of edge waves in the physical theory of diffraction," *Moscow, Soviet Radio*, 1962; translated into English by the US Air Force, Foreign Technology Division (National Air Intelligence Center), Wright-Patterson Air Force Base, OH, 1971, Technical Report AD 733203, Defense Technical Information Center of USA, Cameron Station, Alexandria, VA, 22304-6145, USA.

[11] P. Y. Ufimtsev, *Fundamentals of the Physical Theory of Diffraction*. Hoboken, New Jersey, John Wiley & Sons, Inc., USA, 1st ed. 2007, 2nd ed. 2014.

[12] A collection of papers on diffraction modeling,

[13] C. Balanis, L. Sevgi, and P. Y Ufimtsev, "Fifty years of high frequency asymptotics," *International Journal on RF and Microwave Computer-Aided Engineering*, vol. 23, no. 4, pp. 394-402, July 2013.

[14] L. Sevgi, *Electromagnetic Modeling and Simulation*. IEEE Press – John Wiley (EM Wave Series), NJ, Apr. 2014.

[15] F. Hacivelioglu, L. Sevgi, and P. Y. Ufimtsev, "Electromagnetic wave scattering from a wedge with perfectly reflecting boundaries: Analysis of asymptotic techniques," *IEEE Antennas and Propagation Magazine*, vol. 53, no. 3, pp. 232-253, June 2011.

[16] F. Hacıvelioğlu, M. A. Uslu, and L. Sevgi, "A Matlab-based simulator for the electromagnetic wave scattering from a wedge with perfectly reflecting boundaries," *IEEE Antennas and Propagation Magazine*, vol. 53, no. 6, pp. 234-243, Dec. 2011.

[17] F. Hacıvelioğlu, L. Sevgi, and P. Y. Ufimtsev, "Numerical evaluation of diffraction formulas for the canonical wedge scattering problem," *IEEE Antennas and Propagation Magazine*, vol. 55, no. 5, pp. 257-272, Oct. 2013.

[18] F. Hacıvelioğlu, L. Sevgi, and P. Y. Ufimtsev, "Backscattering from a soft-hard strip: Primary edge waves approximation," *IEEE Antennas and Wireless Propagation Letters*, vol. 12, pp. 249-252, 2013.

[19] F. Hacivelioglu, L. Sevgi, and P. Y. Ufimtsev, "Wedge diffracted waves excited by a line source: Exact and asymptotic forms of fringe waves," *IEEE Trans. Antennas Propagat.*, vol. 61, no. 9, pp. 4705-4712, 2013.

[20] G. Apaydın, F. Hacivelioglu, L. Sevgi, and O. Ufimtsev, "Fringe waves from a wedge with one face electric and the other face magnetic," *IEEE Trans on Antennas and Propagat.*, vol. 64, no. 3, pp. 1125-1130, Mar. 2016.

[21] G. Apaydin, F. Hacivelioglu, L. Sevgi, W. B. Gordon, and P. Y. Ufimtsev, "Diffraction at a rectangular plate: First-order PTD approximation," *IEEE Trans on Antennas and Propagat.*, vol. 64, no. 5, pp. 1891-1899, May 2016.

[22] G. Stratis, V. Anantha, and A. Taflove, "Numerical calculation of diffraction coefficients of generic conducting and dielectric wedges using FDTD," *IEEE Trans. Antennas and Propagat.*, vol. 45, no. 10, pp. 1525-1529, 1997.

[23] V. Anantha and A. Taflove, "Calculation of diffraction coefficients of three-dimensional infinite conducting wedges using FDTD," *IEEE Trans. Antennas and Propagat.*, vol. 46, no. 11, pp.

1755-1756, Nov. 1998.

[24] V. Anantha and A. Taflove, "Efficient modeling of infinite scatterers using a generalized total-field/ scattered field FDTD boundary partially embedded within PML," *IEEE Trans. Antennas and Propagat.*, vol. 50, no. 10, pp. 1337-1349, Oct. 2002.

[25] G. Cakir, L. Sevgi, and P. Y. Ufimtsev, "FDTD modeling of electromagnetic wave scattering from a wedge with perfectly reflecting boundaries: Comparisons against analytical models and calibration," *IEEE Trans. Antennas Propagat.*, vol. 60, no. 7, pp. 3336-3342, July 2012.

[26] M. A. Uslu and L. Sevgi, "Matlab-based virtual wedge scattering tool for the comparison of high frequency asymptotics and FDTD method," *Int. Journal on Applied Computational Electromagnetics*, vol. 27, no. 9, pp. 697-705, Sep. 2012.

[27] A. Uslu, G. Apaydın, and L. Sevgi, "Double-tip diffraction modeling: Finite difference time domain vs. method of moments," *IEEE Trans on Antennas and Propagat.*, vol. 62, no. 12, pp. 6337-6343, Dec. 2014.

[28] A. Uslu, G. Apaydın, and L. Sevgi, "Diffraction modeling by a soft-hard strip using finite difference time domain method," *IEEE Antennas and Wireless Propagation Letters*, vol. 15, 2016.

[29] A. Uslu, G. Apaydın, and L. Sevgi, "Finite difference time domain modeling of fringe waves," *ACES, Int. Journal on Applied Computational Electromagnetics*, vol. 32, This issue, pp. xxx-xxx, 2017.

[30] G. Apaydın and L. Sevgi, "A novel wedge diffraction modeling using method of moments," *ACES, Int. Journal on Applied Computational Electromagnetics*, vol. 30, no. 10, pp. 1053-1058, Oct. 2015.

[31] G. Apaydin, F. Hacivelioglu, L. Sevgi, and P. Y. Ufimtsev, "Wedge diffracted waves excited by a line source: Method of moments (mom) modeling of fringe waves," *IEEE Trans. Antennas Propagat.*, vol. 62, no. 8, pp. 4368-4371, Aug. 2014.

[32] G. Apaydin and L. Sevgi, "Two-dimensional non-penetrable wedge scattering problem and a MATLAB-based fringe wave calculator," *IEEE Antennas and Propagation Magazine*, vol. 58, no. 2, pp. 86-93, Apr. 2016.

[33] G. Apaydın, L. Sevgi, and P. Ufimtsev, "Fringe integral equations for the 2D wedge with soft and hard boundaries," *Radio Science*, vol. 51, no. 10, pp. 1570-1578, Oct. 2016.

[34] O. Ozgun and L. Sevgi, "Double-tip diffraction modeling: Finite element modeling (FEM) vs. uniform theory of diffraction (UTD)," *IEEE Trans. on Antennas and Propagat.*, vol. 63, no. 6, pp. 2686-2693, June 2015.

[35] O. Ozgun and L. Sevgi, "Finite element modeling of fringe waves in wedge diffraction problem," *IEEE Antennas and Wireless Propagation Letters*, vol. 15, 2016.

[36] F. Hacıvelioğlu, L. Sevgi, and P. Y. Ufimtsev, "On the modified theory of physical optics," *IEEE Trans. on Antennas and Propagat.*, vol. 61, no. 12, pp. 6115-6119, Dec. 2013.

[37] R. F. Harrington, *Field Computation by Moment Method*. New York: IEEE Press, 1993.

[38] E. Arvas and L. Sevgi, "A tutorial on the method of moments," *IEEE Antennas Propag. Mag.*, vol. 54, no. 3, pp. 260-275, June 2012.

Levent Sevgi (FIEEE) received his B.S., M.S., and Ph.D. degrees from Istanbul Technical University (İTU) in 1982, 1984, and 1991, respectively. He completed his Ph.D. studies in Brooklyn Poly, New York under the supervision of Prof. Dr. Leopold B. Felsen during 1988-1990.

He was with İTU, Istanbul (1991–1998); TUBITAK-MRC, Marmara Research Center, Turkey (1999–2000); Weber Research Institute, Polytechnic University of New York (1988–1990); Raytheon Systems, Canada (1998–1999); Center for Defense Studies, ITUV-SAM (1993–1998 and (2000–2002), DOĞUŞ University (2001–2014); University of Massachusetts - UMASS (2012–2013). He has been with OKAN University, Istanbul since Sep. 2014.

He has involved with complex electromagnetic (EM) problems and systems for nearly three decades and published several books, nearly 180 research papers/tutorials and more than 100 conference papers.

He is the author of the books entitled *Complex Electromagnetic Problems and Numerical Simulation Approaches* (2003) and *Electromagnetic Modeling and Simulation* (2014), published by the IEEE Press - John Wiley, and *A Practical Guide to EMC Engineering* (2017), published by ARTECH House.

Computational Design of Optical Couplers for Bended Nanowire Transmission Lines

Yunus Emre Tunçyürek, Barışcan Karaosmanoğlu, and Özgür Ergül

Department of Electrical and Electronics Engineering
Middle East Technical University, Ankara, Turkey
{bariscan,tuncyurek.emre,ozergul}@metu.edu.tr

Abstract ─ We present computational analysis, optimization, and design of optical couplers that can be useful to improve the transmission along bended nanowires. After demonstrating the deteriorated energy transmission due to sharp bends, which lead to out-of-phase nanowires and diffraction, we use a rigorous simulation environment to design efficient couplers made of spherical particles. For this purpose, an optimization module based on genetic algorithms is combined with the multilevel fast multipole algorithm, leading to a full-wave environment for precise designs of couplers. Numerical examples involving silver nanowires are presented to demonstrate the effectiveness of the optimization mechanism.

Index Terms ─ Genetic algorithms, multilevel fast multipole algorithm, nanowires, optical couplers, surface integral equations.

I. INTRODUCTION

Their favorable properties that allow controlling and guiding optical waves make nanowires an important class of popular ingredients of nano-optical systems [1]–[14]. Thanks to plasmonic properties of metals at optical frequencies, nanowires provide an excellent ability to transfer electromagnetic energy to long distances with respect to wavelength [3]. Hence, they are naturally used in a plethora of applications, such as sensing [1], energy harvesting, and optical imaging [5],[7]. As in all areas of electromagnetics, computational studies [12]–[14] are performed hand in hand with analytical and experimental work in order to develop alternative configurations of nanowire systems, leading to improved designs with better optical responses. Today, nanotechnology allows for the fabrication of less defective nanowires and their highly ordered arrangements for achieving ideal structures that were considered to be only theoretical a decade ago.

When a nanowire system is used as a transmission line, the electromagnetic energy is transmitted via surface plasmon polaritons. At the end of the line, the energy is assumed to be coupled to another system [6], or to free space, where radiation occurs from the tips of the nanowires [3]. In an optical system, depending on the application, it may be required to bend the transmission line. Then, similar to their counterparts at microwave frequencies, reflections may occur from the bends, reducing the amount of energy transferred. But, since the nanowires are not closed systems and the energy is mainly carried on the nanowire-air interfaces, diffraction at the bending locations becomes an important problem that further reduces the efficiency of the transmission [8]. As shown in this paper, smooth bends improve the transmission; but a large radius of curvature (ROC) may be required for a sufficient transmission. In addition, curving nanowires may bring additional challenges in the fabrication processes. At the same time, a large ROC wastes an area around bend and it is desirable to use a coupler that allow for efficient transmission even for sharply bended nanowires.

This study is devoted to the design of optical couplers for bended nanowire transmission lines. By using an array of spherical particles at the bend locations, we are able to increase the transmission through 90º corners without implementing any curves. The structure of the coupler is optimized via genetic algorithms (GAs) supported by fast and accurate solutions using the multilevel fast multipole algorithm (MLFMA) [15],[16]. In the next section, we briefly provide the details of the developed simulation and optimization environment. Section III presents the optimization parameters and numerical results, demonstrating the effectiveness of the optimizations. The paper ends with our concluding remarks in Section IV.

II. SIMULATION AND OPTIMIZATION ENVIRONMENT

We consider metallic objects, i.e., nanowires and couplers, located in free space at optical frequencies. The transmission problems are solved in frequency domain assuming time-harmonic sources in steady state. The major components of the solver and the optimization mechanism can be summarized as follows.
- Metals are modeled as homogeneous plasmonic objects using frequency-dependent complex perm

values with negative real parts. Surfaces are discretized by using triangular meshes. Electric and magnetic current densities are expanded via standard Rao-Wilton-Glisson functions. For accurate solutions, a modified combined tangential (MCTF) [17] is used, which provides accurate solutions of metallic objects in wide ranges of optical frequencies.

- Iterative Krylov-subspace algorithms are used to solve the dense matrix equations derived from the discretized MCTF. Matrix-vector multiplications are performed efficiently by using MLFMA [15], that is developed particularly for plasmonic structures [18]. Iterative solutions are accelerated by using a nested scheme employing MLFMA and its approximate forms. All interactions (matrix elements) and near-zone calculations are performed with two digits of accuracy (1% maximum error).

- GAs are used to optimize the couplers involving spherical plasmonic particles. On/off optimizations are performed by removing or keeping the particles to maximize the cost function. Hence, binary chromosomes involving 0 (off/remove) and 1 (on/keep) bit values are used so that the chromosome length corresponds to the number of initial particles in the coupler. An in-house implementation of GAs, employing hybrid selection, success-based mutations, and family elitism, is used for efficient optimizations.

- The GA implementation is combined efficiently with the solver module based on MLFMA. Two different kinds of combinations are considered, depending on the size of the problems. In a black-box combination, the GA module requires the evaluation of each individual, which is considered to be an independent electromagnetic problem. In an integrated combination, the setup computations for the full problem is performed before the optimization starts, and each evaluation is achieved by row/column deletion on the full matrix equation. In both cases, a dynamic accuracy control for MLFMA [19] can be used to further accelerate the optimizations by using less accurate solutions in initial GA pools.

More details of the solver and optimization modules can be found in [19],[20].

III. NUMERICAL RESULTS

Figure 1 depicts the scenario considered in this paper. Transmission lines involving pairs of silver (Ag) nanowires are considered at 250 THz. At this frequency, the relative permittivity of Ag is approximately $-60.8 + 4.31i$ [21], while it is assumed to be non-magnetic.
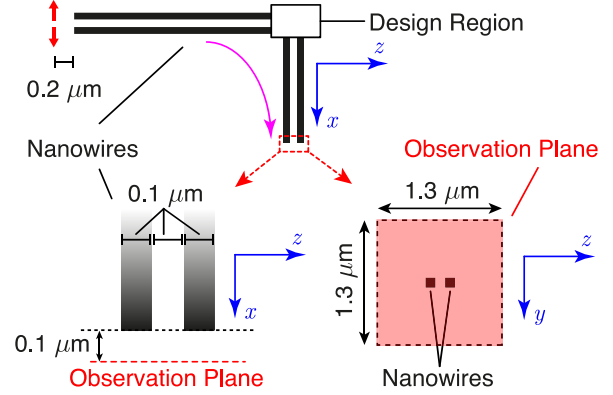
Fig. 1. The transmission scenario considered in this paper.

The nanowires have 0.1×0.1 µm square cross sections, while the surface-to-surface distance between them is also set to 0.1 µm. Without bending, each transmission line involves a horizontal part (in the z direction) of approximately 20 µm that is connected to a vertical part (in the x direction) of approximately 20 µm, leading to a total length of around 40 µm (approximately 33λ, where λ is the wavelength in free space). The couplers are designed as two-dimensional arrays of spherical Ag particles located at the intersection locations. The spheres are identical with a diameter of 90 nm. When using the couplers, the horizontal and vertical parts are connected sharply with 90º corners. For benchmarking, we also consider curved bends with various ROC values, while no coupler is used in these cases. As also depicted in Fig. 1, each transmission line is excited by a pair of dipoles (with unit dipole moments, i.e., 1 Am strengths) located symmetrically on the left-hand side with 0.2 µm distance from the nanowires. The output region is defined at the bottom end of the vertical nanowires. Specifically, sampling points on 1.3×1.3 µm planes with 0.1 µm distance from the nanowires are used to assess the transmission capabilities of the nanowires systems.

First, we consider the performances of curved connections, in comparison to the 90º sharp connection. Figure 2 presents the electric-field intensity (magnitude in dBV/m) and the power density (magnitude in dBW/m²) at around the transmission lines. The power density is calculated as:

$$S = \frac{1}{2} E \times H^*, \tag{1}$$

where E and H represents the electric field intensity and the magnetic field intensity, respectively. The dynamic ranges are selected as 40 dB and 20 dB for the field and power, respectively, for a comparative visualization. The

dipoles are clearly visible on the left-hand sides, where strong coupling to the nanowires is also observed. Diffraction occurs due to bending in all cases, while it becomes less localized as ROC increases from 0.3 μm to 10 μm. A comparison of the field and power values at the output sides reveals that the transmission is very low for the 90º sharp case, i.e., the power density in the vicinity of the nanowires at the output is less than 20 dB in this case. Then, as ROC increases and bending becomes smoother, the transmission improves progressively. While this is expected, we note that the quality of the transmission deteriorates due to the negative effects of the diffraction, as well as the phase mismatch between the nanowires. These contributions can be difficult to be isolated; but, they are modeled precisely using a full-wave solver.
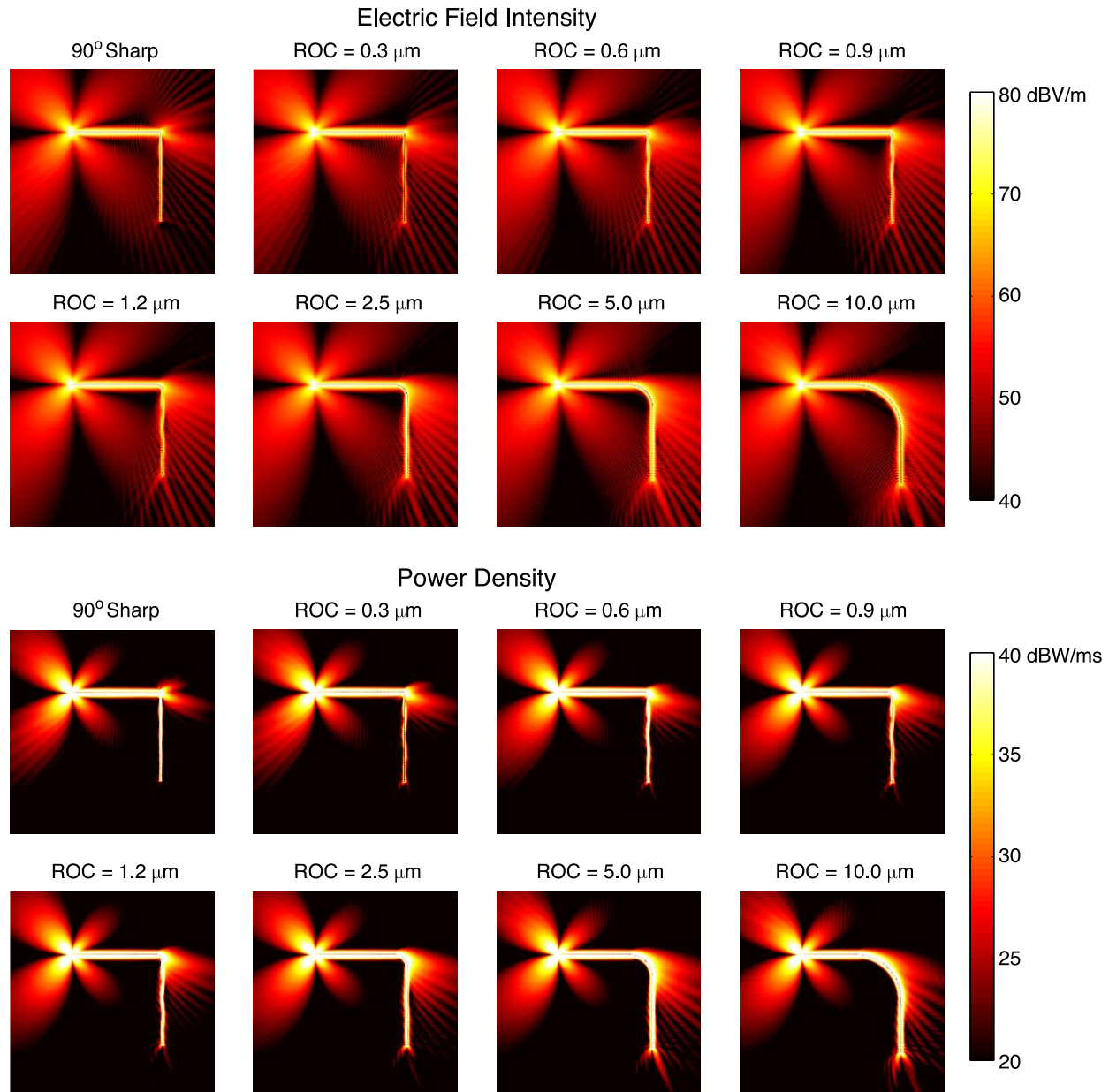
Fig. 2. The electric field intensity and power density at around the curved transmission lines with various values of ROC, in addition to the 90º sharp bending case.

For a detailed comparison of the curved transmission lines, Fig. 3 present the magnitudes of the electric field intensity (dBV/m), magnetic field intensity (dBA/m), and power density (dBW/m²) on the output plane described in Fig. 1. Our observations are in consistent with the discussion above, i.e., the transmission clearly improves

as ROC increases. Considering the power density plots, a small spot of values at around 35 dB is visible for the sharp case, while it evolves into a much larger spot with values more than 45 dB as ROC becomes 10 μm. It is

remarkable that, in addition to the larger output values, increasing ROC leads to more symmetric output patterns, as a demonstration of improved transmission quality.
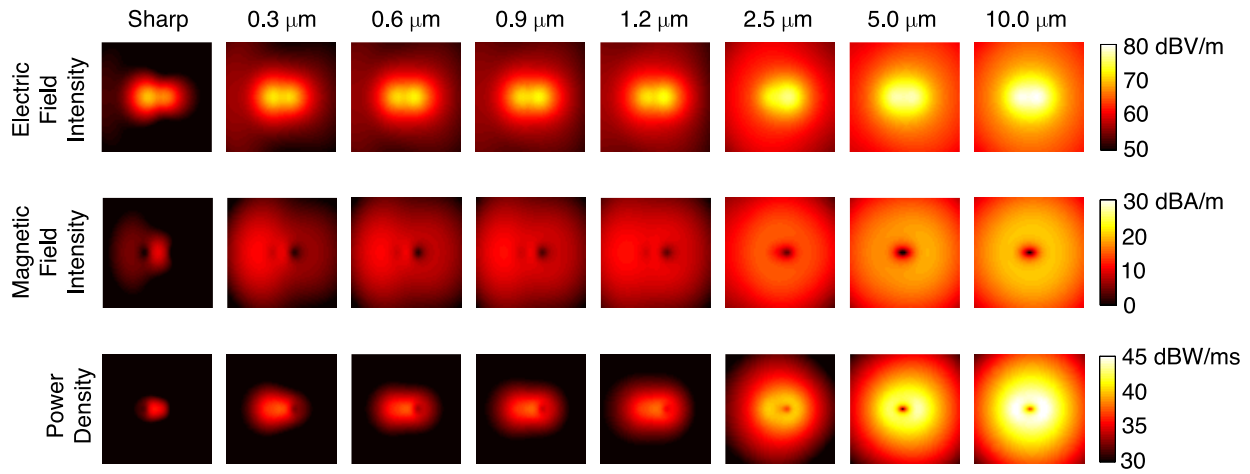
Fig. 3. The electric field intensity, magnetic field intensity, and power density at the outputs (see Fig. 1) of the transmission lines with various values of ROC, in addition to the 90° sharp bending case.

Following the benchmark on curved transmission lines, we consider the design of couplers for improving the transmission through sharp corners. Two-dimensional arrays of 139 or 143 spherical particles, which are also made of Ag, are placed at the corner locations enclosing the nanowires. Specifically, a 13×13 grid is used, while the particles corresponding to the nanowire locations are simply omitted. Optimizations are performed in the MATLAB environment. As the cost function, we select the average power density to be maximized on the 1.3×1.3 μm output planes. In the following, we present the results for three types of optimizations.

- The full model, discretized with around 91,314 unknowns, is considered. Using pools of 40 individuals (40 solutions per generation), it takes around one day to perform 6 generations (240 solutions) using 20 workers. Therefore, in order to perform an optimization with 50 generations, we need around 8 days.
- A quarter model, which is obtained by reducing the length of the transmission lines to 10 μm (5 μm horizontal plus 5 μm vertical), is considered. Locations of the dipoles and the output planes with respect to the transmission lines are kept as in the full model. In this case, again using pools of 40 individuals and 20 workers in the MATLAB environment, we are able to complete 100 generations in 4 days. Once an optimal coupler is found, it is tested on the full geometry for the actual performance.

- For testing the sensitivity, a quarter model, where the sphere grid is shifted by one element towards the outer sides of the corner, is considered. In the following, three separate trials are shown for this scenario. Optimization histories (increase of the cost function) for these three optimizations can be seen in Fig. 4.

Figure 5 depicts the optimized coupler designs, in addition to the obtained electric field intensity. It can be observed that the couplers effectively improve the transmission along the nanowires, leading to better output values in comparison to the sharp case without any coupler (see Fig. 3). Better transmissions with the couplers are further verified in Fig. 6, where power density values at around the transmission lines as well as on the output planes are presented. We have the following conclusions.

- Using a quarter model for the optimizations instead of the full geometry provides quite successful results. In fact, the results for the full geometry in Figs. 5 and 6 are clearly worse than the corresponding results for the quarter geometry. This is due to the less number of generations (50 instead of 100) used for the full geometry, due to the slower optimization trials for this geometry. Although not shown, reducing the geometry further (smaller than the quarter) reduces the effectiveness of the optimizations, i.e., a designed coupler for the smaller geometry does not work sufficiently for the full case.

- Shifting the grid slightly changes the optimization results. This is partially due to the small rearrangements of the spherical particles when shifting is applied. Consequently, the optimizations seem to be stable, leading to reasonably good results that can be achieved.
- Three different optimizations for the same (shifted) grid and geometry provide similar results, again demonstrating the stability of the optimizations. Obviously, discrepancies also exist as the final geometries depicted in Fig. 5 are not exactly the same. If the results are investigated in detail, and as also depicted in Fig. 4, the second trial leads to a better performance among three trials with more than 1.8 kW/m^2 average power.
- Considering again the last three optimizations, the similarities between the coupler designs shown in Fig. 5 is remarkable. In general, we observe empty spaces on the right-top and left-bottom portions, while the particles mostly remain on the left-top and right-bottom sides. These designs may be used as seeds to reach more optimal couplers to be considered in a further work.

Finally, for more quantitative comparisons, Table 1 lists the average and maximum power density values at the outputs of the transmission lines considered in this paper. Although the maximum power is not directly

optimized, there is a high correlation between the maximum and average power values. In addition to the sharp (no-coupler) case, we consider the optimized (the second trial for the quarter model with shifted grid) case, as well as the curved designs with various ROC values. It can be observed that the optimized coupler improves the average power ten times than the no-coupler case. The improvement by the coupler is close to the curved sample with 2.5 μm ROC. Existence of any coupler design of the same size, which may provide transmissions as good as larger ROCs, is under investigation.
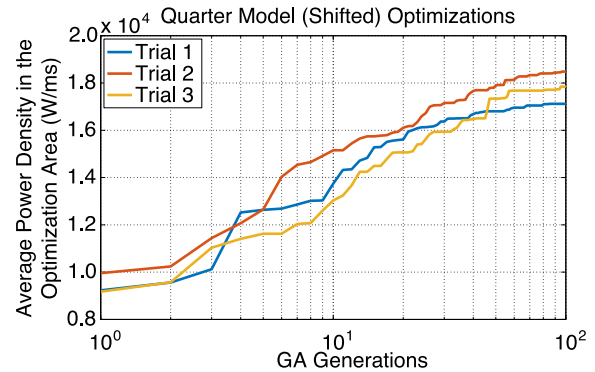
Fig. 4. Optimization histories for three trials on the shifted quarter model.
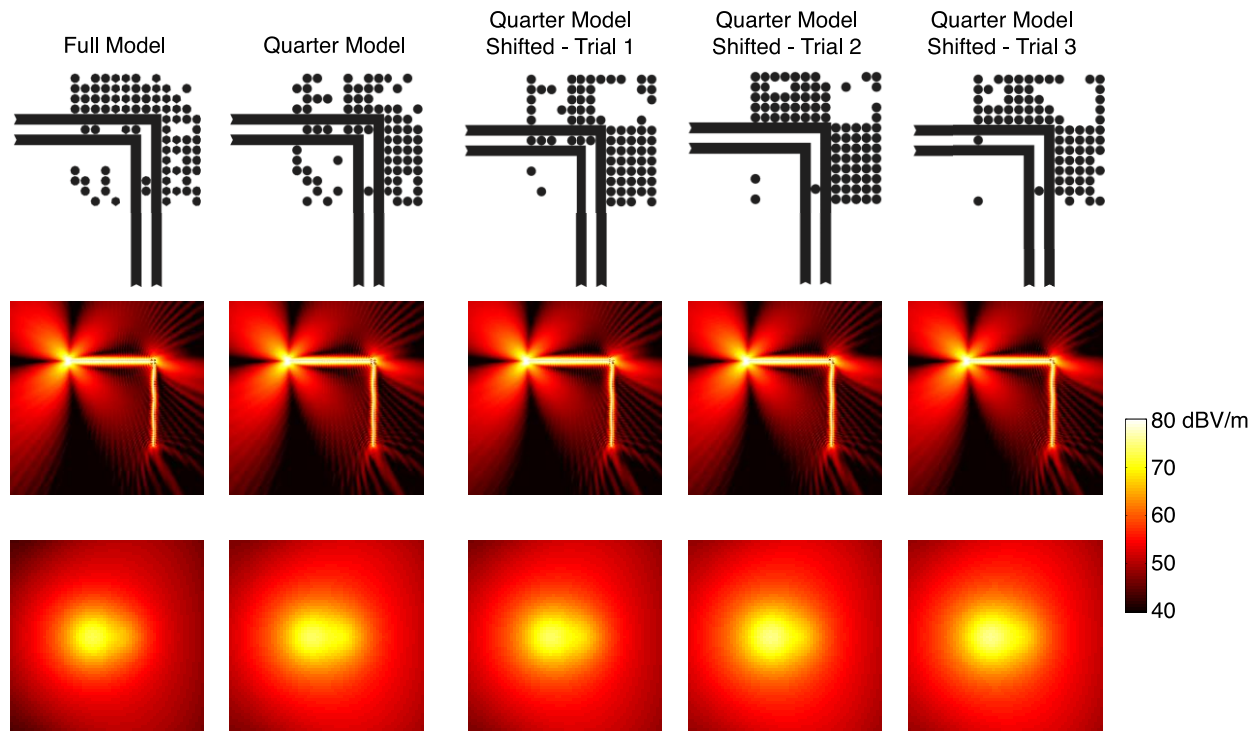
Fig. 5. Coupler designs (optimization results) to maximize the output of the 90° bended transmission line, and the corresponding electric field intensity at around the nanowires as well as on the output plane.
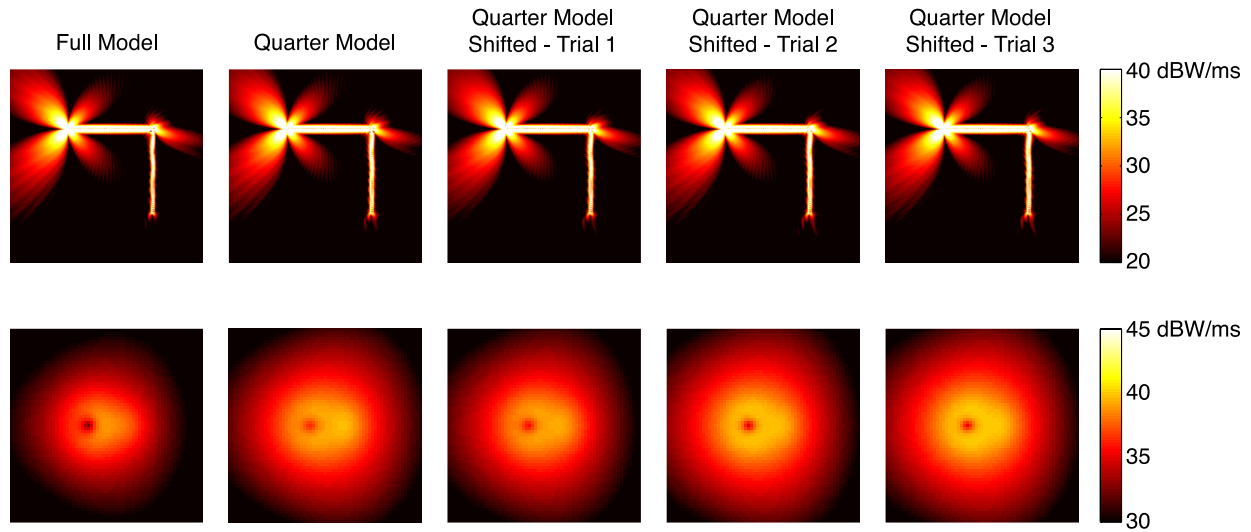
Fig. 6. The power density at around the nanowires when using the coupler designs at the corner of the 90° bended transmission line.

Table 1: Average and maximum power density values at the outputs of the transmission lines

	Curved Transmission Lines								
ROC	0.3μm	0.6 μm	0.9 μm	1.2 μm	2.5 μm	5.0 μm	10 μm	Sharp	Optimized
Average (kW/m^2)	0.924	1.04	1.18	1.38	3.26	6.85	10.4	0.307	3.22
Maximum (kW/m^2)	5.49	5.53	5.80	6.12	10.3	24.0	32.68	3.91	10.0

IV. CONCLUSION

We present simulation and optimization of optical couplers to improve the transmission ability of bended nanowire systems. By using an optimization mechanism involving efficient implementations of GAs and an MLFMA-based solver, we perform full-wave optimizations of couplers when they are located on the transmission lines (without resorting to isolation). We show that a well-designed coupler that involves only 100–200 spherical particles can improve the average power transmission through sharp corners by 10-folds without applying any curve at the bend locations.

ACKNOWLEDGMENT

REFERENCES

[1] X. Wang, C. J. Summers, and Z. L. Wang, "Large-scale hexagonal-patterned growth of aligned ZnO nanorods for nano-optoelectronics and nanosensor arrays," *Nano Lett.*, vol. 4, no. 3, pp. 423-426, Jan. 2004.

[2] H. Ditlbacher, A. Hohenau, D. Wagner, U. Kreibig, M. Rogers, F. Hofer, F. R. Aussenegg, and J. R. Krenn, "Silver nanowires as surface plasmon resonators," *Phys. Rev. Lett.*, vol. 95, no. 257403, Dec. 2005.

[3] A. W. Sanders, D. A. Routenberg, B. J. Wiley, Y. Xia, E. R. Dufresne, and M. A. Reed, "Observation of plasmon propagation, redirection, and fan-out in silver nanowires," *Nano Lett.*, vol. 6, no. 8, pp. 1822-1826, June 2006.

[4] A. V. Akimov, A. Mukherjee, C. L. Yu, D. E. Chang, A. S. Zibrov, P. R. Hemmer, H. Park, and M. D. Lukin, "Generation of single optical plasmons in metallic nanowires coupled to quantum dots," *Nature*, vol. 450, no. 7168, pp. 402-406, Nov. 2007.

[5] J. Yao, Z. Liu, Y. Liu, Y. Wang, C. Sun, G. Bartal, A. M. Stacy, and X. Zhang, "Optical negative refraction in bulk metamaterials of nanowires," *Science*, vol. 321, no. 5891, pp. 930, Aug. 2008.

[6] X. Guo, M. Qiu, J. Bao, B. J. Wiley, Q. Yang, X. Zhang, Y. Ma, H. Yu, and L. Tong, "Direct coupling of plasmonic and photonic nanowires for hybrid nanophotonic components and circuits," *Nano Lett.*, vol. 9, no. 12, pp. 4515-4519, 2009.

[7] B. D. F. Casse, W. T. Lu, Y. J. Huang, E. Gultepe, and L. Menon, "Super-resolution imaging using a three-dimensional metamaterials nanolens," *Appl. Phys. Lett.*, vol. 96, no. 023114, Jan. 2010.

[8] W. Wang, Q. Yang, F. Fan, H. Xu, and Z. L. Wang, "Light propagation in curved silver nanowire

plasmonic waveguides," *Nano Lett.*, vol. 11, no. 4, pp. 1603-1608, Mar. 2011.

[9] S. M. Bergin, Y. Chen, A. R. Rathmell, P. Charbonneau, Z. Y. Lib, and B. J. Wiley, "The effect of nanowire length and diameter on the properties of transparent, conducting nanowire films," *Nanoscale*, vol. 4, no. 6, pp. 1996-2004, Feb. 2012.

[10] M. Sun, Z. Zhang, P. Wang, Q. Li, F. Ma, and H. Xu, "Remotely excited Raman optical activity using chiral plasmon propagation in Ag nanowires," *Light: Science and Applications*, vol. 2, no. 112, Nov. 2013.

[11] Y. Huang, Y. Fang, Z. Zhang, L. Zhu, and M. Sun, "Nanowire-supported plasmonic waveguide for remote excitation of surface- enhanced Raman scattering," *Light: Science and Applications*, vol. 3, no. 199, Aug. 2014.

[12] J.P. Kottmann and O. J. F. Martin, "Plasmon resonances of silver nanowires with a non- regular cross section," *Phys. Rev. B*, vol. 64, no. 235402, Nov. 2001.

[13] A. Yılmaz, B. Karaosmanoğlu, and Ö. Ergül, "Computational electromagnetic analysis of defor-med nanowires using the multilevel fast multipole algorithm," *Sci. Rep.*, vol. 5, no. 8469, Feb. 2015.

[14] H. Aykut Şatana, B. Karaosmanoğlu, and Ö. Ergül, "A comparative study of nanowire arrays for maximum power transmission," in *Nanowires,* K. Maaz, Ed. InTech, 2017.

[15] J. Song, C.-C. Lu, and W. C. Chew, "Multilevel fast multipole algorithm for electromagnetic scattering by large complex objects," *IEEE Trans.*

[16] Ö. Ergül, "Solutions of large-scale electromagnetics problems involving dielectric objects with the parallel multilevel fast multipole algorithm," *J. Opt. Soc. Am. A.*, vol. 28, no. 11, pp. 2261-2268, Nov. 2011.

[17] B. Karaosmanoğlu, A. Yılmaz, and Ö. Ergül, "A comparative study of surface integral equations for accurate and efficient analysis of plasmonic structures," *in IEEE Transactions on Antennas and Propagation*, vol. 65, no. 6, pp. 3049e3057, June 2017.

[18] B. Karaosmanoğlu, A. Yılmaz, U. M. Gür, and Ö. Ergül, "Solutions of plasmonic structures using the multilevel fast multipole algorithm," *Special Issue on Challenges in RF and Microwave Defense Engineering, Int. J. RF Microwave Comput.-Aided. Eng.*, vol. 26, no. 4, pp. 335-341, May 2016.

[19] C. Önol, B. Karaosmanoğlu, and Ö. Ergül, "Efficient and accurate electromagnetic optimi-zations based on approximate forms of the multilevel fast multipole algorithm," *IEEE Antennas Wireless Propag. Lett.*, vol. 15, pp. 1113-1115, Apr. 2016.

[20] A. Çekinmez, B. Karaosmanoğlu, and Ö. Ergül, "Integral-equation formulations of plasmonic problems in the visible spectrum and beyond," in *Dynamical Systems - Analytical and Computational Techniques*, M. Reyhanoğlu, Ed. InTech, 2017.

[21] P. B. Johnson and R. W. Christy, "Optical constants of the noble metals," *Phys. Rev. B*, vol. 6, no. 12, pp. 4370-4379, Dec. 1972.

Antennas Propag., vol. 45, no. 10, pp. 1488-1493, Oct. 1997.

Baffle Diffraction in Interferometric Detectors of Gravitational Waves

Giuseppe Pelosi [1], Leonardo Possenti [1], Stefano Selleri [1], and Innocenzo M. Pinto [2]

[1] Department of Information Engineering
University of Florence, Florence, 50139, Italy
giuseppe.pelosi@unifi.it, leonardo.possenti@unifi.it, sefano.selleri@unifi.it

[2] Department of Engineering
University of Sannio, Benevento, 82100, Italy
pinto@sa.infn.it

Abstract ─ This paper presents an efficient high-frequency analysis framework for studying diffraction occurring at irises, or baffles, in the arms of a Fabry-Perot optical interferometer, relevant to the design and operation of interferometric detectors of gravitational waves like LIGO and Virgo.

Index Terms ─ Gaussian beams, gravitational wave detectors, uniform theory of diffraction.

I. INTRODUCTION

Recently interferometric detectors of gravitational waves like LIGO, Virgo and KAGRA provided the first direct observation of gravitational waves [1-2]. These instruments are very long baseline (~5km) Fabry-Perot optical interferometers, where the (quadrupole) spacetime ripples due to a gravitational wave are converted into an intensity modulation of the dark fringe [3-5].

The differential arm length perturbations to be measured are extremely small, of the order of 10^{-21}m, hence requiring extreme precision in the whole optical set-up, and extreme rejection of all possible noise sources. In particular, the (infrared, $\lambda = 1064$nm) laser beam travels the interferometer arms within pipes where high vacuum is created, to minimize light scattering from air molecules. Even if the beam is very narrow, the spot size on the terminal mirrors being a few cm wide, diffraction due to the finite size of the end-mirrors (and other optical components) [6] may cause a small amount of stray light to reach the vacuum pipe walls, that are coupled to environmental noise, creating multipath interference that may result into idiosyncratic noise features, that ultimately hinder the instrument's performance. Absorbing baffles or irises, are accordingly placed along the beam path, to intercept stray light that would eventually reach the pipe walls, and re-couple to the main FP cavity mode [7,8].

However, diffraction from the baffle edges can be itself a source of multipath interference; hence efficient modeling of baffle diffraction is necessary in order to optimize baffle design for present and next generation detectors.

In this paper we apply the uniform theory of diffraction (UTD) to a simple *canonical* baffle problem, using a realistic (Gaussian beam) model for the primary field in the arms, and a fully 3D baffle geometry. The proposed solution is analytic and physically readable, and the UTD-computed diffracted field is projected into the natural Gauss-Laguerre basis describing the light field the FP interferometer arms [4], to obtain an efficient (accurate, readable and easily computable) representation of the diffracted field.

The paper is organized as follows: the needed Gauss-Laguerre and UTD concepts are introduced in Section II and III, respectively. Section IV discusses the geometry of the baffle problem and the proposed UTD solution, with numerical results shown in Section V. Finally, Section VI draws some conclusions and hints for future work.

II. GAUSSIAN BEAMS

Laser beams are usually very narrow-band, and highly directive, so that the beam amplitude drops off rapidly as the angle between the beam axis and the direction of observation increases.

The (scalar) Gaussian beam solution of Helmholtz equation in the paraxial approximation, provides a very useful tool for the mathematical representation of fields which propagate unbounded but confined close to a specific direction, as laser beams [9].

Assuming axial symmetry, and propagation along the positive z direction, the fundamental (scalar) Gaussian beam field is:

$$u(\rho, z) = \frac{w_0}{w(z)} e^{-\frac{\rho^2}{[w(z)]^2}} e^{j\phi_G(z)} e^{-\frac{\pi\rho^2}{\lambda R(z)}} e^{-jkz}. \qquad (1)$$

The function $w(z)$ describes the beam width (distance between the points where the field's amplitude reduces by a factor e^{-1} from its maximum on-axis value); $w_0 = w(0)$ being denoted as the beam waist, as shown in Fig. 1. The larger w_0 the more collimated the beam. $R(z)$ is the wavefront radius of curvature. At the beam waist $z = 0$, $R(0)$ tends to infinity, as one would expect for a plane wave. Further away, $\lim_{z \to \infty} R(z) = z$, that is the radius of curvature of a spherical wavefront originating in $z = 0$. As the Gaussian beam propagates along the z-axis, its phase changes in a way which differs from that of a plane wave. The phase shift is represented by the Gouy phase $\phi_G(z)$ (see [9, 10] for details), resulting in a slightly increased distance between wavefronts.
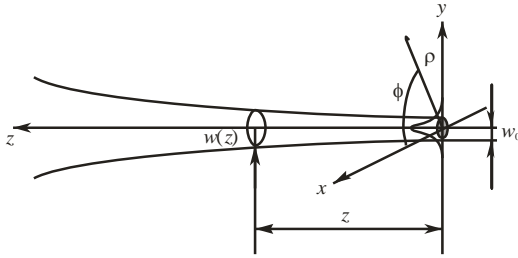
Fig. 1. Reference system and Gaussian beam, showing how the waist $w(z)$ changes along the beam propagation direction.

In real lasers or optical systems, axial symmetry cannot be guaranteed, and higher order modes can be excited. In cylindrical coordinates, these are the Gauss-Laguerre (GL) modes:

$$u(\rho, \phi, z) = \frac{w_0}{w(z)}\left(\frac{\sqrt{2}\rho}{w(z)}\right)^m L_p^m\left(\frac{2\rho^2}{[w(z)]^2}\right) \cdot$$
$$\cdot e^{-\frac{\rho^2}{[w(z)]^2}} e^{-j\frac{\pi\rho^2}{\lambda R(z)}} e^{-jkz} e^{jm\phi} e^{j\phi_G(z)}. \quad (2)$$

The Laguerre polynomials $L_p^m(x)$ are defined by two integer indices $p > 0$ and m and are of order $N = 2p + |m|$. The related Gouy phase shift $\phi_G(z)$ is larger than that of the fundamental Gaussian beam by a factor $N + 1$.

The two indices p and m describe, respectively, the radial and azimuthal dependence of the beam. In particular, the radial index p denotes the number of nodal rings on a plane perpendicular to the direction of propagation.

The superposition of the (p, m) and $(p,-m)$ GL modes yields the $TEM_{p,m}$ modes shown in Fig. 2.

In the case of interest here, the vector electromagnetic field is linearly polarized, and can be written as follows:

$$\mathbf{u}(\rho, \phi, z) = u(\rho, \phi, z)\hat{\mathbf{p}}, \quad (3)$$

where $\hat{\boldsymbol{p}}$ is a constant unit vector.
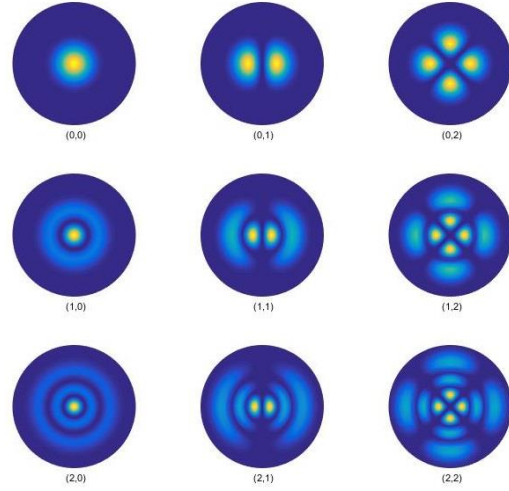
Fig. 2. Transverse intensity distribution of various $TEM_{p,m}$ (GL) beams.

III. UNIFORM THEORY OF DIFFRACTION

In the asymptotic high frequency limit, when the wavelength becomes negligible with respect to the size of the scattering objects, the light field can be computed by ray tracing (eikonal equation, Fermat principle) combined with field transport and energy conservation along the rays, yielding the geometrical optics (GO) solution [11].

The Fermat principle was generalized by Keller to include knife-edge and conical-tip diffracted rays, leading to an improved version of GO known as Geometrical Theory of Diffraction (GTD) [12].

The GTD field, however, may exhibit discontinuities (e.g., at shadow/reflection boundaries) and/or singularities (e.g. at caustics and foci).

The Uniform Geometrical Theory of Diffraction (UTD) was developed to overcome some of these limitations, namely the divergence at shadow boundaries, by the introduction of appropriate, physically motivated transition functions. UTD hence provides continuous field at shadow boundaries, even if it still fails at caustics [13].

In the asymptotic short wavelength limit, diffraction can be considered as a *local* phenomenon and the study of scattering is reduced to that of a few ideal "canonical" problems, the most relevant for our purposes being the "wedge problem" [14, 15].

The field scattered by a wedge is given by the superposition of GO and diffracted (UTD) field: the former takes into account incident and reflected fields in those regions where they exist; the latter guarantees continuity. The diffracted field may be accordingly written as $[\mathbf{E}^d] = [D][\mathbf{E}^i]A(\rho)e^{-jk\rho}$, where $[\mathbf{E}^d]$ and $[\mathbf{E}^i]$ are column matrices holding the components of

the diffracted and incident fields respectively, $[D]$ is a square matrix of diffraction coefficients, ρ is the distance from the wedge edge to the observation point and $A(\rho)$ is a spreading factor. Field components are conveniently given in a ray-fixed coordinate system (see [13-15] for details), hence incident and diffracted field are fully described by their parallel and perpendicular components with respect to the incidence and diffraction planes respectively, and $[D]$ is a 2-by-2 matrix. The diffraction matrix is available for perfectly conducting, perfectly absorbing and mixed (impedance) boundary condition wedges [13-15].

IV. FORMULATION

As a toy model for studying baffle diffraction in the beam pipes of a LIGO-like interferometric detector of gravitational waves, we consider the simple geometry depicted in Fig. 3: a planar metal screen placed at $z = z_b$, perpendicular to the pipe/beam axis z, with a centered circular aperture of radius a.

Fig. 3. Geometry for the baffle diffraction problem.

Even if the diffracting edge is a circular rim, its diameter is usually several thousands of wavelengths, so that the edge can be treated as locally straight, and UTD coefficients for the straight wedge can be used.

The baffle is illuminated by a 3D Gaussian beam (3) propagating along the z-axis, with the electric field linearly polarized along the y direction.

Different polarizations can, of course, be treated in a similar manner.

Table 1: Baffle aperture radius and observing plane used in our simulations

	$z_b = 5a$	$z_s = 2a + z_b$	$z_s = 5a + z_b$
$a = 0.05$ m	0.25 m	0.35 m	0.5 m
$a = 0.15$ m	0.75 m	1.05 m	1.5 m
$a = 0.5$ m	2.5 m	3.5 m	5 m

The diffracted field is evaluated on a plane at $z = z_s$ by resorting to the extended Fermat's principle to locate the diffraction point on the baffle rim for each diffracted ray path.

V. NUMERICAL RESULTS

For the present analysis, a wavelength $\lambda = 1\mu m$ has been considered, with a beam waist $w_0 = 10\lambda_0$, and unit amplitude on the beam axis.

Six different baffle geometries have been considered, whose relevant parameters are collected in Table 1.

The diffracted field has been computed using UTD and is depicted in Fig. 4, in normalized units for easier reading for various values of the baffle's aperture a and of the observation plane distance from the baffle's plane.

In all cases, an interference pattern appears. As the aperture becomes larger, the interference pattern tends to vanish.

As the distance between the planes at $z = z_b$ and $z = z_s$ increases, the intensity of the diffracted field also tends to vanish, and no interference pattern shows up.

One of the major numerical issues has been the very low incident field's values on the baffle's edge. Dealing with a wavelength and a beam waist in the order of 10^{-6}m and 10^{-4}m, the beam is extremely collimated and its intensity on the baffle's edge is of the order of 10^{-10}Vm^{-1}. Hence, the evaluation of the diffracted field is critical due to its very low intensity and to the finite machine's precision. Smaller values for the beam waist or an augmented intensity of the incident beam have been used in order to get larger values for the incident field on the baffle's edge, values which are then to be denormalized to attain final results.

Even if UTD overcomes the GTD issues at the shadow boundaries, thanks to the transition function, it is known that, as the distance from the edge increases, the UTD evaluation is more critical [13]. Special care was hence necessary in our case, where the field is computed thousands of wavelength away from the edge, to evaluate the transition function since, again, finite machine precision give rise to non-perfect singularity cancellation in diffraction coefficients very close to the shadow boundaries.

Table 2 shows CPU times. It can be noted how times are not the same, even if the number of points where the diffracted field is computed is the same, due to checks in the evaluation of the transition functions which are necessary as a increases and the baffle and the reference section gets farther apart.

Table 2: Times to compute the incident field on the edge, t_{inc}, and the diffracted field on the section, t_d, at two different distances from the baffle

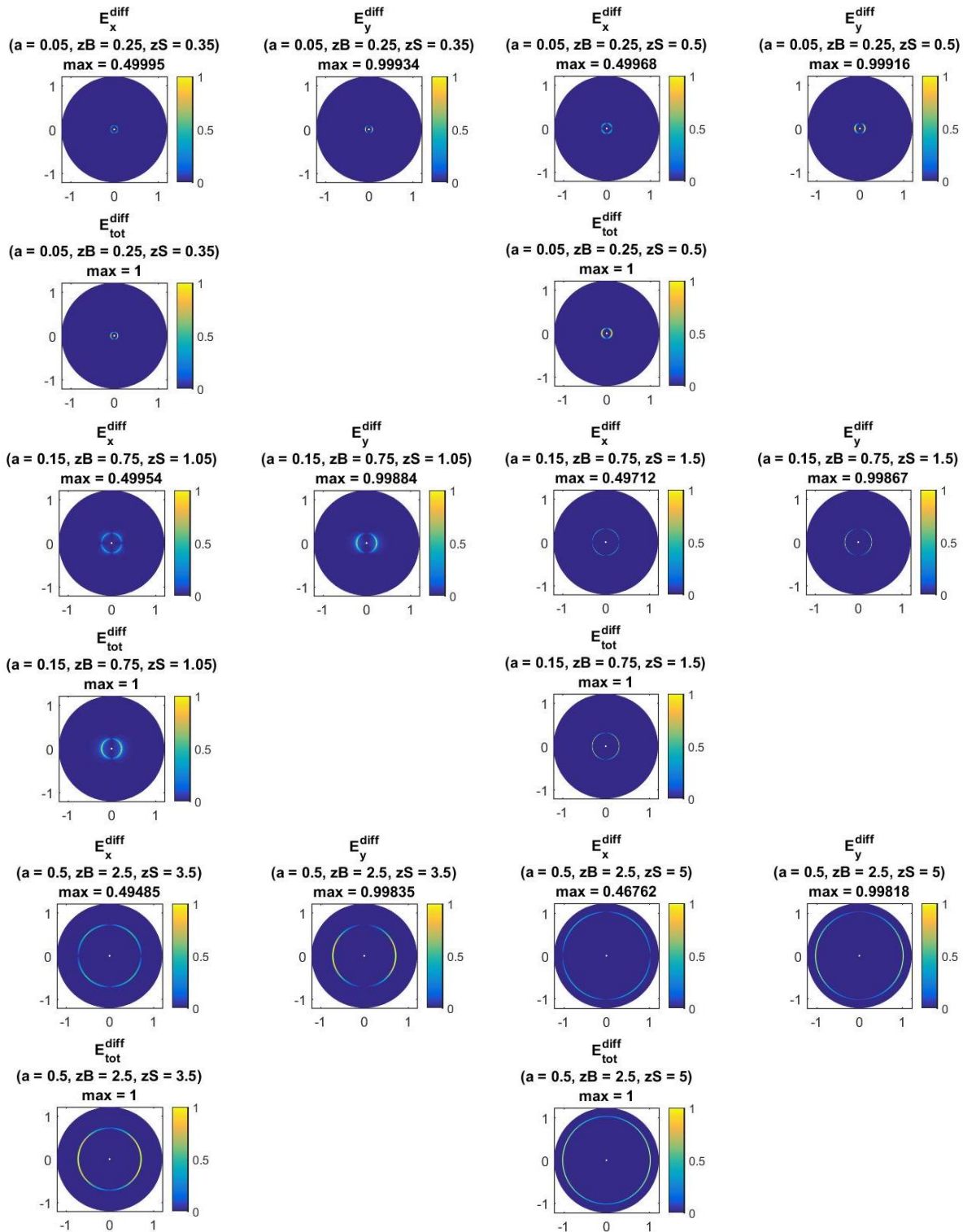|	$a = 0.05$ m	$a = 0.15$ m	$a = 0.5$ m
t_{inc}	0.017s	0.001s	0.001s
t_d @ $2a$	79,748s	79,865s	80,393s
t_d @ $5a$	79,826s	80,393s	81,005s

Fig. 4. Normalized transverse electric field components. Left column $z_s = 2a$; right column $z_s = 5a$.

VI. CONCLUSIONS

Light diffraction by a baffle with a circular aperture in a perfectly conducting screen illuminated by a Gaussian beam in a LIGO-like interferometric detector of gravitational waves has been discussed.

Gauss Laguerre modes have been used as a natural

representation tool for the fields in a FP cavity, and UTD has been used to compute the scattered fields. The predicted magnitude of the diffracted field is pretty low; yet the extreme sensitivity of gravitational wave detectors needs an accurate analysis of all possible noise sources, including stray light, as discussed here. Further developments will include more realistic geometric and material properties of the baffles, and a study of the impact of baffle-diffracted light on the noise floor of the instrument.

ACKNOWLEDGMENTS

REFERENCES

[1]   B. P. Abbott. et al., "LIGO: The laser interferometer gravitational wave observatory," *Rep. Prog. Phys.*, vol. 72, no. 6, pp. 07690-07740, 2009.

[2]   T. Accadia, et al., "Virgo: A laser interferometer to detect gravitational waves," *J. Instrum.*, vol. 7, no. 3, pp. 3012-3018, 2012.

[3]   Y. Aso, et al., "Interferometer design of the KAGRA gravitational wave detector," *Phys. Rev. D*, vol. 88, no. 8, pp. 043007-043023, 2013.

[4]   B. P. Abbott, "Observation of gravitational waves from a binary black hole merger," *Phys. Rev. Letters*, vol. 116, no. 2, pp. 061102-061118, 2016.

[5]   B. P. Abbott, "GW151226: Observation of gravitational waves from a 22-solar-mass binary black hole merger," *Phys. Rev. Letters*, vol. 116, no. 6, pp. 241103-241117, 2016.

[6]   B. Bhawal, "Diffraction losses of various modes in advanced LIGO arm cavity," *LIGO Document* T050234, 2005.

[7]   M. R. Smith, "Stray light control for advanced LIGO," *LIGO Document* G1100232, 2011.

[8]   A. Chiummo, "Advanced Virgo stray light control status," *LIGO Document* G1301021, 2013.

[9]   A. E. Siegman, *Lasers*. Univ. Science Books, Sausalito (CA), 1986.

[10]   A. Javier, "Laser and Gaussian beam propagation and transformation," in *Encyclopedia of Optical Engineering*, Marcel Dekker Inc., New York, 2003.

[11]   M. Born and E. Wolf, *Principles of Optics*. Cambridge Univ. Press, Cambridge (UK), 2002.

[12]   J. B. Keller, "Geometrical theory of diffraction," *J. Opt. Soc. Amer.*, vol. 52, no. 2, pp. 116-130, 1962.

[13]   R. G. Kouyoumjian and P. H. Pathak, "A uniform geometrical theory of diffraction for an edge in a perfectly conducting surface," *Proc. of the IEEE*, vol. 62, no. 11, pp. 1448-1461, 1974.

[14]   G. Pelosi, Y. Rahmat-Samii, and J. Volakis, Eds., "High-frequency techniques in diffraction theory: 50 years of achievements in GTD, PTD, and related approaches," [Part I] *IEEE Antennas Propag. Mag.*, APM-55 (3), pp. 16-58, June 2013; [Part II] *IEEE Antennas Propag. Mag.*, APM-55 (4), pp. 17-79, Aug. 2013.

[15]   G. Pelosi and S. Selleri, "The wedge-type problem: The building brick in high-frequency scattering from complex objects," *IEEE Antennas and Propag. Mag.*, vol. APM-55 (3), pp. 41-58, 2013.

Giuseppe Pelosi was born in Pisa, Italy, in 1952. He received the Laurea (Doctor) degree in Physics (summa cum laude) from the University of Florence in 1976. He is currently with the Department of Information Engineering of the same university, where he is currently Full Professor of Electromagnetic Fields. His research activity is mainly focused on numerical techniques for applied electromagnetics (antennas, circuits, microwave and millimeter-wave devices, scattering problems). He was coauthor of several scientific publications on the aforementioned topics, appeared in international refereed journals. He is also coauthor of three books and several book chapters.

Pelosi was elected a Fellow of the IEEE for contributions to computational electromagnetics.

Leonardo Possenti was born in Florence (Italy) in 1991. He received the Laurea degree (cum laude) in Telecommunication Engineering from the University of Florence (Italy). In 2016 he attended a semester at the Tampere University of Technology, in Tampere (Finland). Since November 2016 he has been pursuing his Ph.D. at the University of Florence (Italy). His recent interests are mainly in high-frequency electromagnetic scattering in particular from impedance structures via GTD and UTD solutions and some of their applications in physics and space engineering.

Stefano Selleri was born in Viareggio, Italy, on December 9th, 1968. He obtained his degree (Laurea), cum laude, in Electronic Engineering and the Ph.D. in Computer Science and Telecommunications from the University of Florence in 1992 and 1997, respectively. He is author of over 90 papers on international referred journals and

eight books or books chapters. He is currently an Assistant Professor at the University of Florence, where he conducts research on numerical modeling of microwave, devices and circuits with particular attention to numerical optimization.

Innocenzo M. Pinto received the Laurea degree in Electrical Engineering (cum laude) from the University of Naples, Napoli, Italy, in 1976. He became an Assistant Professor of Electromagnetics in 1983, an Associate Professor in 1987, and a full Professor in 1990.

In 1998, he joined the University of Sannio, Benevento, Italy, where he has been the University President's Delegate for International Liaisons and Scientific Research, a Member of the Evaluation Board, and the Dean of the Faculty of Engineering. His research interests include Electromagnetics, Gravitational Wave Theory and Experiments, and Applied Mathematics. He has published more than 150 peer-reviewed journal papers and book chapters. Pinto is a Senior Member of the IEEE, a Member of the American Physical Society, and a PI for the LIGO-Virgo Scientific Collaboration and the LCGT-KAGRA Collaboration.

Finite Difference Time Domain Modeling of Fringe Waves

Mehmet Alper Uslu [1], Gokhan Apaydin [2], and Levent Sevgi [3]

[1] Department of TGE, NETAS, Istanbul, Turkey
auslu@netas.com.tr

[2] Electromagnetic Consulting, Istanbul, Turkey
g.apaydin@gmail.com

[3] Department of Electrical-Electronics Engineering
Okan University, Tuzla, Istanbul, 34759, Turkey
levent.sevgi@okan.edu.tr

Abstract ─ A novel method is introduced for calculating fringe currents and fringe waves around the tip of a perfectly reflecting wedge under line source illumination. The time-domain fringe (non-uniform) currents are extracted with the finite-difference time-domain (FDTD) method. These currents are then fed into a free-space FDTD and fringe waves are excited. Alternatively, fringe waves are also obtained using the Green's function approach. The validation of the proposed method and the verification of the results are done against the physical theory of diffraction (PTD) as well as the method of moments (MoM). The factors affecting the accuracy are also discussed.

Index Terms ─ Finite difference time domain (FDTD), fringe waves, method of moments (MoM), nonuniform currents, physical theory of diffraction, PTD, uniform currents, wedge.

I. INTRODUCTION

Physical optics (PO), introduced by Macdonald in 1912, is a high frequency asymptotic (HFA) technique used for the calculations of scattered fields from perfectly electrical conducting (PEC) objects [1]. PO is a source-based technique where currents are assumed to be induced on an infinite PEC plane tangent to the object. PO source induced currents, which are nonzero only on the illuminated side of object's surface (away from any discontinuity), are named as uniform currents. PO-based scattered fields, which consist of reflected and diffracted fields, yield inaccurate results for the objects having discontinuities such as sharp edges and/or tips. This is because the magnitude of the induced currents near a discontinuity is not uniformly distributed. In other words, diffraction is not modeled properly with PO's uniform current approximation. Physical theory of diffraction (PTD) extends PO by introducing fringe (non-uniform) currents. The PTD scattered fields contain contributions of both uniform (PO) currents and non-uniform (fringe) currents [2]. The fields radiated from fringe currents are called fringe waves.

The understanding and investigation of fringe waves are critical in broad range of electromagnetic (EM) problems, such as radar cross-section, propagation, electromagnetic compatibility modeling and simulation. The canonical wedge structure has long been used for this purpose. For example, exact and asymptotic formulations of fringe currents are given for a PEC wedge illuminated by a plane wave in [3] and for the line source illumination in [4]. A novel method of moments (MoM)-based approach is also introduced recently [5]. Finite difference time domain (FDTD) is a numerical method used in solving Maxwell's equations in time domain. It has been widely used in variety of EM problems including radiation, propagation, and scattering. The FDTD method has also been used in the calculation of diffraction coefficients and there are many studies in modeling diffraction from various wedges [6]–[9]. Recently, double tip diffraction has also been modeled with FDTD [10]. Here, we propose a novel FDTD method for the extraction of fringe currents and fringe waves on the canonical PEC wedge structure. The fringe fields are also computed via Green's function based on FDTD-extracted fringe currents.

The paper is organized as follows. In Section 2, we describe the problem and summarize PTD fringe wave expressions. Then, the FDTD-based fringe currents extraction procedure is outlined in Section 3. Section 4 presents examples and numerical comparisons against the PTD and MoM data. Conclusions are given in Section 5.

II. GEOMETRY OF THE PROBLEM

The geometry of the problem is shown in Fig. 1.

Here, a PEC wedge with apex angle $2\pi - \alpha$ is illuminated by a line source located at (ρ_0, φ_0). The tip of the wedge is at the origin. The receiver is at (ρ, φ). The incident EM wave hits the wedge and induces surface currents. This induced current consists of uniform (PO) and non-uniform (fringe) parts [2]. Non-uniform currents cause fringe waves.
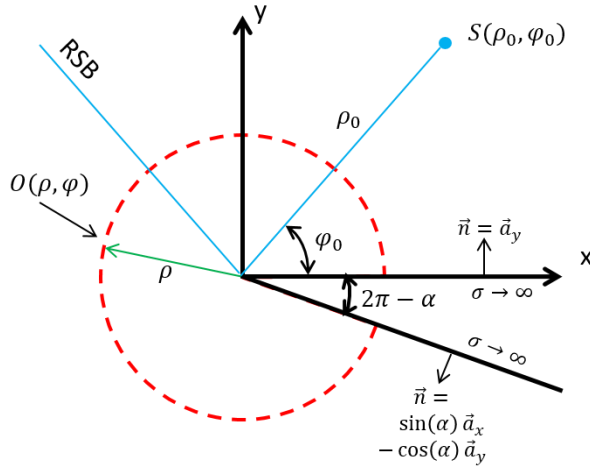

Fig. 1. Geometry of the problem under SSI illumination.

PTD fringe fields are obtained by subtracting PO diffracted fields from total/exact diffracted fields:

$$u^{fringe} = u^{d,Exact} - u^{d,PO}. \tag{1}$$

Exact diffracted fields can be obtained from both integral and series summation representations [2, 3, 11]. Below, the integral solution is given for the sake of completeness for both soft (TM) and hard (TE) boundary condition (BC), respectively:

$$u_s^d = \{V_d(-\pi - \varphi + \varphi_0) - V_d(\pi - \varphi + \varphi_0)\} - \{V_d(-\pi - \varphi - \varphi_0) - V_d(\pi - \varphi - \varphi_0)\}, \tag{2}$$

$$u_h^d = \{V_d(-\pi - \varphi + \varphi_0) - V_d(\pi - \varphi + \varphi_0)\} + \{V_d(-\pi - \varphi - \varphi_0) - V_d(\pi - \varphi - \varphi_0)\}, \tag{3}$$

where

$$V_d(\beta) = \frac{1}{2\pi n} \int_0^\infty H_0^{(1)}[kR(it)] \frac{\sin(\beta/n)}{\cosh(t/n) - \cos(\beta/n)} dt, \tag{4}$$

with $n = \alpha/\pi$ and $R(\eta) = \sqrt{r^2 + r_0^2 + 2rr_0\cos(\eta)}$. PO diffracted fields are given as [4]:

$$u_{s,h}^{d,PO}(r,\varphi) = u^{d,inc} + u_{s,h}^{d,refl}, \tag{5}$$

where

$$u^{d,inc}(r,\varphi) = \frac{kr\sin(\varphi - \varphi_0)}{4i} \int_0^\infty H_0^{(1)}[k(r_0 + r')]H_1^{(1)}(k\rho^-)\frac{dr'}{\rho^-}, \tag{6}$$

with $\rho^- = \sqrt{r^2 + r'^2 + 2rr'\cos(\varphi - \varphi_0)}$ and,

$$u_s^{d,refl}(r,\varphi) = -\frac{kr\sin(\varphi + \varphi_0)}{4i} \int_0^\infty H_0^{(1)}[k(r_0 + r')]H_1^{(1)}(k\rho^+)\frac{dr'}{\rho^+}, \tag{7}$$

with $\rho^+ = \sqrt{r^2 + r'^2 + 2rr'\cos(\varphi + \varphi_0)}$. The term $u_h^{d,refl}$ is used for hard BC and expressed by the opposite of (7). Numerical computation of this integral representation is discussed in [12].

III. FDTD MODELING OF FRINGE WAVES

FDTD is a numerical method which is based on discretization of Maxwell's equations in both space and time. The first and most popular (staircase) discretization scheme was proposed by Yee in 1966 [13]. In this scheme, field components are assumed to be located in space as shown in Figs. 2 and 3. Besides the spatial difference, electric and magnetic fields are also assumed to be separated in the time domain by a half-time step. The 2D FDTD equations, for the scenario in Fig. 1, corresponding to soft (TM$_z$) and hard (TE$_z$) BC problems contain (H$_x$, H$_y$, E$_z$) and (E$_x$, E$_y$, H$_z$) components, respectively.
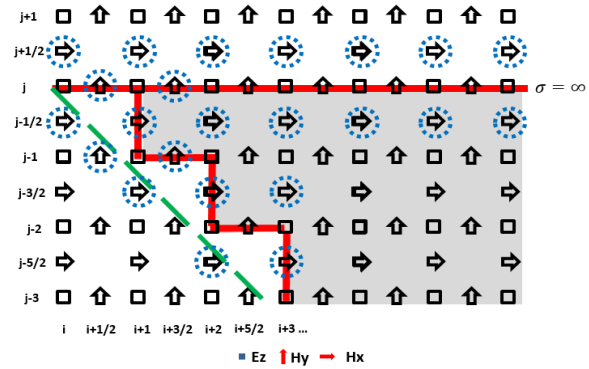

Fig. 2. A FDTD model of the problem in the TMz configuration. The magnetic field components used for calculation of surface currents are circled.
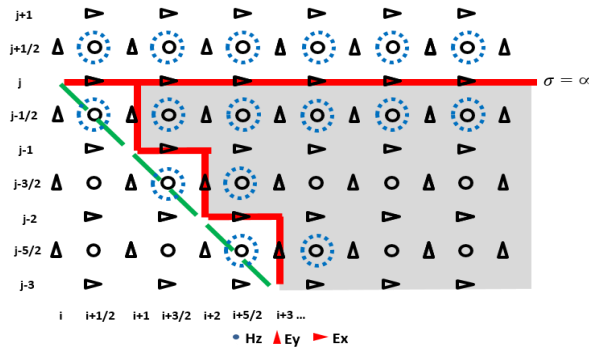

Fig. 3. A FDTD model of the problem in the TEz configuration. The magnetic field components used for calculation of surface currents are circled.

The PEC wedge in TM_z configuration is modeled by setting all electric field components to zero for the cells lying inside. For TE_z configuration, the electric field components lying inside are set to zero and the magnetic fields are updated in the usual way.

The source-induced surface currents are modeled using the tangential magnetic fields. On the top surface and for the TMz mode, this is expressed by:

$$\vec{J}_s^{top} = \hat{a}_y \times \vec{H} = -\hat{a}_z H_x. \tag{8}$$

The field components are not collocated because of the staggered nature of FDTD grid. Hence, spatial averaging can be applied to magnetic fields for approximating their values on the boundaries. As shown in Fig. 2, H_x components are positioned a half-cell ($\Delta y / 2$) above and below of top surface; these are used in averaging source-induced surface currents. The bottom surface is not that simple because the normal direction changes according to the position of the E-field. For example, the surface normal is directed along $-\hat{a}_x$ for the boundary between nodes $(i+1, j)$ and $(i+1, j-1)$. Hence, source-induced surface current is obtained by averaging four H_y located around the boundary, i.e.:

$$\vec{J}_s^{bot,TM_z}(n,1) = 0.25 \begin{bmatrix} H_y(i+1/2, j-1) + H_y(i+1/2, j) \\ + H_y(i+3/2, j-1) + H_y(i+3/2, j) \end{bmatrix}, \tag{9}$$

where n is time index. For TE_z mode, H_z is used in obtaining source-induced surface currents on both top and bottom surfaces. As seen in Fig. 3, spatial averaging is also required for this mode.

The novel multi-step FDTD approach used for the calculation of fringe currents and fringe waves in the time domain is as follows:

- Run the FDTD simulation for the PEC wedge structure and record surface currents in the time domain. On the top surface, recorded currents contain both uniform and non-uniform parts; on the bottom surface it contains only non-uniform currents.
- Make the wedge angle 180° (i.e., replace wedge with the half-plane), run the FDTD simulation again, and record surface currents only on the top surface of the wedge. Recorded data contains only uniform (PO) currents.
- Subtract data recorded in Step 2 from Step 1 and obtain only non-uniform currents on the top surface.
- Remove the wedge from the FDTD space, use discrete form of $\nabla \times \vec{H} = \varepsilon_0 \partial \vec{E} / \partial t + \vec{J}$ equation and feed the time-domain fringe current using $\vec{J}$ to the related E-field component(s) and run the FDTD program. The FDTD simulation directly yields the fringe waves.

Note that, this procedure is for single side illumination (SSI) as shown in Fig. 1. For the double-side illumination (DSI), where both faces of wedge are illuminated by the incident field, uniform currents are also induced on the bottom surface; hence one additional step, which is similar to Step 2, needs to be performed. In this step, the bottom surface of the wedge is extended to infinity and the time domain currents are recorded. The recorded currents are formed by only uniform currents and they need to be subtracted from the total currents obtained in step 1 on bottom surface.

Note also that, frequency domain fringe currents (at a specified frequency) may also be obtained using FFT. Fringe waves may then be calculated analytically using the Green's function representations, for example, as in (6a) and (6b) in [10] for the TE and TM modes, respectively.

IV. EXAMPLES AND COMPARISONS

The proposed approach is validated and verified against PTD and MoM through the examples presented in Figs. 4-11. Here, different wedge angles (0°, 45°, and 90°) and different angle of illuminations are used. The frequency is 30 MHz.

In Fig. 4, TM_z fringe fields around a 90° PEC wedge, illuminated by a line source at $\rho_0=60$ m, $\varphi_0=70°$ recorded on a circle with a radius 20 m (2λ) from the tip are shown. Note that, Fig. 4 (a) shows angular variation of the fringe fields in the frequency domain, while Fig. 4 (b) shows a snapshot during the FDTD simulations (i.e., time-domain pulsed fringe fields).

Time domain characteristics of PO and fringe currents, recorded on the top surface of this wedge at a point 1.5 m away from the tip, are shown in Fig. 5. Normalized frequency domain variations of the same point are also shown in Fig. 6 with source's FFT.

The total (uniform + non-uniform) and non-uniform currents induced on this PEC wedge are shown in Fig. 7. As observed, non-uniform currents concentrate in the vicinity of edge. Figures 8 and 9 belong to the same scenario but for the TE_z polarization.

The simulations are repeated for 0° and 45° PEC wedges and results are presented in Figs. 10 and 11. As observed, very good agreement among analytical and numerical methods are achieved.

Note that, FDTD simulations are performed on a 400×400 cell area. The spatial resolution is $\Delta x = \Delta y = \lambda / 20$ corresponds to 0.5 m cell size at 30 MHz. Temporal resolution is $\Delta t = 1.18$ ns. Once-differentiated Gaussian pulse is used as the excitation $\sqrt{2e}(n\Delta t - t_0)/\tau\, e^{-(n\Delta t - t_0)^2/\tau^2}$. Here, n is time-step, $\tau = \sqrt{2.3}/\pi f_0 \approx 0.16$ ns is the characteristics-half width and $t_0 = 4.5\tau$ is temporal delay. The discretization of the PTD and MoM are as in [4] and [5], respectively.
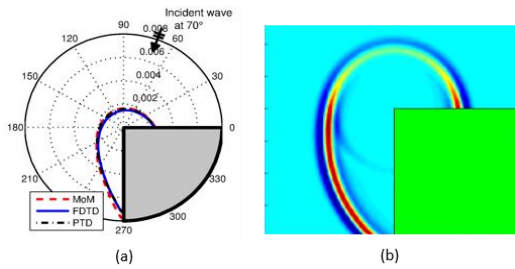
Fig. 4. (a) Fringe fields around the tip of the wedge for TM_z polarization (SSI), Dashed: MoM, Solid: FDTD, Dashed-dotted: PTD, $\alpha=270°$, $\rho_0=60$ m, $\varphi_0=70°$, $\rho=20$ m, $f=30$ MHz; (b) a time-domain snapshot showing broadband fringe fields.
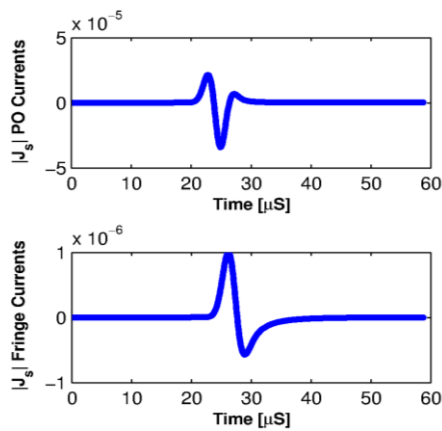

Fig. 5. Time domain surface currents for TM_z polarization of above scenario recorded on top surface at 1.5 m distance from the tip, (Top) PO currents, (Bottom) fringe (non-uniform) currents, $\alpha=270°$, $\rho_0=60$ m, $\varphi_0=70°$, $\rho=20$ m, $f=30$ MHz.
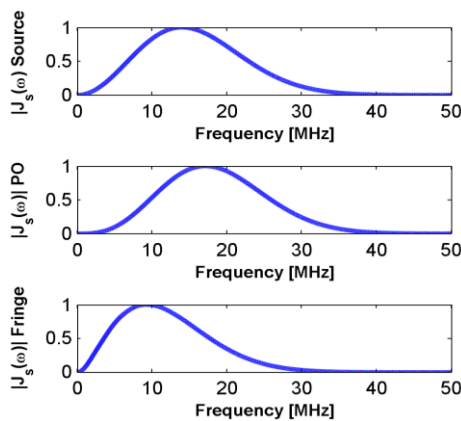

Fig. 6. Normalized frequency domain surface currents for TM_z polarization of above scenario recorded on top surface at 1.5 m distance from the tip, (Top) Source's FFT, (Middle) FFT of PO currents, (Bottom) FFT of fringe (non-uniform) currents, $\alpha=270°$, $\rho_0=60$ m, $\varphi_0=70°$, $\rho=20$ m, $f=30$ MHz.

Fig. 7. Wedge surface currents for TM_z polarization of above scenario, (Top) total currents, (Bottom) fringe (non-uniform) currents, $\alpha=270°$, $\rho_0=60$ m, $\varphi_0=70°$, $\rho=20$ m, $f=30$ MHz Solid: MoM, Dashed: FDTD (left and right portions belong to the bottom and top surfaces, respectively).

Fig. 8. (a) Fringe fields around the tip of the wedge; Dashed: MoM, Solid: FDTD, Dashed-dotted: PTD (TE_z pol, SSI, $\alpha=270°$, $\rho_0=60$ m, $\varphi_0=70°$, $\rho=20$ m, $f=30$ MHz); (b) a time-domain FDTD snapshot showing broad-band fringe fields.
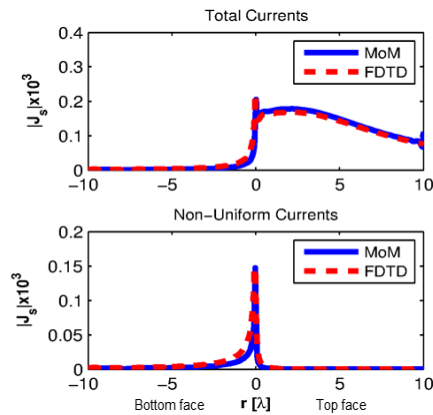

Fig. 9. Wedge surface currents for TE_z polarization of above scenario, (Top) total currents, (Bottom) fringe (non-uniform) currents, $\alpha=270°$, $\rho_0=60$ m, $\varphi_0=70°$, $\rho=20$ m, $f=30$ MHz Solid: MoM, Dashed: FDTD (left and right portions belong to the bottom and top surfaces, respectively).
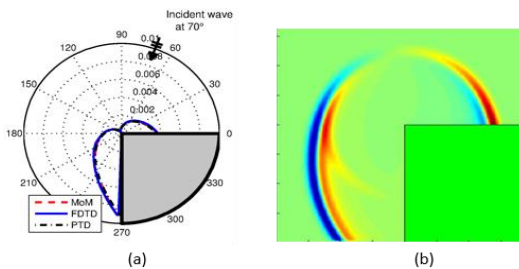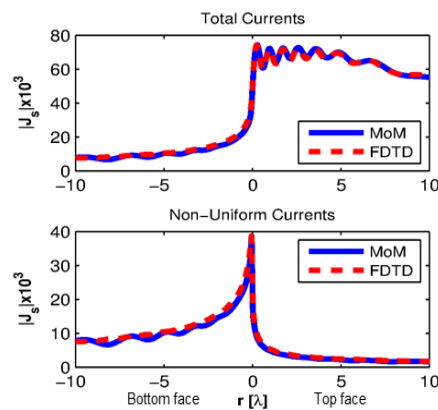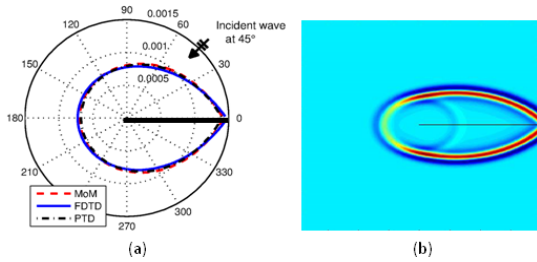
Fig. 10. (a) Fringe fields around the tip of the wedge; Dashed: MoM, Solid: FDTD, Dashed-dotted: PTD (TM$_z$ pol, SSI, α=360°, ρ$_0$=70 m, φ$_0$=45°, ρ=20 m, f=30 MHz); (b) a time-domain FDTD snapshot.
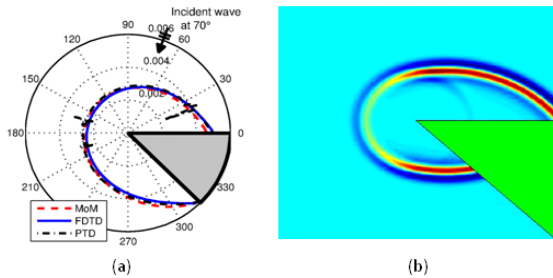

Fig. 11. (a) Fringe fields around the tip of the wedge; Dashed: MoM, Solid: FDTD, Dash-dot: PTD (SSI, TM$_z$ pol, α=315°, ρ$_0$=60 m, φ$_0$=70°, ρ=5 m, f=30 MHz); (b) a time-domain FDTD snapshot.

V. CONCLUSIONS

For the first time in the literature, a novel, FDTD diffraction method is introduced for the simulation of fringe currents and fringe waves around a PEC wedge. Fringe currents and fringe waves are presented both in the frequency and time domains. The validity of the proposed method and the verification of the accuracy of the results are done using PTD and MoM generated fringe currents and fields.

Note that, using geometric averaging yields better performance for collocating electric and magnetic fields [14] and the accuracy may be increased. Also, the rectangular grid used in the standard FDTD algorithm limits the accuracy, especially for the TE polarization [15]. This limitation can be removed by using FDTD algorithms based on conformal cells [16]. Note also that, the FDTD-extracted fringe currents and fringe waves further demonstrate the argument on the modified theory of physical optics (MTPO) in [17].

REFERENCES

[1] H. Macdonald, "The effect produced by an obstacle on a train of electric waves," *Philosophical Transactions of the Royal Society A: Mathematical, Physical and Engineering Sciences*, vol. 212, no. 484-496, pp. 299-337, 1913.

[2] P. Ufimtsev, *Fundamentals of the Physical Theory of Diffraction*. Hoboken, N.J.: Wiley-Interscience, 2007.

[3] P. Ufimtsev, A. Terzuoli, and R. Moore, *Theory of Edge Diffraction in Electromagnetics*. Raleigh, NC: SciTech, 2009.

[4] F. Hacivelioglu, L. Sevgi, and P. Ufimtsev, "Wedge diffracted waves excited by a line source: Exact and asymptotic forms of fringe waves," *IEEE Trans. Antennas Propag.*, vol. 61, no. 9, pp. 4705-4712, Sept. 2013.

[5] G. Apaydin, F. Hacivelioglu, L. Sevgi, and P. Ufimtsev, "Wedge diffracted waves excited by a line source: Method of moments (mom) modeling of fringe waves," *IEEE Trans. Antennas Propag.*, vol. 62, no. 8, pp. 4368-4371, Aug. 2014.

[6] G. Cakir, L. Sevgi, and P. Ufimtsev, "FDTD modeling of electromagnetic wave scattering from a wedge with perfectly reflecting boundaries: Comparisons against analytical models and calibration," *IEEE Trans. Antennas Propag.*, vol. 60, no. 7, pp. 3336-3342, July 2012.

[7] G. Stratis, V. Anantha, and A. Taflove, "Numerical calculation of diffraction coefficients of generic conducting and dielectric wedges using FDTD," *IEEE Trans. Antennas Propag.*, vol. 45, no. 10, pp. 1525-1529, Oct. 1997.

[8] V. Anantha and A. Taflove, "Calculation of diffraction coefficients of three-dimensional infinite conducting wedges using FDTD," *IEEE Trans. Antennas Propag.*, vol. 46, no. 11, pp. 1755-1756, Nov. 1998.

[9] M. A. Uslu and L. Sevgi, "Matlab-based virtual wedge scattering tool for the comparison of high frequency asymptotics and fdtd method," *The Applied Computational Electromagnetics Society*, vol. 27, no. 9, 2012.

[10] M. A. Uslu, G. Apaydin, and L. Sevgi, "Double tip diffraction modeling: Finite difference time domain vs. method of moments," *IEEE Trans. Antennas Propag.*, vol. 62, no. 12, pp. 6337-6343, Dec. 2014.

[11] J. Bowman, T. Senior, and P. Uslenghi, *Electromagnetic and Acoustic Scattering by Simple Shapes*. New York: Hemisphere, 1987.

[12] F. Hacivelioglu, L. Sevgi, and P. Y. Ufimtsev, "On the numerical evaluation of diffraction formulas for the canonical wedge scattering problem," *IEEE Antennas Propag. Mag.*, vol. 55, no. 5, pp. 257-272, Oct. 2013.

[13] K. Yee, "Numerical solution of initial boundary value problems involving Maxwell;s equations in isotropic media," *IEEE Trans. Antennas Propag.*, vol. 14, no. 3, pp. 302-307, May 1966.

580   ACES JOURNAL, Vol. 32, No. 7, July 2017

Mehmet Alper USLU received the B.S., M.S., and Ph.D. degrees in Electronics and Communications engineering from Dogus University, Istanbul, Turkey, in 2010, 2011, and 2015, respectively. His research interests are diffraction theory, radar system design, computational electromagnetics, RF Microwave circuits and systems, EMC, Digital Signal Processing Algorithms, Realtime/ Embedded Software Development, Radar Cross Section modeling. He has been with NETAS since 2012.

Gökhan Apaydin received the B.S., M.S., and Ph.D. degrees in Electrical and Electronics Engineering from Bogazici University, Istanbul, Turkey, in 2001, 2003, and 2007, respectively. He was a Teaching and Research Assistant with Bogazici University from 2001 to 2005; he was a Project Engineer with the University of Technology Zurich, Zurich, Switzerland, from 2005 to 2010; he was with Zirve University, Gaziantep, Turkey from 2010 to 2016; and he was a Visiting Associate Professor at the Department of ECE, University of Illinois at Urbana–Champaign, Champaign, IL, USA, in 2015. He has been involved with complex electromagnetic problems and systems. His research interests include analytical and numerical methods (FEM, MoM, FDTD, and SSPE) in electromagnetics (especially on electromagnetic computation of wave propagation, diffraction modeling, and related areas).

Levent Sevgi received the Ph.D. degree from Istanbul Technical University (ITU), Turkey, and Polytechnic Institute of New York University, Brooklyn, in 1990. Prof. Leo Felsen was his Advisor. He was with ITU (1991-1998); the Scientific and Technological Council of Turkey–Marmara Research Institute, Gebze/Kocaeli (1999-2000); Weber Research Institute/Polytechnic University in New York (1988-1990); the Scientific Research Group of Raytheon Systems, Canada (1998-1999); the Center for Defense Studies, ITUVSAM (1993-1998) and (2000-2002); the Department of ECE, UMASS Lowell, MA, USA (2012-2013) for his sabbatical term; and Dogus University (2001-2014). Since 2014, he has been with Okan University, Istanbul. He has been involved with complex electromagnetic problems and systems for nearly 30 years.

An Improved Shooting and Bouncing Ray Method for Outdoor Wave Propagation Prediction

Dan Shi, Na Lv, Nan Wang, and Yougang Gao

Department of Electronic Engineering
Beijing University of Posts and Telecommunications, Beijing, 100000, China
shidan@buptemc.com

Abstract ─ An improved algorithm for shooting and bouncing ray tracing (SBR) is proposed in this paper. The conventional SBR method has to launch a large number of rays or ray tubes to guarantee the accuracy, which increases the calculation time significantly. This paper presents a novel adaptive ray launching (ARL) method based on the pattern of transmitting antenna, which reduces the launched rays greatly while maintaining the computation accuracy. Some examples of applying the proposed method to calculate the outdoor radio wave propagation are presented, and the results are compared with the measurements and simulations. The good agreements between them validate the proposed approach. The method has a high gain in terms of computational efficiency (about 480% speedup compared with 1^0 uniform ray launching).

Index Terms ─ Acceleration, pattern, ray tracing, receiver ball, shooting and bouncing ray, transmitting angle.

I. INTRODUCTION

With the growing demands of electromagnetic environment management (EEM) and wireless communication network design (WCND), the radio wave propagation prediction in outdoor environment attracts more and more attentions recently. Owing to the complexity and large size of the outdoor environment, the ray tracing method rather than other numerical methods such as finite difference time domain method (FDTD) and finite element method (FEM), is often applied in the computation. There are basically two types of ray tracing, namely image method [1] and shooting and bouncing ray (SBR) method [2-3]. Although the image method can find the exact propagation paths from the transmitters to the receivers, however, the computational burden grows exponentially with the number of the facets or the walls in the environment [4]. Thus, its application is limited to very simple environment. The SBR method, on the other hand, is computationally efficient for the complex environment, and can well model the refraction phenomenon. However,

generally the SBR method is less accurate than the image method for it launches a limited number of rays to save the computational time. Therefore, a large number of rays have to be launched to increase the accuracy, which greatly increases the simulation time simultaneously. Thus, a lot of research has been done to save the computational time of the SBR method in the published literatures [5-13]. A group of acceleration techniques incorporate bounding volumes, which reduce the simulation time mainly by decreasing the intersection test calculations [5-7]. In other research activities, the concept of spatial super-sampling is used [8-9]. Nevertheless, the intelligent reduction of the number of the rays is an efficient way to reduce the computational burden [10-13], by using wave-front decomposition method and line search theory.

In this paper, a new method to reduce the number of the rays is proposed. The method focuses on reducing the chance to trace these rays which cannot reach the receivers. The rays with strong possibility to reach the receiver are refined to enhance the accuracy of the simulation. This is achieved by dynamical iterations of transmitting angle and the receiver ball radius. Moreover, the ray assignment is combined with the pattern of the transmitter, leading to more rays are sent out in the direction of the main lobe, which enhances the computational accuracy and efficiency at the same time.

The organization of this paper is as follows. In Section II, the proposed method is introduced. In Section III, some examples of applying the method for studying the outdoor radio wave propagation are presented, and the results are compared with other methods and measurements. The conclusion is drawn in Section IV.

II. METHOD DESCRIPTION

In traditional SBR method, the source is often modeled with a limited number of rays, which are uniformly generated in all directions of the three-dimensional space with identical angular separation [14-16]. However, the transmitting angles that transport electromagnetic power to the receivers constitute only a

small fraction of the total space. If these transmitting angles are specified prior to the start of the high-resolution ray tracing, the refinement rays are launched only through them, and the computational burden decreases significantly. In this paper, it is proposed to find the transmitting angles around the transmitter that transport electromagnetic power to the receivers firstly and then trace the rays in those angles with a high resolution. Some iterative algorithms are applied, which include adaptive receiver ball radius and changeable transmitting angles. As the method used in the commercial software Wireless Insite (WI) [16], the transmitting sphere is often divided by 1^0 angles, and every angle sends out a ray. Thus, there are 64800 rays sent out from the source initially and the number would increase dramatically for modeling scattering and diffraction effects, which depends on the terrain and geometry environment. Thus, the number of rays is increased significantly in complex environment if all the rays from the source should be traced. In our model, however, the transmitting angles are not uniform and are iterated step by step. Moreover, the angles are dependent on the pattern of the transmitter. The angles in the main lobe of the transmitter are assigned much smaller while the angles in other directions are roughly assigned. For example, a diploe has 60^0 beam-width in E plane and is omni-directional in H plane. If 3^0 transmitting angle is applied in the main lobe and 10^0 transmitting angle is applied in other directions, there are only 2832 rays sent out from the source. So, the rays launched initially are less than the traditional method with 1^0 uniform ray launching.

The steps are as follows:

1) Firstly, the radius of the receiver ball is set as half of the distance between the transmitter and the receiver. Such large radius is to guarantee receiving as many rays as possible and thus avoid leaving out the rays that contribute to the total electromagnetic field at the receivers. In other words, this process is to roughly determine the fraction of the sphere around the transmitter from which the rays are needed to be refined.

2) Then, according to the received rays in last step, the iterations of the receiver ball and transmitting angles are implemented. If the ray from the transmitting angle is received, the transmitting angle should be refined, and more rays are emitted from this transmitting angle. During the iteration, the radius of receiver ball is reduced by half until it reaches the threshold, which is 1/10 of the distance between the transmitter and the receiver. This threshold is obtained on the basis of thousands of experiments. The process and flow chart are displayed in Fig. 1 and Fig. 2, respectively.
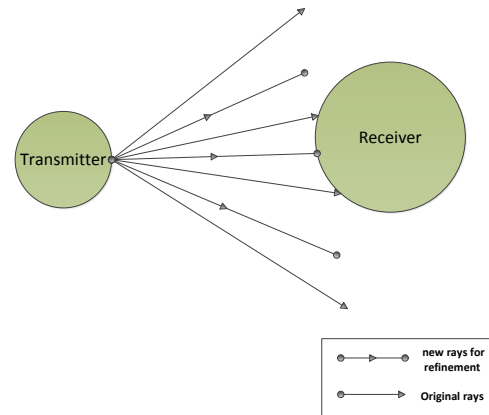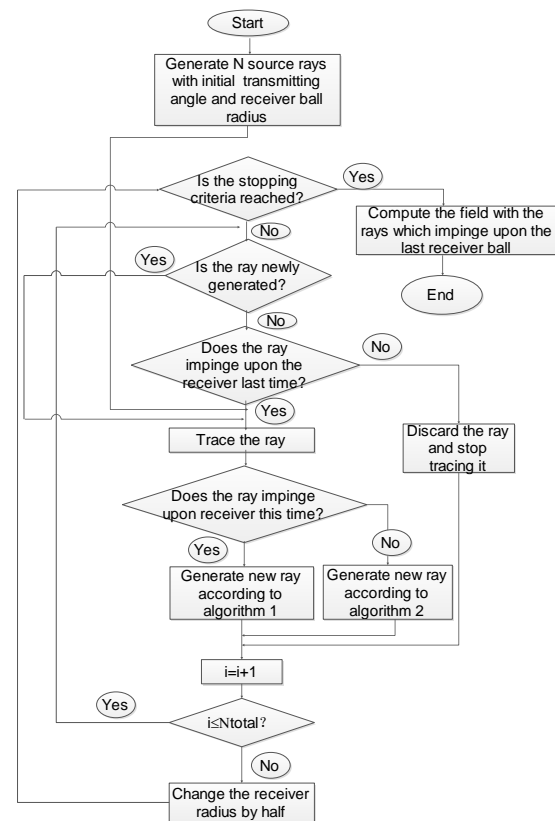

Fig. 1. The iteration of rays.

Fig. 2. Flowchart of the proposed method.

According to Fig. 2, N rays are launched initially, and the receiver ball radius is assigned according to the distance between the transmitter and the receiver. Then these rays are traced one by one and recorded according to this radius. After all these rays are traced, the receiver

ball radius is reduced by half. And then these rays are traced according to the new receiver ball radius. The rays which are not received in the last iteration would be discarded in this iteration. After determining whether the ray illuminates the receiver or not in this iteration, two branches appear: one is "Generate new rays according to algorithm 1" and the other is "Generate new rays according to algorithm 2". In algorithm 1, if the neighboring ray is also received, one more ray is launched between them for refinement. On the other hand, if the neighboring ray is not received, one more ray is launched between them for narrowing the range of the ray generation. In algorithm 2, if the neighboring ray is received, one more ray is launched between them for narrowing the range of the ray generation. If the neighboring ray is not received, no more rays are launched between them. After all the rays are traced and recorded once, the receiver ball radius is reduced by half. The procedure is repeated until the stopping criteria is reached, which is the minimal receiver ball radius.

To provide an efficient way for data storage and path searching, the data structure is designed as shown in Fig. 3. The information of every ray is comprised of four parts, which are starting point, direction vector, flag to mark whether the ray is received or not, and the path information.
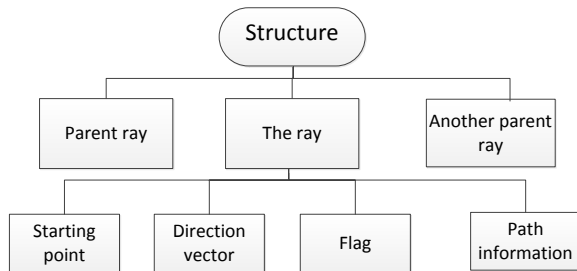

Fig. 3. Data structure for rays.

III. NUMERICAL RESULTS

Two examples in the outdoor scenarios are investigated with the proposed algorithm in this part.

The first scenario is shown in Fig. 4. The transmitter is a planar antenna consisted of a dipole antenna array with a reflector of a base station, whose input power is about 43 dBm, and the gain is about 13 dBi. The center frequency is 935 MHz. Its location in the electric map is x = 207 m, y = 528 m and z = 20 m. It is located on the roof of a building, which is marked with a red triangle. There are three receivers, which are all half wave dipole antennas and marked with the red circles. The receiver 1 is located at the position where x = 382 m, y = 199 m, and z = 2 m. The receiver 2 is located at x = 94 m, y = 0, z = 2 m. The receiver 3 is at x = 1046 m, y = 134 m, z = 2 m. The distances between the transmitter and the three receivers are 373 m, 540 m and 927 m, respectively.

The terrain is loaded from the electric map directly. The conductivity and permittivity of different materials are listed in Table 1.

Fig. 4. The transmitter and receivers in an outdoor scenario.

Table 1: Material properties

Material	Conductivity (S/m)	Relative Permittivity
Concrete wall	0.015	15
Brick wall	0.014	4
Wood	0	5
Asphalt	0.0005	5.72
Ground	0.001	4
River	0	81
Grass	0.085	40
Leaf	0.39	26
Branch	0.39	20

The calculation area is several square kilometers. In such site - specific environment, numerous reflections and diffractions occur. If the transmitting angle is uniformly set as 1^0 according to the traditional method, it takes 8 hours and 13 minutes to complete the calculation. However, if the transmitting angle is uniformly set as 10^0 firstly, and then is refined on the basis of the received rays, the computation time is only 33 minutes. As an improved method for the accuracy, if the transmitting angle is assigned by the pattern of the transmitter, in which the transmitting angle is set as 3^0 in the main lobe direction and 10^0 in other directions firstly, and then is iterated based on the received rays, the computation time is 1 hour and 25 minutes. In this model, the smallest transmitting angle is only 0.0625^0 finally. The eventually received rays and computation accuracy are compared in Table 2.

From Table 2 and Fig. 5, it can be found that the method with adaptive transmitting angle improves the accuracy comparing with the traditional method. Moreover, the accuracy is highest when the transmitting angles are assigned on the basis of the pattern of the transmitter. The results obtained with this improved method are very close to the measurements. The proposed method not only improves the computational accuracy, but also saves a lot of the computational time. The computational efficiency is enhanced by a factor of 4.8 compared with 1^0 uniform ray launching.

Table 2: Comparisons with measurements

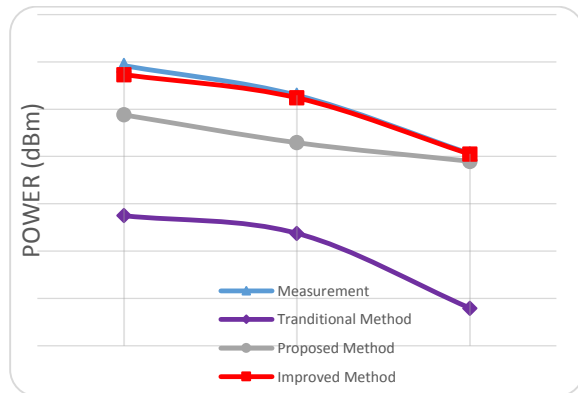|	Measurement	1^0 Fixed	10^0 Iterative	3^0+10^0 Iterative
Received rays at receiver 1		12	8	18
Power at receiver 1	-20.4 dBm	-36.3 dBm	-25.6 dBm	-21.4 dBm
Received rays at receiver 2		10	7	16
Power at receiver 2	-23.5 dBm	-38.1 dBm	-28.5 dBm	-23.8 dBm
Received rays at receiver 3		9	6	15
Power at receiver 3	-29.7 dBm	-46 dBm	-30.5 dBm	-29.8 dBm

Fig. 5. Comparison between different methods and measurements.

To further verify the proposed method, the electric fields at 80 different points are calculated with the proposed method and Wireless Insite (WI) simulation. The results obtained by the proposed method are close with those by the WI simulation. In addition, the electric fields vs. distance and height are investigated in Fig. 6 and Fig. 7, respectively. In Fig. 6, the transmitter with a dipole antenna is located at the position where x = 49 m, y = 193 m, and z = 10 m, and 50 receivers are located at different positions with a 10 m interval with the neighboring one. It can be found that the electric field attenuates with the distance between the transmitter and the receiver. The reason why the electric fields at those points at the beginning are smaller is because that there are not line of sight paths between the receivers and the transmitter owing to the terrain.

In Fig. 7, the transmitter is same as that in Fig. 6, and 30 receivers are located the position where x = -73 m

and y = 108 m. The height of these receivers varies from 10 m to 300 m with 10 m interval. From Fig. 7 we can see that the electric field attenuates with the height since the distance between the transmitter and the receiver increases as the height increases.
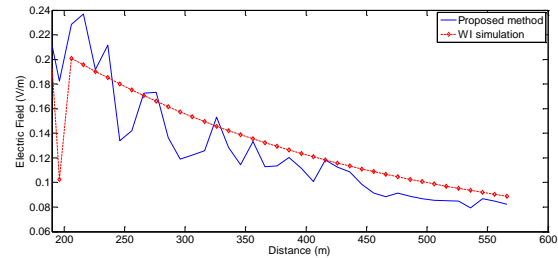
Fig. 6. Electric field vs. distance.
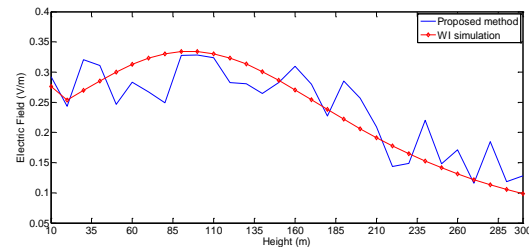
Fig. 7. Electric field vs. height.

IV. CONCLUSION

A new acceleration technique for the ray tracing method was presented. The proposed method is extremely suitable for the wave propagation prediction in the complex and electrically large environment. The results indicated the proposed approach had a speedup of 480% and a high accuracy compared with the measurements and the WI simulation. The proposed method can be applied in the EEM and WCND in practice.

ACKNOWLEDGMENT

REFERENCES

[1] G. Tiberi, S. Bertini, W. Malik, A. Monorchio, D. Edwards, and G. Manara, "Analysis of realistic ultrawideband indoor communication channels by using an efficient ray-tracing based method," *IEEE Trans. Antennas Propag.*, vol. 57, no. 3, pp. 777-785, 2009.

[2] S. Y. Seidel and T. S. Rappaport, "Site-specific propagation prediction for wireless in-building personal communication system design," *IEEE Trans. Veh. Technol.*, vol. 43, no. 4, pp. 879-891, 1994.

[3] F. Weinmann, "UTD shooting-and-bouncing extension to a PO/PTD ray tracing algorithm," *ACES Journal*, vol. 24, no. 3, pp. 281-293, 2009.

[4] F. A. Agelet, A. Formella, and J. M. H. Rabanos, "Efficient ray-tracing acceleration techniques for radio propagation modeling," *IEEE Trans. Veh. Technol.*, vol. 49, no. 6, pp. 2089-2014, 2000.

[5] Z. Yun, M. F. Iskander, and Z. Zhang, "A fast indoor/outdoor ray tracing procedure using combined uniform rectangular and unstructured triangular grids," *IEEE Int. Symp. On Antennas and Propagation*, Salt Lake City, UT, USA, vol. 2, pp. 1134-1137, July 2000.

[6] Z. Yun, Z. Zhang, and M. Iskander, "A ray-tracing method based on the triangular grid approach and application to propagation prediction in urban environments," *IEEE Trans. Antennas Propag.*, vol. 50, no. 5, pp. 750-758, 2002.

[7] M. F. Cátedra, J. Pérez, F. S. Adana, and O. Gutiérrez, "Efficient ray–tracing technique for three–dimensional analyses of propagation in mobile communications: Application to picocell and microcell scenarios," *IEEE Antennas Propagat. Mag.*, vol. 40, no. 2, pp. 15-28, April 1998.

[8] H. Suzuki and A. S. Mohan, "Ray tube tracing method for predicting indoor channel characteristics map," *Electron. Lett.*, vol. 33, no. 17, pp. 1495-1496, 1997.

[9] A. Rajkumar, B. F. Naylor, F. Feisullin, and L. Rogers, "Predicting RF coverage in large environments using ray-beam tracing and partitioning tree represented geometry," *Wirel. Netw.*, vol. 2, no. 2, pp. 143-154, 1996.

[10] V. Mohtashami and A. A. Shishegar, "Efficient shooting and bouncing ray tracing using decomposition of wavefronts," *IET Microw. Antennas Propag.*, vol. 4, no. 10, pp. 1567-1574, 2010.

[11] V. Mohtashami and A. A. Shishegar, "Accuracy and computational efficiency improvement of ray tracing using line search theory," *IET Microw., Antennas Propag.*, vol. 4, no. 9, pp. 1290-1299, 2010.

[12] V. Mohtashami and A. A. Shishegar, "Modified wavefront decomposition method for fast and accurate ray-tracing simulation," *IET Microw., Antennas Propag.*, vol. 6, no. 3, pp. 295-304, 2012.

[13] V. Mohtashami and A. A. Shishegar, "Efficient ultrawideband propagation modelling by using the cubic B-spline function in ray tracing calculations," *IET Microw., Antennas Propag.*, vol. 6, no. 12, pp. 1347-1358, 2012.

[14] C. Saeidi, F. Hodjatkashani, and A. Fard, "New tube-based shooting and bouncing ray tracing method," *International Conference on Advanced Technologies for Communications*, pp. 269-273, 2009.

[15] G. D. Durgin, *Advanced site-specific propagation prediction techniques*, pp. 62-66, 1998.

[16] http://www.remcom.com/wireless-insite

Dan Shi received Ph.D. degree in Electronic Engineering from Beijing University of Posts & Telecommunications, Beijing, China in 2008. She has been an Associate Professor in Beijing University of Posts & Telecommunications. Her interests include electromagnetic compatibility, electromagnetic environment and electromagnetic computation.

Na Lv received her Bachelor degree in Communication Engineering from BUPT in Beijing, China in 2015. Now she is studying for Master degree in Beijing University of Posts and Telecommunications in Beijing, China.

Yougang Gao received his B.S degree in Electrical Engineering from National Wuhan University, China in 1950. He was a Visiting Scholar in Moscow Technical University of Communication and Information in Russia from 1957 to 1959. He is now a Professor and Ph.D. Supervisor in Beijing University of Posts and Telecommunications, China. He has been an Academician of International Informatization Academy of UN since 1994. He was once the Chairman of IEEE Beijing EMC Chapter and Chairman of China National E-Commission for URSI. He has published several books: *Introduction of EMC, Inductive Coupling and Resistive Coupling*, as well as *Shielding and Grounding* (all these books were published by People's Posts and Telecommunications Press). He became an EMP Fellow of US Summa Foundation since 2010.

A Top-down Approach to S-UTD-CH Model

Mehmet B. Tabakcioglu

Electrical and Electronics Engineering Department
Bursa Technical University, Bursa, 16330, Turkey
mehmet.tabakcioglu@btu.edu.tr

Abstract ─ Free space electromagnetic wave propagation is an excessively pretty simple. However, in the reality, there are obstructions like buildings and hills blocking the electromagnetic waves and leading diffraction and reflection, and these obstructions can be modeled as a knife edge or wedge due to using of UHF. Hence, the vital problem is how an electromagnetic wave propagates in multiple diffraction scenario including buildings, trees, hills, cars etc. In order to estimate the field strength or relative path loss of the waves at the receiver, so many electromagnetic wave propagation models have been introduced throughout the century. Ray tracing and numerical integration based propagation models are introduced. In this paper, detailed information is provided about S-UTD-CH (Slope UTD with Convex Hull) model. Particularly, in the transition zone, the S-UTD-CH model can be applied to multiple diffraction scenarios. In addition, Fresnel zone concept, convex hull and slope UTD models are fundamentals of the S-UTD-CH model. Moreover, in terms of computation time and accuracy, the S-UTD-CH model is conceived an optimum model. Furthermore, verification of S-UTD-CH model is made by means of FEKO, which is a comprehensive electromagnetic simulation software tool by Altair.

Index Terms ─ Diffraction, FEKO, radio wave propagation, Ray-tracing, S-UTD-CH model.

I. INTRODUCTION

In order to establish high precision and time efficient communication networks and radio broadcasting systems too many electromagnetic wave propagation models have been introduced throughout the century. At first, geometrical optic model observing some physical events like reflection, refraction and enlightenment is proposed [1]. The geometrical optic (GO) model based on particle property of the light. That is, the light propagates from the source as particle and there are sharp shadow boundaries. The geometrical optic model does not work successfully in the case of multiple-diffraction. In real environment, there are obstacles such as buildings, hills, trees and cars etc., can cause reflection, refraction and diffraction. Thanks to using ultra-high frequency (UHF)

electromagnetic waves, the buildings, trees and hills in the environment can be modeled as knife edge and wedge structures, respectively. Geometrical theory of diffraction (GTD) model is introduced by Keller [2]. The GTD model is an extension to the GO model by adding diffracted waves [3]. The GTD model fails to calculate the field strength in the vicinity of the optical boundaries [4]. In other words, the GTD model is unsuccessful to calculate the relative path loss in the case of that source, diffraction and observation points are in the same line [5]. The GTD model finds the acceptable results in the case that the size of obstacle is less than the wavelength of the incident wave [6]. In 1966, Deygout proposed a new multiple-diffraction propagation model for knife-edge structures [7]. This model is valid for the environment including limited number of knife-edge structures [8]. Besides this model fails to calculate the relative path loss in the case of that the knife edges are close to each other [9]. Uniform theory of diffraction (UTD) model is a high frequency asymptotic technique introduced by [10] and computes the field strength at the receiver in a very short time. The UTD model removes some of the failure of GTD model in the vicinity of the shadow boundary. If an obstacle blocks the frontal obstacle, the UTD model fails to calculate the relative path loss accurately [11, 12]. That is, if the heights of the obstacles are close to each other, the UTD model gives inaccurate predictions. In order to remove the failure of the UTD model, slope UTD model is proposed [13-16]. This model is more exact than the GO, GTD and UTD models. It is based on adding of derivatives of incident fields. Some simulations are made in order to verify the S-UTD model with Vogler's model [17]. Vogler model is an accurate and numerical integration based well-known model. If the number of obstacle is greater than 10, the S-UTD model fails to predict the field strength accurately, and leads so much complexity and requires so much computation time. That is, up to 10 diffractions, the S-UTD model come up with remarkable, accurate, meaningful and time-efficient results [18-20]. In order to overcome time efficiency and exactness deficiencies of slope UTD model, another UTD-based, ray theoretical, time-efficient and accurate model is proposed [19-23].

The proposed model called by S-UTD-CH, abbreviated form of Slope UTD with Convex Hull. In fact S-UTD-CH model is not a new model and only combination of the Slope UTD model and Convex-Hull model. The rest of paper explains S-UTD-CH model and give comparison results of UTD based models with regard to computation time and accuracy of prediction. Another comparison is made by using CAD FEKO electromagnetic simulation software tool.

II. S-UTD-CH MODEL

Electric field behind an obstacle can be calculated by formula in [24]:

$$E = \left[E_i D + \frac{\partial E_i}{\partial n} d_s\right] A(s) e^{-jks}, \qquad (1)$$

where E_i is incident field, $A(s)$ is the spreading factor, D is the amplitude diffraction coefficient, k is the wave number, d_s is the slope diffraction coefficient, n represents the normal and s is a distance. The obstacles like buildings and hills can be modelled as a knife edge, wedge or cylinder thanks to using UHF waves. In the knife-edge case diffraction coefficient [16] is expressed by:

$$D(\alpha) = -\frac{e^{-j\pi/4}}{2\sqrt{2\pi k}\cos(\alpha/2)} F[x], \qquad (2)$$

where, k is the wave number, $F[x]$ is the transition function given in [25], α is an angle between the incident and the diffracted waves. $A(s)$ is the spreading factor is given by:

$$A(s) = \sqrt{\frac{s_0}{s_1(s_1+s_0)}}, \qquad (3)$$

where, s_0 is the total distance before the last diffracting obstacle, whereas s_1 is the distance after the last diffracting obstacle as shown in Fig. 1.
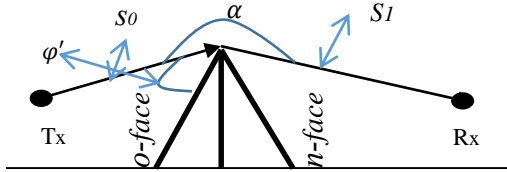

Fig. 1. Diffraction geometry.

By taking into account the wedge structure, polarisation effects have to be added. The amplitude diffraction coefficients [26] for horizontal and vertical polarization are given by:

$$D_s = R_{0s}R_{ns}D_1 + D_2 + R_{0s}D_3 + R_{ns}D_4, \qquad (4)$$
$$D_h = R_{0h}R_{nh}D_1 + D_2 + R_{0h}D_3 + R_{nh}D_4, \qquad (5)$$

where, h and s indices stand for vertical and horizontal polarisations. R is the reflection coefficient, 0 and n denote zero and n faces of the wedge and they are illustrated in Fig. 1.

$D_{1,2,3,4}$ are in [27] are given by:

$$D_i = \frac{-e^{-j\pi/4}}{2n\sqrt{2\pi k}}\cot(\psi(i)) F\left(2kLn^2\sin^2(\psi(i))\right), \quad (6)$$

$$\psi(1)=\frac{\pi+\varphi-\varphi'}{2n}, \psi(2)=\frac{\pi-\varphi+\varphi'}{2n}, \psi(3)=\frac{\pi-\varphi-\varphi'}{2n}, \psi(4)=\frac{\pi+\varphi+\varphi'}{2n},$$

where, n is a number ($n = 2 - \beta/\pi$) ranging in [0-2]. β is the internal angle and L is the distance parameter calculated via using continuity equations.

Due to using wedge structure, the reflected fields have to be taken into account. Thus, the reflection coefficients in [28] are given by:

$$R_{0s} = \frac{\sin(\varphi')-\sqrt{\varepsilon_r-\cos^2(\varphi')}}{\sin(\varphi')+\sqrt{\varepsilon_r-\cos^2(\varphi')}}, \qquad (7)$$

$$R_{0h} = \frac{\varepsilon_r\sin(\varphi')-\sqrt{\varepsilon_r-\cos^2(\varphi')}}{\varepsilon_r\sin(\varphi')+\sqrt{\varepsilon_r-\cos^2(\varphi')}}, \qquad (8)$$

$$R_{ns} = \frac{\sin(n\pi-\varphi)-\sqrt{\varepsilon_r-\cos^2(n\pi-\varphi)}}{\sin(n\pi-\varphi)+\sqrt{\varepsilon_r-\cos^2(n\pi-\varphi)}}, \qquad (9)$$

$$R_{nh} = \frac{\varepsilon_r\sin(n\pi-\varphi)-\sqrt{\varepsilon_r-\cos^2(n\pi-\varphi)}}{\varepsilon_r\sin(n\pi-\varphi)+\sqrt{\varepsilon_r-\cos^2(n\pi-\varphi)}}. \qquad (10)$$

As aforementioned, the S-UTD-CH model is combination of two previously proposed S-UTD (Slope UTD) and CH (Convex Hull) models. Convex hull model is introduced and applied in [29, 30]. A convex hull is constructed by using the Fresnel zone. The Fresnel zone, an ellipsoid region between the transmitting and receiving antennas, is commonly used in radio planning tools [31] as depicted in Fig. 2.
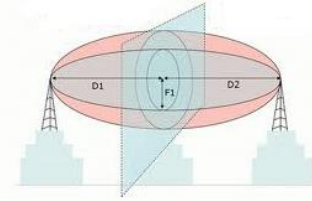
Fig. 2. Fresnel zone.

F_1 is the radius of the first Fresnel zone expressed by:

$$F_1 = \sqrt{\frac{ncD_1D_2}{f(D_1+D_2)}}, \qquad (11)$$

where ($n=1$) is the order of the Fresnel zone and c is the speed of light, D_1 and D_2 are the distance before and after the obstacle, respectively.

Most of the wave emits from the transmitter propagates in Fresnel zone. If the obstacle does not disrupt the Fresnel zone, this obstacle would be excluded from the scenario due to so little contribution on the receiver. Fresnel zone disruption by tree and house can be seen in Fig. 3.
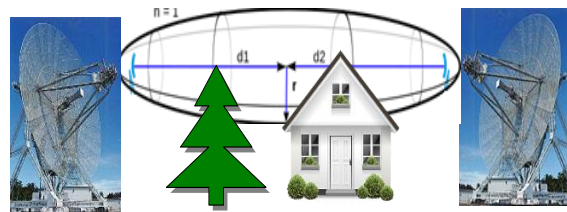
Fig. 3. Fresnel zone disruption.

Convex hull, a polygon between the transmitter and the receiver, is constructed by using the fresnel zone concept [32].

Firstly, the first fresnel zone is drawn between the tranmitter and the receiver. Some obstacles placed outside of the zone are excluded from the scenario. Then, the highest obstacle intersecting the line between the transmitter and the receiver in the scenario is selected. Next, secondary fresnel zones are drawn between the transmitter and the highest obstacle and between the receiver and the highest obstacle. Afterthat, the obstacles placed outside of the secondary zones are excluded from the scenario again. Finally, convex hull is constructed with remained obstacles as illustrated in Figs. 4 (a-b).

Fig. 4. Convex hull construction.

Exclusion of some unsuccessful diffracting obstacles alleviates the computation time and complexity by not promising from the accuracy of predicted field.

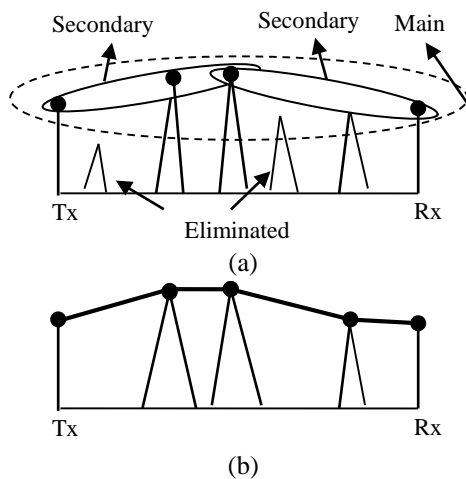S-UTD-CH mechanism can be explained as followed. Firstly, convex hull is constructed by utilising the Fresnel zone concept. Secondly, all the ray paths emanate from the transmitter and ends on the receiver are determined. Finally, Slope UTD model runs for these ray paths and predicts the field strength.

III. COMPARISON OF THE MODELS

A lot of comparisons have been carried out among the models for accuracy and/or computation time [33-38]. Ray-theoretical electromagnetic wave propagation models, which are UTD, S-UTD and S-UTD-CH, are compared with regard to computation time and accuracy of prediction of relative path loss in this section. In the case of that there are fewer than 11 diffractions in the scenario the S-UTD model is envisioned the reference model according to accuracy of prediction. The scenario of comparisons is illustrated in Fig. 5.
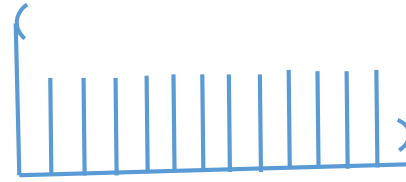

Fig. 5. Test scenarios for comparison.

As shown in Fig. 5, there are 10 obstacles in given scenario, and the obstacles and the receiving antenna heights are 20 m and 1.5 m, respectively. All the distances between obstacles and antennas are deployed equally spaced as 25 m and 50 m. The operational frequencies are 100, 400, 900 and 1800 MHz. The height of transmitter is selected as 10, 15, 20, 25 and 30 m.

In the first case, the operational frequency is 100 MHz and the distance between the obstacles is 25 m. The transmitter heights are selected as 10, 15, 20, 25 and 30 m, respectively. In order to show how the relative path loss is affected by the change of transmitter height, simulation is performed, and the results are demonstrated in Table 1.

In Table 1, the first column shows the transmitter height. Next three columns indicate the relative path loss of S-UTD-CH, S-UTD and UTD models, respectively. The latter three columns give the computation time of mentioned models. The eliminated obstacle number in the S-UTD-CH model is shown in the last column.

The UTD model requires the least computation time. Also, in the highly elevated transmitting antenna case (30 m), due to one obstacle elimination the S-UTD-CH model has relatively shorter computation time than S-UTD model. In this case, computation time of the S-UTD model is 2118.35 s, whereas the computation time of the S-UTD-CH model is 354.18 s. However, the difference between the relative path losses of models is only 0.06 dB. The S-UTD-CH model can be used instead of the S-UTD model with relatively less computation time. It is obvious that the S-UTD model needs the highest computation time.

In the second case, the operational frequency is 100 MHz and the distance between the obstacles is 50 m. The transmitter heights are selected as 10, 15, 20, 25 and 30 m, respectively. In order to show how the relative path loss is affected by the change of the distance between obstacles, simulation is performed, and the results are shown in Table 2.

In Table 2, the first column shows the transmitter height. Next three columns indicate the relative path loss of S-UTD-CH, S-UTD and UTD models, respectively. The latter three columns give the computation time of mentioned models. The eliminated obstacle number in the S-UTD-CH model is shown in the last column.

The UTD model requires the least computation

time. Due to that all the obstacles are in the Fresnel zone of the transmitter, there is no eliminated obstacle in the S-UTD-CH model. This situation leads the same computation times for the S-UTD-CH model and the S-UTD model.

In the third case, the transmitter height is 30 m and the distance between the obstacles is 25 m. The operational frequencies are selected as 100, 400, 900 and 1800 MHz, respectively. In order to indicate how the relative path loss is affected by the change of operational frequency, simulation is performed, and the results are illustrated in Table 3.

In Table 3, the first column shows the operational frequency. Next three columns indicate the relative path loss of S-UTD-CH, S-UTD and UTD models, respectively. The latter three columns give the computation time of mentioned models. The eliminated obstacle number in the S-UTD-CH model is shown in the last column.

The S-UTD model requires the most computation time with ultimate in accuracy. Also, in highly elevated (30 m) transmitting antenna cases, there is obstacle elimination. Moreover, as the operational frequency increases, eliminated obstacle number increases too. There is almost no difference between prediction accuracy of S-UTD and S-UTD-CH models. In these cases S-UTD-CH model can be used in multiple diffractions with regard to less computation time. Furthermore, as the operational frequency increases, predicted relative path loss decreases.

The second proof is made by using FEKO electromagnetic simulation software tool. The test scenario is given in Fig. 6.
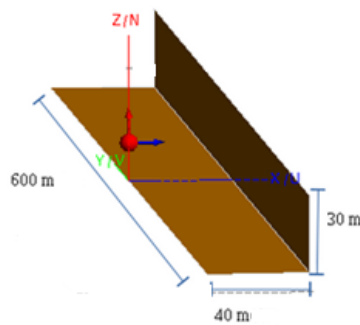
Fig. 6. The second test scenario.

As can be seen in the Fig. 6, the transmitting antenna height is 15 m, and at a 40 m distance from the transmitter there is an obstacle whose height is 30 m. The operational frequency is 900 MHz. By using the FEKO coverage map is drawn in Fig. 7.
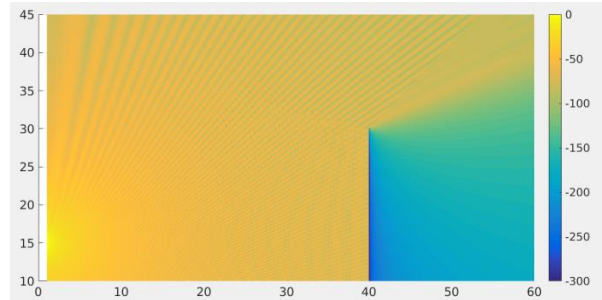
Fig. 7. FEKO simulation results.

As it is seen in the Fig. 7, in front of the obstacle there are LOS, ground reflected, obstacle reflected and backward diffracted waves. Thanks to that these rays are in different phases, interference pattern is observed in front of the obstacle. Moreover in behind of the obstacle, only diffracted waves are propagated.

Coverage map also generated with the S-UTD-CH model for the same scenario and this map is illustrated in Fig. 8.
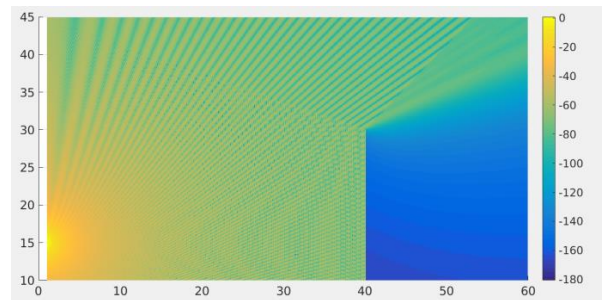
Fig. 8. S-UTD-CH simulation results.

As can be seen in the Fig. 8, the same interference pattern is obtained behind and in front of the obstacle. Behind the obstacle there is some difference resulted from FEKO design.

Table 1: 1st Case (f = 100 MHz, d = 25 m)

Transmitter Height	S-UTD-CH RPL (dB)	S-UTD RPL (dB)	UTD RPL (dB)	S-UTD-CH Time (s)	S-UTD Time (s)	UTD Time (s)	Eliminated Obstacle
10	-52,91	-52,91	-86,82	1355,95	1319,92	4,16	0
15	-47,02	-47,02	-82,19	1303,26	1323,15	4,08	0
20	-38,98	-38,98	-75,9	2075,16	1953,81	5,62	0
25	-32,12	-32,12	-35,36	2044,41	1995,04	5,53	0
30	-27,99	-27,93	-29,49	354,18	2118,35	5,83	1

Table 2: 2nd Case (f = 100 MHz, d = 50 m)

Transmitter Height	S-UTD-CH RPL (dB)	S-UTD RPL (dB)	UTD RPL (dB)	S-UTD-CH Time (s)	S-UTD Time (s)	UTD Time (s)	Eliminated Obstacle
10	-46,56	-46,56	-81,7	1363,38	1361,64	4,29	0
15	-41,63	-41,63	-77,86	1303,6	1266,21	4,16	0
20	-30,8	-30,8	-35,33	2137,49	2119,73	5,73	0
25	-35,78	-35,78	-73,23	2122,38	2150,01	5,54	0
30	-26,80	-26,80	-29,35	2116,67	2150,26	5,88	0

Table 3: 3rd Case (Transmitter height = 30 m, d = 25 m)

Frequency (MHz)	S-UTD-CH RPL (dB)	S-UTD RPL (dB)	UTD RPL (dB)	S-UTD-CH Time (s)	S-UTD Time (s)	UTD Time (s)	Eliminated Obstacle
100	-27,99	-27,93	-29,49	354,18	2118,35	5,83	1
400	-30,43	-30,34	-30,45	55,12	2136,95	5,63	2
900	-31,78	-31,68	-31,57	2,04	2076,68	5,66	4
1800	-33,44	-33,67	-33,24	0,61	2101,19	5,54	5

IV. CONCLUSIONS

A top-down approach for S-UTD-CH model is presented in this study. A great many simulations indicates that there is tremendous contribution to UTD model in the case of multiple transition region diffraction. Adding the derivative of incoming field removes the discontinuity problem of UTD model in the transition zone. Actually, the UTD model can be used to predict the field strength or relative path loss in the rural or single diffraction case with a relatively short computing time. Next, the S-UTD model has ultimate accuracy with relatively long computing time in the multiple diffraction including more than 10 obstacles. Besides, there is a tradeoff between the accuracy of prediction and computation time. Afterwards, Slope UTD with a Convex-Hull (S-UTD-CH) model is based on the selection mechanism, based on the Fresnel zone concept and convex hull model, for unsuccessful obstacles. The S-UTD-CH model provides accurate results and short computation time in multiple-diffraction scenarios including more than 10. Moreover, due to the elevated transmitting antenna and higher operational frequency cases the relative path loss of models and contribution to the UTD model are reduced. Furthermore, verification of the S-UTD-CH model is provided by FEKO electromagnetic wave simulation software tool. To sum up, the S-UTD-CH model could be used in radio planning tool, broadcasting systems and prediction algorithms thanks to higher accuracy of prediction and less computation time.

REFERENCES

[1]   V. A. Borovikov and B. E. Kinber, *Geometrical Theory of Diffraction*. Institution of Electrical Engineers, London, UK, 1994.

[2]   J. B. Keller, "Geometrical theory of diffraction," *Journal of the Optical Society of America*, vol. 52, no. 2, pp. 116-130, 1962.

[3]   C. A. Balanis, L. Sevgi, and P. Y. Ufimtsev, "Fifty years of high frequency diffraction," *International Journal of RF and Microwave Computer-Aided Engineering*, vol. 23, no. 4, pp. 1-6, 2013.

[4]   M. Schneider and R. J. Luebbers, "A uniform double diffraction coefficient," *Antennas and Propagation Society International Symposium*, San Jose, CA, vol. 3, pp. 1270-1273, June 1989.

[5]   R. J. Luebbers, "Finite conductivity uniform GTD versus knife edge diffraction in prediction of propagation path loss," *IEEE Transactions on Antennas Propagation*, vol. 32, no. 1, pp. 70-76, 1984.

[6]   L. J. Graeme, *Geometrical Theory of Diffraction for Electromagnetic Waves*. Institution of Electrical Engineers, London, UK, 1976.

[7]   J. Deygout, "Multiple knife-edge diffraction of microwaves," *IEEE Transactions on Antennas Propagation*, vol. 14, no. 4, pp. 480-489, 1966.

[8]   J. Walfisch and H. L. Bertoni, "A theoretical model of UHF propagation in urban environment," *IEEE Transactions on Antennas Propagation*, vol. 36, no. 12, pp. 1788-1796, 1988.

[9]   C. Tzaras and S. R. Saunders, "Comparison of multiple-diffraction models for digital broadcasting coverage prediction," *IEEE Transactions on Broadcasting*, vol. 46, no. 3, pp. 221-226, 2000.

[10] R. G. Kouyoumjian and P. H. Pathak, "Uniform geometrical theory of diffraction for an edge in a perfectly conducting surface," *Proceedings of IEEE*, vol. 62, no. 11, pp. 1448-1461, 1974.

[11] E. Yazgan, "A simple formulation of UTD for some reflector antennas," *International Journal of*

Electronics, vol. 66, no. 2, pp. 283-288, 1989.

[12] A. Kara and E. Yazgan, "Roof shape modelling for multiple diffraction loss in cellular mobile communication systems," *International Journal of Electronics*, vol. 89, no. 10, pp. 753-758, 2002.

[13] J. B. Andersen, "Transition zone diffraction by multiple edges," *IEEE Proceedings Microwave Antennas and Propagation*, vol. 141, no. 5, pp. 382-384, 1994.

[14] J. B. Andersen, "UTD multiple-edge transition zone diffraction," *IEEE Transactions on Antennas and Propagation*, vol. 45, no. 7, pp. 1093-1097, 1997.

[15] K. Rizk, R. Valenzuela, D. Chizhik, and F. Gardiol, "Application of the slope diffraction method for urban microwave propagation prediction," *IEEE Vehicular Technology Conference*, Ottawa, Ont., vol. 2, pp. 1150-1155, May 1998.

[16] C. Tzaras and S. R. Saunders, "An improved heuristic UTD solution for multiple-edge transition zone diffraction," *IEEE Transactions on Antennas Propagation*, vol. 49, no. 12, pp. 1678-1682, 2001.

[17] L. Vogler, "An attenuation function for multiple knife-edge diffraction," *Radio Science*, vol. 17, no. 6, pp. 1541-1546, 1982.

[18] A. Kara, E. Yazgan, and H. L. Bertoni, "Limit and application range of slope diffraction for wireless communication," *IEEE Transactions on Antennas Propagation*, vol. 51, no. 9, pp. 2514-2514, 2003.

[19] M. B. Tabakcioglu and A. Kara, "Comparison of improved slope UTD method with UTD based methods and physical optic solution for multiple building diffractions," *Electromagnetics*, vol. 29 no. 4, pp. 303-320, 2009.

[20] M. B. Tabakcioglu and A. Kara, "Improvements on slope diffraction for multiple wedges," *Electromagnetics*, vol. 30, no. 3, pp. 285-296, 2010.

[21] M. B. Tabakcioglu, D. Ayberkin, and A. Cansiz, "Comparison and analyzing of propagation models with respect to material, environmental and wave properties," *ACES Journal*, vol. 29, no. 6, pp. 486-491, 2014.

[22] M. B. Tabakcioglu and A. Cansiz, "Application of S-UTD-CH model into multiple diffraction scenarios," *International Journal of Antennas and Propagation*, vol. 2013, pp. 1-5, 2013.

[23] M. B. Tabakcioglu, "S-UTD-CH model in multiple diffractions," *International Journal of Electronics*, vol. 103, no. 5, pp. 765-774, 2015.

[24] R. J. Luebbers, "A heuristic UTD slope diffraction coefficient for rough lossy wedges," *IEEE Transactions on Antennas and Propagation*, vol. 37, no. 3, pp. 206-211, 1989.

[25] D. A. McNamara, C. V. Pistorious, and J. A. G. Malherbe, *Introduction to the Uniform Geometrical Theory of Diffraction*. Boston, MA: Artech House, 1990.

[26] K. Karousos and C. Tzaras, "Multi time-domain diffraction for UWB signals," *IEEE Trans. Antenna Propagation*, vol. 56, no. 5, pp. 1420-1427, 2008.

[27] G. Koutitas and C. Tzaras, "A slope UTD solution for a cascade of multishaped canonical objects," *IEEE Trans. Antenna Propagation*, vol. 54, no. 10, pp. 2969-2976, 2008.

[28] A. Tajvidy and A. Ghorbani, "A new uniform theory-of-diffraction-based model for the multiple building diffraction of spherical waves in microcell environments," *Electromagnetics*, vol. 28, no. 5, pp. 375-387, 2008.

[29] O. M. Bucci, "The experimental validation of a technique to find the convex hull of scattering systems from field data," *IEEE Antennas and Propagation Symposium*, pp. 539-542, 2003.

[30] H. K. Chung and H. L. Bertoni, "Application of isolated diffraction edge method for urban microwave path loss prediction," *IEEE Vehicular Tech. Conf.*, pp. 0205-209, 2003.

[31] H. L. Bertoni, *Radio Propagation for Modern Wireless Systems*. Prentice Hall, 2000.

[32] G. Liang and H. L. Bertoni, "A new approach to 3-D ray tracing for propagation prediction in cities," *IEEE Transactions on Antennas and Propagation*, vol. 46, no. 6, pp. 853-863, 1998.

[33] O. Ozgun and L. Sevgi, "Comparative study of analytical and numerical techniques in modeling electromagnetic scattering from single and double knife-edge in 2D ground wave propagation problems," *ACES Journal*, vol. 27, no. 5, pp. 376-388, 2012.

[34] A. Skarlatos, R. Schuhmann, and T. Weiland, "Simulation of scattering problems in time domain using a hybrid FDTD UTD formulation," *The 19th Annual Review of Progress in Applied Computational Electromagnetics*, 2003.

[35] P. Persson, "Modeling conformal array antennas of various shapes using uniform theory of diffraction (UTD)," *ACES Journal*, vol. 21, no. 3, pp. 305-317, 2006.

[36] G. Apaydin and L. Sevgi, "A novel wedge diffraction modeling using method of moments (MoM)," *ACES Journal*, vol. 30, no. 10, pp. 1053-1058, 2015.

[37] M. A. Uslu, G. Apaydın, and L. Sevgi, "Double tip diffraction modeling: Finite difference time domain vs. method of moments," *IEEE Trans. on Antennas and Propagat.*, vol. 62, no. 12, pp. 6337-6343, 2014.

[38] O. Ozgun and L. Sevgi, "Double-tip diffraction modeling: Finite element modeling (FEM) vs. uniform theory of diffraction (UTD)," *IEEE Trans. on Antennas and Propagat.*, vol. 63, no. 6, pp. 2686-2693, 2015.

Mehmet Baris Tabakcioglu was born in 1981. He received B.S. degree in Physics from Middle East Technical University in 2005. Then he received the M.S. degree in Electrical and Electronics Engineering from Atılım University in 2009. After that he received the Ph.D degree in Electrical and Electronics Engineering from Atatürk University in 2013.

His currently research area is wave diffraction, reflection and propagation. He is currently working at Bursa Technical University in Electrical and Electronics Engineering department.

Modeling of Diffraction Effects in Urban Radiowave Propagation

Ozlem Ozgun

Department of Electrical and Electronics Engineering
Hacettepe University, Ankara, 06800, Turkey
ozlem@ee.hacettepe.edu.tr

Abstract ─ A comparative study of some theoretical and numerical models is presented in the solution of two-dimensional urban radiowave propagation problems. The path loss is computed by GO+UTD (geometric optics + uniform theory of diffraction), two-way SSPE (split step parabolic equation) and the diffracting screens models, and the results are compared through numerical simulations. The diffracted fields that are obtained by the GO+UTD model are demonstrated. Computational aspects of the models are briefly discussed.

Index Terms ─ Diffracting screens model, geometric optics (GO), GO+UTD tool, path loss, PETOOL, two-way split step parabolic equation (SSPE), uniform theory of diffraction (UTD), urban propagation.

I. INTRODUCTION

The planning and development of modern mobile communications systems requires accurate and efficient models for urban radiowave propagation, which aim to predict losses in radio signals in different environments. Since the domain of interest is very large in wavelengths, numerical methods like method of moments, finite difference and finite element methods (as well as some commercial software like HFSS, CST, etc.) cannot be employed due to large number of unknowns required to solve such long-range propagation problems. Some empirical models have been developed, which try to estimate propagation losses based on curve-fitting of measured field response [1,2]. However, the main limitation of these models is that they are accurate for specific parameters and environments, and they do not become valid in different propagation scenarios. To overcome the difficulties in empirical models, some theoretical models have been proposed in which the environment is represented by some canonical parameters/geometries, such as building geometry, spacing, etc. For example, Longley-Rice model [3], Bullington model [4], Lee's model [5], and Walfisch and Bertoni model [6,7] have been used in the literature.

There are also some theoretical models, so-called high frequency techniques, such as geometrical optics (GO) [8], geometrical theory of diffraction (GTD) [9],

uniform theory of diffraction (UTD) [10], physical optics (PO) [11] and physical theory of diffraction (PTD) [12], which can be used to model urban propagation problems. These techniques use ray-based approach and provide accurate formulations to account for main propagation mechanisms, such as reflection, refraction and diffraction. In Fig. 1, reflection and diffraction of field rays are illustrated in a typical urban propagation problem involving a series of buildings. The GO approach computes incident and reflected fields, but cannot include diffracted fields. Keller extended GO to include diffraction effects and developed GTD by defining a diffraction coefficient for a perfectly conducting wedge by asymptotically evaluating Sommerfelds' diffraction integral. To overcome the singularities along the incident and reflection shadow boundaries (ISB and RSB) in the GTD model, UTD was developed to achieve smoother wave behavior along the shadow boundaries. The PO model estimates the field and current on surface and integrates the current over the surface to determine the scattered field. Similar to GO, the PO does not include the diffracted fields. The PTD method includes the diffracted fields by using non-uniform (fringe) edge currents on the surface. Recently, a MATLAB-based tool (called GO+UTD) was developed to model radiowave propagation by combining the GO and UTD models [13,14]. Also, a MATLAB-based tool for diffraction modeling of a wedge problem was proposed [15,16].

Other than these empirical and theoretical models, parabolic equation (PE) method is perhaps the most efficient numerical method to model arbitrary refraction effects and terrain irregularities in long-range propagation problems [17]. It is based on an approximate form of the Helmholtz wave equation, and can be solved by a marching type algorithm. Therefore, long range propagation problems can easily be solved in a fast and accurate manner. However, one of the limitations of the standard PE is that it considers only forward propagating waves. For short range problems, as well as the problems involving multiple reflections and diffractions because of hills and valleys with steep slopes, the standard PE fails to model multipath effects. To model backward

propagating waves in an irregular terrain profile, two-way PE model was proposed [18] and implemented as a MATLAB-based tool (called PETOOL) [19]. Although the PE method can inherently model diffracted fields, it cannot separate the diffracted field from the total field.

The organization of this paper is as follows: the GO+UTD, the two-way SSPE and the diffracting screens models are summarized in Sections II, III and IV, respectively. Numerical examples are presented in a comparative manner in Section V. Finally, some conclusions are drawn in Section VI.
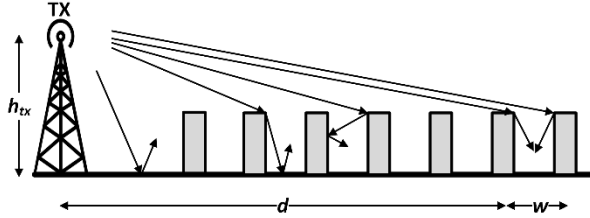

Fig. 1. Radiowave propagation in urban region.

II. GO+UTD MODEL

The GO+UTD toolbox is based on an algorithm that divides the terrain into a number of line segments, and superposes the incident and multiple reflected and diffracted fields by repeatedly utilizing the GO and UTD principles according to different line-of-sight (LOS) conditions [13]. First, direct ray is computed for each illuminated point. Line segments illuminated by the source and their image sources are determined. Reflected rays are computed by radiating these image sources. This process is continued to account for higher-order reflections until the reflected rays escape from the domain, or until the contribution of reflected rays becomes negligible according to a certain threshold criterion. In addition, diffracted fields from sharp tips are computed. The tips behave as new source locations, and the reflected rays of the diffracted rays are computed by obtaining image sources similar to the above steps.

The GO method is illustrated in Fig. 2 (a), where a cylindrically diverging line source is above a flat surface. Assuming that u denotes the electric or magnetic field in horizontal (soft) or vertical (hard) polarizations, respectively, the total field (u^t) in the illuminated part of the surface is the sum of direct/incident field (u^i) and the reflected field (u^r) emanating from the image source, which are given by (assuming $e^{j\omega t}$ time dependence):

$$u^i = u_0 e^{-jkr}/\sqrt{r} , \quad (1)$$

$$u^r = u^i\big|_{at P} R_{s,h} \sqrt{\frac{d_1}{d_1+d_2}} e^{-jkd_2} = u_0 R_{s,h} \frac{e^{-jk(d_1+d_2)}}{\sqrt{d_1+d_2}} , \quad (2)$$

where u_0 is the amplitude of the incident field, $k = 2\pi/\lambda$ is the wavenumber (λ is the wavelength), and $R_{s,h}$ is the reflection coefficient of the surface, which is -1 and $+1$

for soft and hard polarizations, respectively.
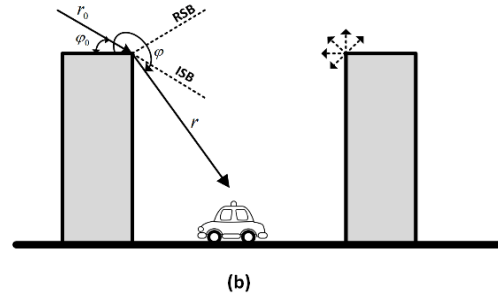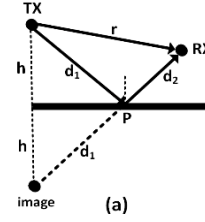
Fig. 2. Illustration of the GO+UTD modeling in the close vicinity of the receiver: (a) GO and (b) UTD.

The UTD method is used to model diffracted fields, and is described by considering the geometry in Fig. 2 (b), which shows the region between two buildings. If the corners of the building are illuminated by either incident field or reflected field from other surfaces, the diffracted fields for each corner are computed and superposed to determine the field at a receiver point. Consider a single corner whose interior wedge angle is $\pi/2$, as shown in the figure. The tip-to-source distance and the source angle are denoted by r_0 and φ_0, respectively; whereas the tip-to-observer distance and the observation angle are represented by r and φ, respectively. The exterior wedge angle is set to $\alpha = 3\pi/2$ to model a right-angled building, and can be set to any value for arbitrary geometries. The diffracted field in UTD is determined by:

$$u^d_{s,h} = u^i D_{s,h} e^{-jkr}/\sqrt{r} , \quad (3)$$

where u^i is the incident field at the tip of the wedge, and $D_{s,h}$ is the diffraction coefficient for soft and hard polarizations, given as follows [10]:

$$D_{s,h} = \frac{-e^{-j\pi/4}}{2n\sqrt{2\pi k}} \{[\cot\left(\frac{\pi-\xi^-}{2n}\right)F(kLg^+\xi^-)$$
$$+\cot\left(\frac{\pi+\xi^-}{2n}\right)F(kLg^-\xi^-)]$$
$$\mp[\cot\left(\frac{\pi-\xi^+}{2n}\right)F(kLg^+\xi^+)+\cot\left(\frac{\pi+\xi^+}{2n}\right)F(kLg^-\xi^+)]\}$$
$$(4)$$

where ($-$) and ($+$) are for soft and hard polarizations, respectively. Here, $n = \alpha/\pi$, $\xi^+ = \varphi + \varphi_0$, $\xi^- = \varphi - \varphi_0$,

and $F(X)$ is the Fresnel integral given by:

$$F(X) = 2j\sqrt{X}\,e^{jX}\int_{\sqrt{X}}^{\infty} e^{-j\tau^2}\,d\tau\,,\qquad(5)$$

and L and $g^{\pm}$ are expressed as follows:

$$L = \frac{rr_0}{r+r_0}\,,\qquad g^{\pm}(\xi) = 2\cos^2\left(\frac{2n\pi N^{\pm}-\xi}{2}\right),\qquad(6)$$

where $N^{\pm}=(\pm\pi+\xi)/2n\pi$ are the integers that most closely satisfy this expression. Since the cotangent functions possess singularities at the shadow boundaries, they can be replaced by (for small $\varepsilon\to 0$):

$$\begin{aligned}&\cot\left(\frac{\pi\pm\beta}{2n}\right)F\left(kLg^{\pm}\xi\right)\\&\approx n\left[\sqrt{2\pi kL}\,\mathrm{sgn}(\varepsilon)-2kL\varepsilon e^{-j\pi/4}\right]e^{-j\pi/4}\end{aligned}\qquad(7)$$

III. TWO-WAY SSPE MODEL

The parabolic equation (PE) model is widely used in modeling radiowave propagation since electrically long distances can easily be handled by employing a marching-type numerical algorithm. The PE is derived from the Helmholtz wave equation by separating the rapidly varying phase term to get a reduced function varying slowly in range for propagating angles close to the paraxial (horizontal) direction. The PE is converted to an initial value problem and can be solved by the Fourier split-step parabolic equation (SSPE), which starts from an initial field defined by an antenna pattern, and marches in range by determining the field along vertical direction at each range step. The SSPE in its standard form is a one-way approach and accounts for only forward-propagating waves. The field at range $x+\Delta x$ is determined as follows [17-19] (assuming $e^{-i\omega t}$ time dependence):

$$\begin{aligned}&u(x+\Delta x,z) = \exp\left[ik(n-1)\Delta x\right]\times\\&F^{-1}\left\{\exp\left[ik\Delta x\left(\sqrt{1-\frac{p^2}{k^2}}-1\right)\right]F\left\{u(x,z)\right\}\right\},\end{aligned}\qquad(8)$$

where F denotes the Fourier Transform, $p = k_z = k\sin\theta$ is the transform wavenumber where θ is the propagation angle from the horizontal, and n is the refractive index. Equation (8) is known as wide-angle SSPE because it is valid for propagation angles up to $40°$-$45°$.

Since the one-way SSPE model considers only forward propagating waves and ignores backward waves, it cannot model multipath effects accurately if there are some obstacles that re-direct the incoming wave. In [18], a two-way SSPE algorithm was proposed to incorporate the backward waves into the solution,

by employing an iterative forward-backward marching algorithm over an irregular terrain. When the wave meets the terrain, it is partially-reflected and is marched out in the opposite direction by reversing the paraxial direction in the PE formulation. This continues until satisfying a stopping criterion that compares the total fields at each iteration. The two-way SSPE algorithm was implemented in MATLAB and named as PETOOL [19].

IV. DIFFRACTING SCREENS MODEL

The diffracting screens model is one of the theoretical models developed by Walfisch and Bertoni [6,7]. In this approach, the rows of city buildings are modeled as a series of absorbing diffracting screens of uniform height. The forward diffraction along the screens, and a final diffraction down to street provides an average field strength at the receiver location (see Fig. 3). This model is polarization independent, and provides a rough estimate about the propagation path loss. In this model, the path loss is obtained by [6,7]:

$$L_{ds} = -L_{fs}-L_1-L_2-18\log\left[\frac{17h_{tx}+d^2}{17h_{tx}}\right],\qquad(9)$$

where h_{tx} is the height of the transmitter antenna in meter, and d is the range in km not beyond horizon. Here, F is the free-space propagation loss given by:

$$L_{fs} = 32.4479+20\log(fd)\,,\qquad(10)$$

where f is the frequency in MHz. The loss L_1 is given as:

$$L_1 = -10\log\left[\frac{G_{rx}(\theta)}{\pi k\sqrt{(h_b-h_{rx})^2+a^2}}\left[\frac{1}{\theta}-\frac{1}{2\pi+\theta}\right]^2\right],\qquad(11)$$

where h_b is the height of the building in meter, h_{rx} is the height of the receiver antenna in meter, a is the distance between the building and the receiver in meter, $G_{rx}(\theta)$ is the gain of the receiver antenna along the corner direction, k is the wavenumber, and $\theta = \tan^{-1}((h_b-h_{rx})/a)$ is the angle from the corner to the receiver. The loss L_2 is obtained as:

$$L_2 = -10\log\left[G_{tx}Q^2\right],\qquad(12)$$

where G_{tx} is the gain of the transmitter antenna along the corner direction (usually taken as unity), and Q is:

$$Q = \begin{cases}\dfrac{w}{d\times 1000-w}\dfrac{1}{\sqrt{2\pi k}\sqrt{(h_b-h_{tx})^2+w^2}}\left[\dfrac{1}{\theta_1}-\dfrac{1}{2\pi+\theta_1}\right] & \text{if } h_{tx}<h_b-0.5\sqrt{\lambda w}\\[3ex]2.35\left[\tan^{-1}\left(\dfrac{h_{tx}}{d\times 1000}\right)\sqrt{\dfrac{w}{\lambda}}\right]^{0.9} & \text{if } h_{tx}>h_b+\sqrt{\lambda w}\end{cases}\qquad(13)$$

where w is the distance between buildings in meter, λ is the wavelength, and $\theta_1 = \tan^{-1}((h_b-h_{tx})/w)$.
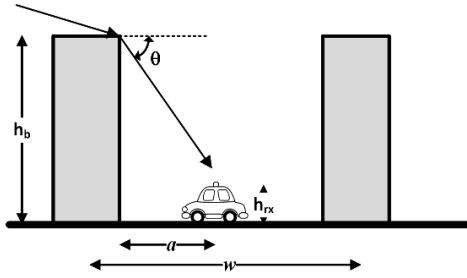
Fig. 3. Illustration of the diffracting screens modeling in the close vicinity of the receiver.

V. NUMERICAL EXAMPLES

This section presents the results of some numerical examples comparing the models in the calculation of path loss. After finding the fields in the SSPE and GO+UTD models, the path loss is obtained by:

$$L = -20\log(u) + 20\log(4\pi)$$
$$+ 10\log(a_e \sin(x/a_e)) - 30\log(\lambda)$$
(14)

where a_e is the *effective* earth radius to account for the bending of the rays in the standard atmosphere.

In Fig. 4, the 3D maps of path loss obtained by the GO+UTD and two-way SSPE are compared assuming that the frequency is 1800 MHz, the polarization is soft (horizontal), the antenna is omnidirectional and the atmosphere is standard. The range and height step sizes are 0.5 m and 0.2 m, respectively, which are used in other simulations as well. There are 7 buildings, the last of which is $d = 900$ m away from the transmitter at $h_{tx} = 20$ m height. The height of each building is $h_b = 15$ m, and the separation between the buildings is $w = 40$ m. The thickness of each building is 10 m. Due to the height of the transmitter, the field between the buildings is mainly due to the diffracted fields and multiple reflections of the diffracted fields. In Fig. 5, 3D maps of path loss and the magnitude of the diffracted field computed by GO+UTD are plotted for different transmitter heights. The frequency is 900 MHz, and the range is $d = 900$ m. As observed from the results, the field strength between the buildings increases as the transmitter height increases. This is expected due to the contribution of reflected fields at the upper part of the buildings. The behavior of the diffracted field in Fig. 5 (c) is because of the non-physical discontinuities around the incident and reflected shadow boundaries. Dominant diffraction occurs along these critical angles.

In Fig. 6, the path loss is plotted as a function of receiver height for different frequencies, assuming that the receiver is $a = 20$ m away from the buildings. In addition, $d = 600$ m and $h_{tx} = 100$ m. Although the GO+UTD and SSPE models compare well, the results of the diffracting screens model deviate. This is expected because the diffracting screens model does not account for the reflections from the finite thickness of the buildings

and the multiple reflections of the diffracted field between the buildings. It is also observed that as the frequency increases, the path loss tends to increase. In Fig. 7, the path loss is plotted as a function of range for different frequencies, assuming that $h_{tx} = 100$ m, $a = 20$ m and $h_{rx} = 1.5$ m. It is seen that as the distance between the buildings and the transmitter antenna increases, the path loss tends to increase. However, due to the interference of diffracted and reflected fields, the path loss may decrease/increase even if the distance increases/decreases. In Fig. 8, the path loss is plotted as a function of receiver height by varying the transmitter height. The frequency is 900 MHz, $d = 900$ m, and $a = 20$ m. As the transmitter height increases, the path loss tends to decrease between the buildings. Finally, in Fig. 9, the GO+UTD and two-way SSPE models are compared for arbitrarily-shaped and positioned buildings. Note that the diffracting screens model is not applicable in this configuration.
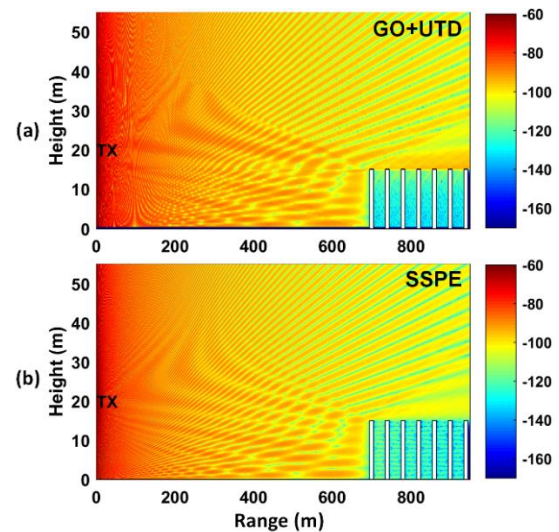
Fig. 4. 3D maps of path loss in 1800 MHz: (a) GO+UTD, and (b) two-way SSPE.

When the computational performances of the models are compared, it is evident that the diffracting screens model quickly performs in a few seconds, but its accuracy is less. Although the SSPE and GO+UTD models involve heavier computational load, they provide accurate results. The computation time of the SSPE and GO+UTD models depend on many factors, such as the distance, the level of discretization in the domain (range and height step sizes), the level of accuracy (the difference in the field distribution when each contributing field is added) and especially the interaction between the radiated fields and the buildings. Depending on the location of the antenna and the buildings, the amount of wave interactions (multiple reflections and diffractions) determine the amount of calculations and the computation

time. The GO+UTD tool has been parallelized in MATLAB by using the parallel processing tools to perform the computations in parallel for each point within the LOS of each source. Hence, the performance of the GO+UTD also depends on the number of processors used. The two-way SSPE performs sequential computations, but this tool will be parallelized in the near future. The 3D maps of the example in Fig. 9 were obtained by GO+UTD in 27mins with 4 processors, and by SSPE in 20mins (12mins) for 1500 (1000) number of step-wise forward-backward calculations. Note that the discretization is taken quite fine (256×380 grid) to obtain better looking maps. The time will decrease if less receiver points are needed in the domain.
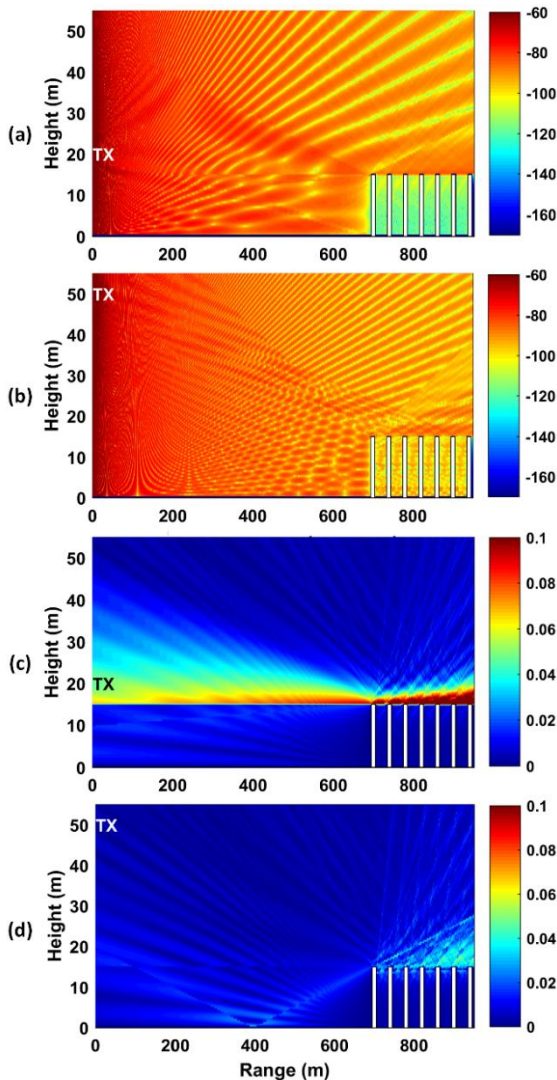
Fig. 5. 3D maps of path loss and the magnitude of the diffracted field computed by GO+UTD in 900 MHz: (a) path loss with $h_{tx} = 20$ m, (b) path loss with $h_{tx} = 50$ m, (c) diffracted field with $h_{tx} = 20$ m, and (d) diffracted field with $h_{tx} = 50$ m.
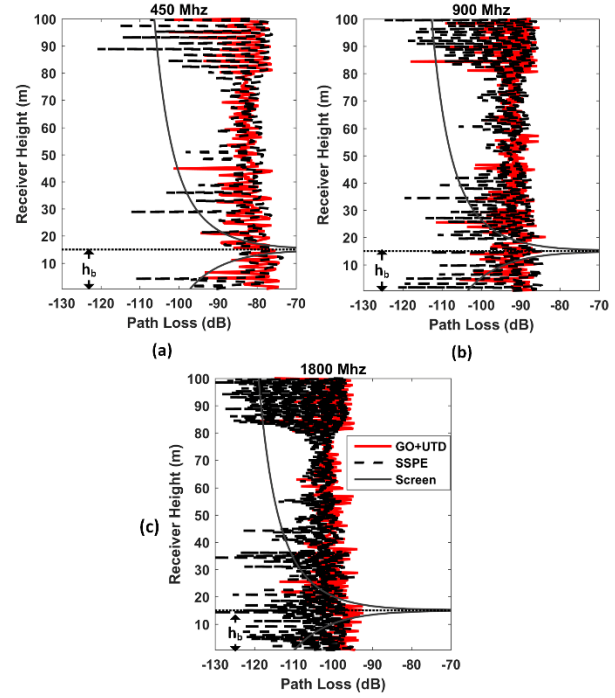
Fig. 6. Path loss as a function of receiver height: (a) 450 MHz, (b) 900 MHz, (c) 1800 MHz. ($d = 600$ m, $h_{tx} = 100$ m, $a = 20$ m).
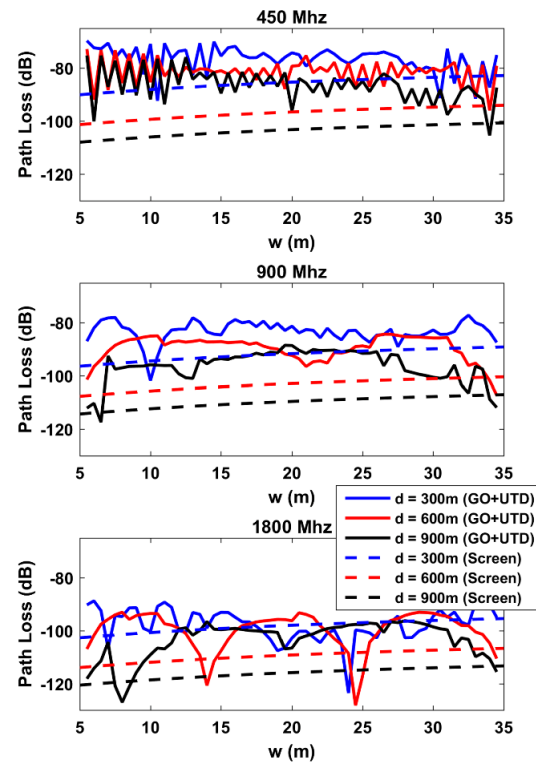
Fig. 7. Path loss as a function of range: (a) 450 MHz, (b) 900 MHz, (c) 1800 MHz. ($h_{tx} = 100$ m, $a = 20$ m, $h_{rx} = 1.5$ m).
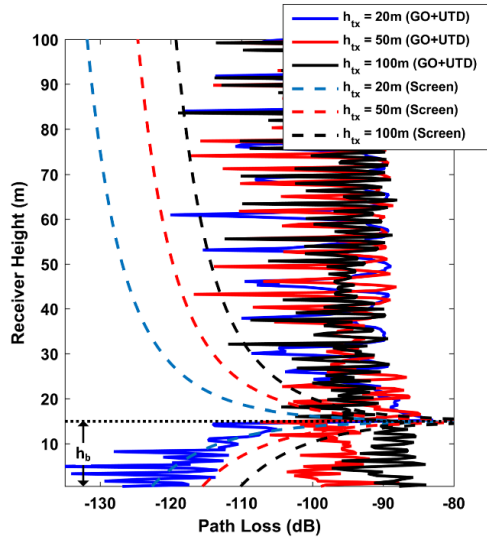
Fig. 8. Path loss as a function of receiver height for different transmitter heights. ($f = 900$ MHz, $d = 900$ m, $a = 20$ m).
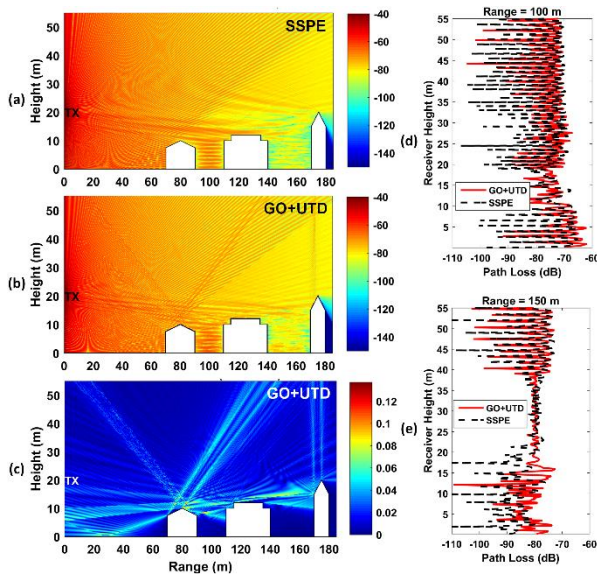
Fig. 9. Simulation of arbitrarily-shaped and -positioned buildings at 900 MHz: (a) path loss (two-way SSPE), (b) path loss (GO+UTD), (c) diffracted field (GO+UTD), (d) path loss vs. receiver height (at 100 m range), and (e) path loss vs. receiver height (at 150 m range).

VI. CONCLUSION

Three models (GO+UTD, two-way SSPE and the diffracting screens models) have been considered for the solution of radiowave propagation in urban area. It is observed that the diffracting screens model provides a rough estimate for the path loss and is not capable of modeling interference effects due to multiple reflections and diffractions. However, the SSPE and GO+UTD

provide accurate results, and the GO+UTD model is useful to visualize the diffracted fields. The GO+UTD and the two-way SSPE compare well in general, except for small differences around the shadow boundaries and in the deep shadow region, which can be improved by decreasing the step size.

REFERENCES

[1] Y. Okumura, E. Ohmori, T. Kawano, and K. Fukua, "Field strength and its variability in UHF and VHF land-mobile radio service," *Rev. Elec. Commun. Lab.*, vol. 16, no. 9, 1968.

[2] M. Hata, "Empirical formula for propagation loss in land mobile radio services," *IEEE Trans. Veh. Technol.*, vol. VT-29, no. 3, pp. 317-325, 1980.

[3] A. G. Longley and P. L. Rice, "Prediction of tropospheric radio transmission loss over irregular terrain—A computer method," *ESSA Technical Report ERL*, 79-IOTS 67, 1968.

[4] K. Bullington, "Radio propagation for vehicular communications," *IEEE Transactions on Vehicular Technology*, vol. VT-26, no. 4, pp. 295-308, 1977.

[5] W. C. Y. Lee, *Mobile Communications Engineering*. McGraw-Hill, New York, 1982.

[6] J. Walfisch and H. L. Bertoni, "A theoretical model of UHF propagation in urban environments," *IEEE Transactions on Antennas and Propagation*, vol. 36, pp. 1788-1796, 1988.

[7] K. Siwiak, *Radiowave Propagation and Antennas for Personal Communications*. Artech House, 2007.

[8] M. Kline and I. Kay, *Electromagnetic Theory and Geometrical Optics*. Wiley, New York, 1965.

[9] J. B. Keller, "Geometrical theory of diffraction," *J. Opt. Soc. Amer.*, vol. 52, pp. 116-30, 1962.

[10] R. G. Kouyoumjian and P. H. Pathak, "A uniform geometrical theory of diffraction for an edge in a perfectly conducting surface," *Proc. IEEE*, vol. 62, pp. 1448-1461, 1974.

[11] A. K. Bhattacharyya, *High Frequency Electromagnetic Techniques Recent Advances and Applications*. Wiley, 1995.

[12] P. Y. Ufimtsev, *Theory of Edge Diffraction in Electromagnetics* Tech Science Press, 2003.

[13] O. Ozgun, "New software tool GO+UTD for visualization of wave propagation," *IEEE Antennas Propag. Mag.*, vol. 58, pp. 91-103, 2016.

[14] O. Ozgun and L. Sevgi, "Numerical techniques in modeling electromagnetic scattering from single and double knife-edge in 2D ground wave propagation problems," *ACES, Appl. Comput. Electrom.*, vol. 27, no. 5, pp. 376-388, 2012.

[15] F. Hacivelioglu, M. A. Uslu, and L. Sevgi, "A MATLAB-based virtual tool for the electromagnetic wave scattering from a perfectly reflecting wedge," *IEEE Antennas Propag. Mag.*, vol. 53, pp. 234-243, 2011.

[16] G. Apaydin and L. Sevgi, "Penetrable wedge scattering problem and a MATLAB-based fringe wave calculator," *IEEE Antennas Propag. Mag.*, vol. 58, pp. 86-93, 2016.

[17] M. F. Levy, *Parabolic Equation Methods for Electromagnetic Wave Propagation*, *IEEE Electromagnetic Wave Series*, London, 2000.

[18] O. Ozgun, "Recursive two-way parabolic equation approach for modeling terrain effects in tropospheric propagation," *IEEE T Antenn. Propag.*, vol. 57, no. 9, pp. 2706-2714, 2009.

[19] O. Ozgun, G. Apaydin, M. Kuzuoglu, and L. Sevgi, "PETOOL: MATLAB-based one-way and two-way split-step parabolic equation tool for radiowave propagation over variable terrain," *Comput. Phys. Commun.*, vol. 182, no. 12, pp. 2638-2654, 2011.

Diffraction at Rounded Wedges: MoM Modeling of PTD Fringe Waves

Gokhan Apaydin [1], Levent Sevgi [2], and Pyotr Ya Ufimtsev [3]

[1] Electromagnetic Consulting, Istanbul, Turkey
g.apaydin@gmail.com

[2] Department of Electrical-Electronics Engineering
Okan University, Tuzla, Istanbul, 34759, Turkey
levent.sevgi@okan.edu.tr

[3] EM Consulting, Los Angeles, California, 90025, USA
pufimtsev@gmail.com

Abstract ─ The paper examines diffraction at rounded wedges with perfectly conducting faces. This topic was a subject of many publications which investigated mainly the *total* diffracted waves. In the present paper, we calculate specifically their *fringe* components to illustrate their sensitivity to the edge curvature. Such fringe waves provide substantial contributions to the scattered field in certain directions and represent a key element in extension of the physical theory of diffraction (PTD) for objects with rounded edges.

Index Terms ─ Fringe wave, hard boundary condition, method of moments, non-uniform currents, physical optics, physical theory of diffraction, rounded wedge, soft boundary condition, uniform currents.

I. INTRODUCTION

A number of papers exist which studied diffraction at wedges with rounded edges. Perhaps the first one was the Kalashnikov paper [1] where he presented the first objective validation of the Sommerfeld diffraction theory. He accomplished thorough experimental investigation of light waves diffracted at metallic wedges with finite edge curvature. In publications [2-24], one can find additional references. Main subjects in those publications were the *total* waves scattered at the edges. Our objective is to calculate specifically their *fringe* components which are the most sensitive to the edge curvature. Such fringe waves provide substantial contributions to the scattered field away from the boundaries of incident and reflected waves. They represent a key element for extension of the physical theory of diffraction (PTD) to objects with rounded edges.

The paper is organized as follows. Section 2 describes the geometry of the problem. In Section 3, we formulate the integral equations in the PTD format for the fringe currents [5,6,25,26]. Section 4 presents their solution by

method of moments (MoM) and illustrates fringe waves scattered at curved edges in comparison with those scattered at sharp wedges.

The time dependence $\exp(-i\omega t)$ is used in the paper.

II. GEOMETRY OF THE PROBLEM

A wedge with a rounded edge is constructed as a combination of the circular cylinder smoothly conjugated with the wedge faces (see, Fig. 1). The wedge with interior angle 2β is located symmetrically along x-axis on the two-dimensional (2D) xy-plane. The origin coincides with the apex of the sharp wedge. Here, a is the radius of the cylindrical surface L_0. Points (x_j, y_j) and $(x_j, -y_j)$ are the junctions/tangency points of the cylindrical surface L_0 with two half-planes L_1, and L_2, which are the faces of the tangential wedge. Fringe waves calculated below for rounded edges are compared with those for the tangential wedge with infinite sharpness (a=0). The wedge is illuminated (from the left) by a plane incident wave propagating along the x-axis. In other words, only double side fixed illumination is considered.

Electromagnetic (EM) waves with two basic polarizations may be investigated for this scenario: the waves with the electric vector (magnetic vector) parallel to the edge of the PEC wedge. In the acoustic diffraction problem, these two situations relate to the wedge with the *soft (hard)* boundary conditions (SBC and HBC), respectively. The solutions of these two-dimensional EM and acoustic problems are identical [5,6].

The wedge structure is canonical in terms of extracting/visualizing every wave phenomenon occurs there [16]. Electromagnetic and acoustic waves interact with objects and scatter. The word *scattering* includes *reflection*, *refraction*, and *diffraction*. The addition of the *scattered field* and the *incident field* yields *total fields*.

The 2D scattering plane around the wedge may be divided into three regions in terms of critical wave

phenomena occurred there [16]. In the first region, all three field components (incident field, reflected field, and diffracted field) exist. In the second (reflection-free) region, only incident and diffracted fields exist. These two regions are separated by the *reflection shadow boundary*.

Fig. 1. Rounded wedge with perfectly reflecting faces.

For the sake of clear understanding and completeness, the definitions of total, scattered, diffracted, and fringe fields are included. *Total field* is the addition of the *incident* and *scattered fields*. In other words, in order to obtain scattered field, one needs to extract/subtract the incident field from the total field. The subtraction of the incident and reflected fields from the total field yields the diffracted field. In other words, the *diffracted field* is equal to the *scattered field* minus the *reflected field*. The f*ringe field* is the part of diffracted field generated by the source-induced fringe (*nonuniform*) currents. These currents exist because of any deviations of a scattering surface from a tangential plane [5,6]. Such deviations can be in the form of sharp discontinuities (edges, tips), discontinuity of a surface curvature (as in the junction points (x_j, y_j), $(x_j, -y_j)$) as well as the smooth bending (as in the cylindrical surface L_0).

As observed in Fig. 2, there are two points that can be taken as the origin. The first is the origin of the *xy*-coordinate system *(0,0)*. For the computation of fields around the wedge for both sharp and rounded wedges the receivers are located on the observation circle with this origin and with a specified radius. In this case, the coordinates (r,φ) related to the sharp wedge are used. The second origin is the center of the rounded-part of the rounded wedge *(d,0)* where we use coordinates (ρ,ψ) related to the rounded wedge. In this case, fields around the rounded wedge are computed for the receivers located on the observation circle with this origin and with a specified radius. Figure 2 presents these two

cases. Note that, reflections occur only in the shaded area for the sharp wedge but occur everywhere for the rounded wedge.

Fig. 2. Scenarios for: (a) sharp–rounded wedge comparisons, and (b) fields simulated around the rounded wedge.

III. FORMULATION OF INTEGRAL EQUATIONS

In the problem under investigation, we apply a scalar interpretation for a perfectly conducting wedge. The soft boundary condition $u=0$ relates to excitation of the wedge by the *E*-polarized plane wave:

$$u^{inc} = E_z^{inc} = u_0 e^{ikx}. \tag{1}$$

The hard boundary condition ($\partial u / \partial n = 0$) corresponds to the case when the wedge is illuminated by the *H*-polarized plane wave:

$$u^{inc} = H_z^{inc} = u_0 e^{ikx}. \tag{2}$$

Proceeding with the second Green's identity one can obtain the surface integral equation:

$$u^{inc}(x, y) + \frac{i}{4} p.v. \int_L \left[u(x', y') \frac{\partial}{\partial n} H_0^{(1)}(kr) - \frac{\partial u(x', y')}{\partial n} H_0^{(1)}(kr) \right] dl' = \frac{u(x, y)}{2}. \tag{3}$$

Here, $L=L_0+L_1+L_2$ is the total surface of the body, $r = \sqrt{(x - x')^2 + (y - y')^2}$, and the integrand is singular at the point $r=0$. The integral is understood as its Cauchy principal value. The incident wave u^{inc} in (3) is given everywhere on the surface L. Function u is the total field $u = u^{inc} + u^{sc}$. It follows from (3) that,

$$u^{inc}(x, y) - \frac{i}{4} p.v. \int_L \frac{\partial u_s(x', y')}{\partial n} H_0^{(1)}(kr) dl' = 0, \tag{4}$$

for the soft surface ($u=0$), and,

$$u^{inc}(x, y) + \frac{i}{4} p.v. \int_L u_h(x', y') \frac{\partial}{\partial n} H_0^{(1)}(kr) dl' = \frac{u(x, y)}{2}, \tag{5}$$

for the hard surface ($\partial u / \partial n = 0$).

Now, we recast these equations in the PTD format [5,6]. First, introduce the surface currents:

$$j_s = \frac{\partial u_s}{\partial n}, j_h = u_h. \tag{6}$$

They consist of two components:

$$j_{s,h} = j_{s,h}^{(0)} + j_{s,h}^{(1)} = j_{s,h}^{PO} + j_{s,h}^{fr}, \qquad (7)$$

where $j^{(0)} = j^{PO}$ is the uniform component defined according to the physical optics (PO). It is defined as:

$$j_s^{PO}(x',y') = 2\frac{\partial u^{inc}}{\partial n}, j_h^{PO}(x',y') = 2u^{inc}. \qquad (8)$$

The term $j_{s,h}^{fr}$ represents the non-uniform PTD component called here the fringe current. In view of these notations, Equations (4) and (5) take the forms:

$$\frac{i}{4} p.v. \int_L j_s^{fr}(x',y') H_0^{(1)}(kr) dl' = \\ u^{inc}(x,y) - \frac{i}{4} p.v. \int_L j_s^{PO}(x',y') H_0^{(1)}(kr) dl' \qquad (9)$$

$$\frac{1}{2} j_h^{fr}(x,y) - \frac{i}{4} p.v. \int_L j_h^{fr}(x',y') \frac{\partial}{\partial n} H_0^{(1)}(kr) dl' = \\ \frac{i}{4} p.v. \int_L j_h^{PO}(x',y') \frac{\partial}{\partial n} H_0^{(1)}(kr) dl' \qquad (10)$$

Calculating $j_{s,h}^{fr}$ from (9) and (10), one can find the total fringe waves scattered by the object as:

$$u_s^{fr}(x,y) = -\frac{i}{4} \int_L j_s^{fr}(x',y') H_0^{(1)}(kr) dl', \qquad (11)$$

$$u_h^{fr}(x,y) = \frac{i}{4} \int_L j_h^{fr}(x',y') \frac{\partial}{\partial n} H_0^{(1)}(kr) dl'. \qquad (12)$$

As shown in [6,25], the integrals from $j_{s,h}^{PO}$ over the faces $L_{1,2}$ represent the PO fields scattered by half-planes. They are described in accordance with (3.37-3.40) and (3.49), (3.50) of [6]. The details of their calculations are presented in [25] that contain the fringe integral equations similar to (9), (10). The only difference in (9), (10) consists in presence of integrals over the cylindrical part L_0.

For numeric solution of the fringe integral Equations (9), (10) we apply the classical MoM (see, [14,20] for details).

IV. NUMERICAL SIMULATIONS AROUND SHARP AND ROUNDED WEDGES

The MoM related references mentioned above in the Introduction show that MoM is highly capable of solving surface integral equations. Here, we develop the MoM algorithms for the fringe integral equations derived in the previous section and first test them against the sharp wedge. Note that, in addition to the fringe fields, the total, scattered, and PO scattered field variations around the wedge are also given for clear understanding of wave scattering phenomena (see, [16,18] for detailed illustrations of diffracted fields). Fringe fields are directly computed using (11), (12). One needs to add PO scattered fields in order to obtain total scattered fields. Finally, addition of the incident field to the scattered field yields the total field.

Numerical simulations in this section consist of two parts. As shown in Fig. 2 (a), the first computations belong to various fields from the rounded wedge and their comparison with that from the sharp wedge. The frequency of all simulations is 30 MHz (i.e., λ=10 m). The observer radius is r=2λ. Although infinite, the length of L_1 and L_2 parts of the wedge is taken 50λ-long, which is tested to be enough for the accuracies used in these numerical calculations. Also, the number of segments in one wavelength is chosen as 20 for MoM calculations (in the vicinity of the edge up to 100-500 segments may be used to increase the accuracy). It is also numerically tested that the number of segments of the rounded part (L_0 part) is at least 20 to satisfy rounded curvature. Note that, different discretizations may be required for the wedges with soft and hard BCs [20]. Approximately, 10λ-20λ-long wedge sides are enough for the soft wedge but up to 100λ-long wedge sides (even more) may be required for the hard wedge.

In the second part, fields from the rounded wedge are computed for the scenario in Fig. 2 (b). It includes the fringe field, the PO field, and their sum.

For the soft sharp wedge, we denote $j_s^{fr}(x,y)$ as $j_s^{fr,shrp}(x,y)$ and outside the wedge it creates the field:

$$u_s^{fr,shrp}(x,y) = -\frac{i}{4} \int_L j_s^{fr,shrp}(x',y') H_0^{(1)}(kr) dl'. \quad (13)$$

This fringe field is calculated using (4.18) on p. 107 in [6]. This is assumed as the reference (PTD) solution. Alternatively, the MoM algorithm presented in [20,25] can be used directly. For the rounded wedge, (9) is discretized and solved using the new MoM algorithm and segment fringe currents $j_s^{fr,rnd}$ are obtained. Then, fringe fields $u_s^{fr,rnd}(x,y)$ around the object are calculated using (11).

In the following examples, for the sharp wedge, first the wedge (half) angle β=5°,15°,30°,45° is specified. Then, the observation circle with r=2λ is chosen. On this circle, the receivers are located at grid points $x = r\cos(\beta+\varphi)$, $y = r\sin(\beta+\varphi)$ with $\Delta\varphi$=0.5°. Finally, because of the symmetry with respect to x axis, $\left| u_s^{fr,shrp}/u_0 \right|$ for $0 \le \varphi \le \pi-\beta$ is calculated and plotted. For the rounded wedge, and for the same sets of parameters, $a=\lambda/m$, m=2,5,10,20,… is specified and MoM solutions are generated and $\left| u_s^{fr,rnd}/u_0 \right|$ for $0 \le \varphi \le \pi-\beta$ is plotted. The objective is to demonstrate how $\left| u_s^{fr,rnd}/u_0 \right|$ approaches $\left| u_s^{fr,shrp}/u_0 \right|$ with decreasing of the rounding radius (a). Examples presented in Figs. 3-7 belong to SBC case; the next figures are given both for SBC and HBC cases.

Note that, the rounded wedge MoM model directly yields sharp wedge solutions when $a=0$. This is used in validating the new rounded wedge MoM algorithm. The rounded wedge algorithm is tested against both PTD and previous sharp MoM models and perfect agreement is obtained. Figure 3 belongs to these validations (a free MATLAB package has been prepared for the visualization of fringe waves around a sharp wedge and its tutorial has just been published [26]).

Figures 4-5 present total and fringe fields, respectively, with four different wedges for the scenario in Fig. 2 (a). The three curves belong to $a=0$, $a=\lambda/10$, and $a=\lambda/5$, cases. As observed in Fig. 4, major total field contribution comes from the interaction of incident, reflected, and diffracted waves. Total fields of the 90° wedge for all three cases are almost identical. The differences in the total fields around the wedge become significant as the wedge interior angle gets smaller. This is because the locations of the receivers shift significantly for narrow wedges (see, Fig. 2 (a)). The same observation also holds for the fringe field variations in Fig. 5.

For the sharp wedge only diffracted field occurs backwards (i.e., towards to the angle of incoming plane wave). But for the rounded wedge there is a strong backward reflection.

Note that, as a increases, the distance between the receiver on x-axis and backward specular reflection point increases and the amplitude of the scattered field along this direction decreases. The effect of this is observed in Fig. 5 where fringe field variation is plotted. However, for fringe waves another reason also exists for their decrease. The larger is radius a of rounded/cylindrical surface L_0 the smaller gets its curvature and, as a consequence, the smaller fringe currents become there.

PO and fringe fields around the rounded wedge are simulated in this section. The scenario for these simulations is given in Fig. 2 (b). For the calculation of this fringe field, first, β and a are chosen. Then, the receivers are located on the circle around the rounded wedge using the grid points (x,y) on the circle $\rho=a+n\lambda$, $n=1,2,\dots$ with $0 \leq \psi \leq \psi_m$ and $\Delta\psi=0.5°$ where,

$$\sin(\beta+\psi_m) = \frac{a}{\rho}. \tag{14}$$

Then, (9) is discretized and solved using the new MoM algorithm and the segment fringe currents $j_s^{fr,rnd}$ are obtained. Fringe fields $u_s^{fr,rnd}(x,y)$ are then calculated using (11). Fringe fields vs. angle variations are then plotted.
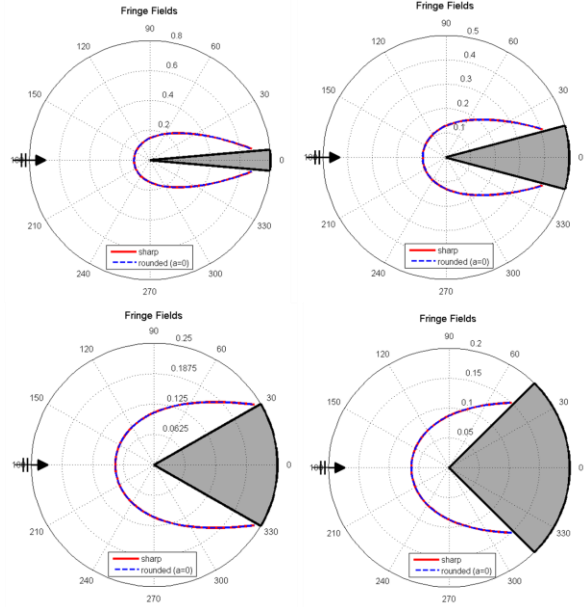

Fig. 3. Fringe fields around different SBC sharp wedges (for the scenario in Fig. 2 (a)). The solid (red) curve is calculated according to (4.18) in [6]. The dashed (blue) curve – by MoM.
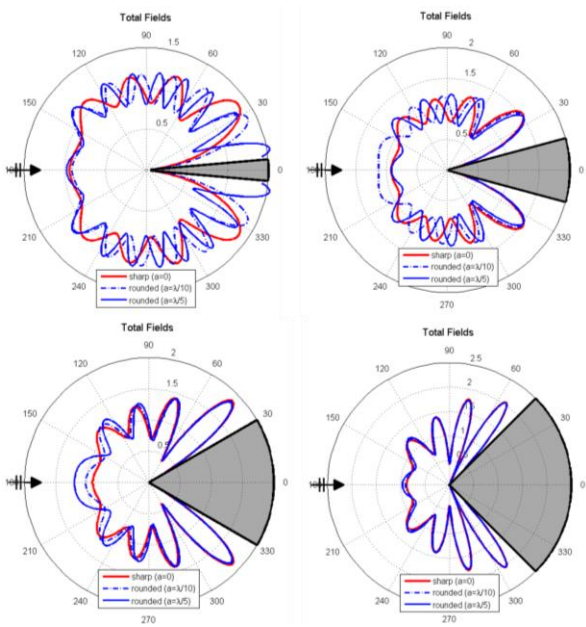

Fig. 4. Total fields around different SBC wedges (for the scenario in Fig. 2 (a)). The solid (red) curve is calculated according to (4.18) in [6]. Other curves – by MoM.
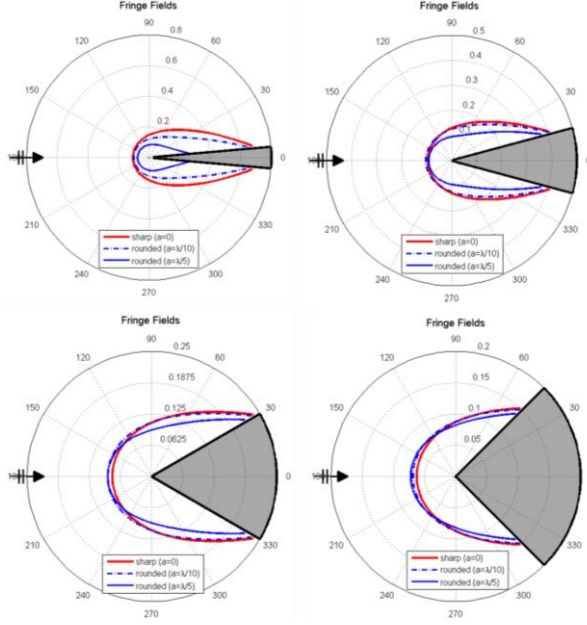
Fig. 5. Fringe fields around different SBC wedges (for the scenario in Fig. 2 (a)).
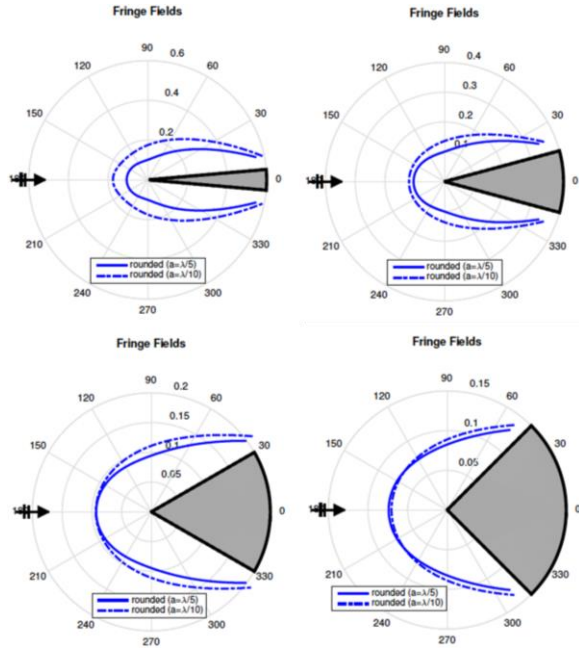

Fig. 6. Fringe fields around different SBC wedges (for the scenario in Fig. 2 (b)).

For the PO-scattered fields around the rounded wedge, we calculate the integral:

$$u_s^{PO,rnd}(x,y) = -\frac{i}{4}\int_L j_s^{PO}(x',y')H_0^{(1)}(kr)dl', \quad (15)$$

with $L = L_0 + L_1 + L_2$. Hence,

$$u_s^{PO,rnd}(x,y) = u_{s,L_0}^{PO,rnd} + u_{s,L_1}^{PO,rnd} + u_{s,L_2}^{PO,rnd}. \quad (16)$$

Here,

$$u_{s,L_0}^{PO,rnd}(x,y) = -u_0 e^{ikd}\frac{ka}{2}$$
$$\times \int_{-\psi_j}^{\psi_j} \cos\psi\, e^{-ika\cos\psi} H_0^{(1)}(kr_0)d\psi, \quad (17)$$

with $r_0 = \sqrt{(x-x_0)^2 + (y-y_0)^2}$,

$$u_{s,L_1}^{PO,rnd}(x,y) = u_0 e^{ikx_j} v_s^{(0)}(kr_1,\phi_1,\phi_0)$$
$$+ \begin{cases} -u_0 e^{ikx_j} e^{-ikr_1\cos(\phi_1+\phi_0)} & \text{for } 0 \le \phi_1 \le \beta \\ 0 & \text{for } \beta \le \phi_1 \end{cases}, \quad (18)$$

$$u_{s,L_2}^{PO,rnd}(x,y) = u_0 e^{ikx_j} v_s^{(0)}(kr_2,\phi_2,\phi_0), \quad (19)$$

for $\pi - \beta \le \phi_2 \le 2\pi - 2\beta$, where $\phi_{1,2}$ is found from (A.4). Also,

$$\begin{aligned} r_1 &= \sqrt{(x-x_j)^2 + (y-y_j)^2} \\ r_2 &= \sqrt{(x-x_j)^2 + (y+y_j)^2} \\ x_j &= d - a\cos\psi_j = d - a\sin\beta \\ y_j &= a\sin\psi_j = a\cos\beta \end{aligned} \quad (20)$$

Notice that, $v_s^{(0)}(kr_1,\phi_1,\phi_0)$ is discontinuous on the boundary of the reflected plane wave ($\phi_1 = \beta$). In summary, $u_s^{PO,rnd}$ is calculated from (15) and (16) for the specified grid points and the results are plotted as PO fields vs. angle. The total field will then be the sum of these two:

$$u_s^{tot,rnd}(x,y) = u_s^{fr,rnd}(x,y) + u_s^{PO,rnd}(x,y). \quad (21)$$

Figure 6 belongs to the second scenario given in Fig. 2 (b) and shows fringe field distributions for four different wedge angles for two different a values ($a_1 = \lambda/10$ and $a_2 = \lambda/5$). Here, the receivers are located on a circle around the rounded wedge (not around the origin on the xy-plane) with the center at $(0,x_2)$ where $x_2 = d_2 = a_2/\sin\beta$ and radius $\rho_2 = \lambda/5 + 2\lambda$. Although, the receivers for the computations for $a_1 = \lambda/10$ and $a_2 = \lambda/5$ are exactly at the same points, the difference of distances between the rounded face and the receivers for these two cases gets larger, for the receivers around the backscattering direction $\varphi = 180°$.

Figure 7 shows uniform (PO), nonuniform (fringe), and total currents on the surface of the wedge having a 30° interior angle, and $a = \lambda/2$ for the SBC case. This figure clearly demonstrates that the fringe currents concentrate in vicinity of the junction points, i.e., in vicinity of the surface curvature discontinuities. Tests with different sets of parameters show that the strongest fringe currents occur for the sharp wedge ($a = 0$). The fringe current decays on both sides of the junction points and has a minimum at midpoint between the junctions.

Figure 8 compares fringe currents of both SBC and HBC cases a few λ around junction points. Here, although $L_1=L_2=50\lambda$ is used in the MoM computations, only $L_1=L_2=4.35\lambda$ and $L_0=1.3\lambda$ sections are shown in the figure (i.e., horizontal axis extends from -5λ to 5λ) with $\lambda/40$ discretization. Nearly, 500 segments are used for the rounded part L_0 (with $a=\lambda/2$, this corresponds to a nearly $\lambda/400$ segmentation). Very small segments are used just to increase the accuracy around the junctions.

As seen there, the fringe current distributions of SBC and HBC cases look alike; they have maxima on the junction points. However, SBC fringe currents make sharp peaks on the junction points but HBC fringe currents have slight discontinuities. Also, HBC fringe currents are higher than SBC fringe currents. Finally, both fringe currents decay away from junctions but HBC fringe currents' decay rate is lower than SBC fringe currents.

Here, it is pertinent to remind the fringe currents behavior in vicinity of a sharp wedge. In SBC case, the fringe current tends to infinity as $(1/kr)^{1-\pi/\alpha} \to \infty$, while in HBC case it is finite ($j_h^{fr} = u_0(4\beta - 2\pi)/\alpha$) when $r \to 0$ and $\alpha = 2\pi - 2\beta > \pi$ [6,27]. Because j_h^{fr} is finite for sharp wedges it is not surprising that it has only slight changes in vicinity of the junction points where the surface L is smooth and only its second derivative undergoes discontinuities.

Remind also that, away from the edge ($kr \gg 1$) on the sharp wedge (with $\beta=15°$) the SBC current j_s^{fr} drops as $(1/kr)^{3/2}$ while the HBC current j_h^{fr} attenuates as $(1/kr)^{1/2}$ [6]. The curves in Fig. 8 for $|r| > 3\lambda$ relate to large values ($kr > 18$) and qualitatively agree with those for a sharp wedge. Notice as well that at point $\psi=0$ ($r=0$ in Fig. 8) on the circular cylinder alone (without L_1, L_2), the SBC and HBC fringe currents are determined by (14.53) and (14.54) of [6] where one should set $\gamma = \pi/2$ and $\psi = -\pi/2$. According to these equations, $\left|j_s^{fr}\right| = k\left|j_h^{fr}\right|$. For $\lambda=10$m (with $f=30$ MHz) taken in our calculations this relationship means that $\left|j_s^{fr}\right| \approx 0.6\left|j_h^{fr}\right|$, while for the rounded wedge according to Fig. 8 we have $\left|j_s^{fr}\right| \approx 0.7\left|j_h^{fr}\right|$.

Finally, in Fig. 9 for comparison purpose we plot both the soft and hard fringe waves for rounded wedges with $a=a_2=\lambda/5$ at the distance $\rho=a_2+2\lambda$. They relate to the scenario in Fig. 2 (b). Notice that, the curves for the wedge with $\beta=30°$ are similar to those for the sharp wedge given in Fig. A4.5 of [6].
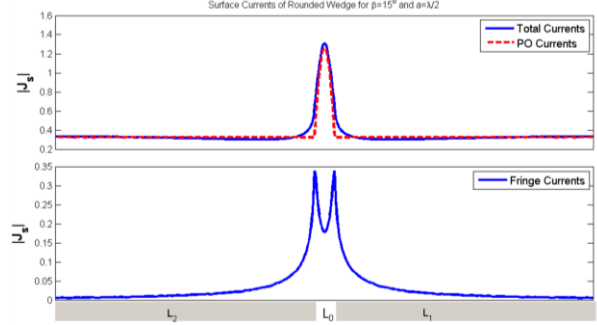

Fig. 7. Total, PO and PTD (fringe) surface currents of the 30° SBC wedge.
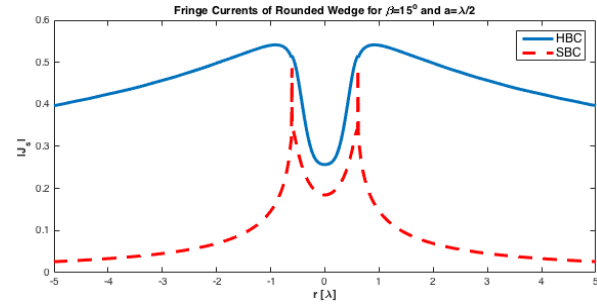

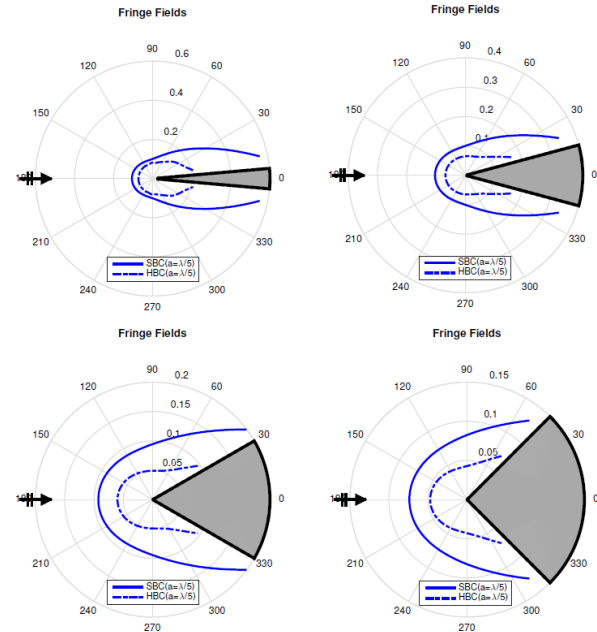Fig. 8. PTD (fringe) surface currents of the 30° SBC and HBC wedges.

Fig. 9. Fringe fields around different SBC/HBC wedges (for the scenario in Fig. 2 (b)).

V. CONCLUSIONS

Fringe integral equations suitable for analysis of the field scattered by rounded soft and hard wedges are developed. Numeric results are obtained via a regular MoM procedure. Comparison with scattering from sharp wedges is illustrated and confirms that the rounded wedge can be considered, approximately, as the sharp wedge when the radius of rounding does not exceed one tenth of the wavelength. The results are also important from the theoretical/methodical point of view because they demonstrate the direct extension of PTD for objects with rounded edges.

REFERENCES

[1] A. Kalashnikov, "The Gouy-Sommerfeld diffract-tion," (in Russian) *J. Russian Physical-Chem. Soc.*, vol. 44, Physical Section, St. Petersburg, Russia, no. 3, pp. 137-144, 1912.

[2] C. Hansen, Ed., *Geometrical Theory of Diffraction*. IEEE Press, 1981.

[3] J. J. Bowman, T. B. A. Senior, and P. L. E. Uslenghi, Eds., *Electromagnetic and Acoustic Scattering by Simple Shapes*. Hemisphere Publishing Corporation, 1987.

[4] Y. A. Kravtsov and N. Y. Zhu, *Theory of Diffraction: Heuristic Approaches*. Alpha Science Series on Wave Phenomena, 2010.

[5] P. Y. Ufimtsev, *Fundamentals of the Physical Theory of Diffraction.* John Wiley & Sons, Inc., Hoboken, New Jersey, USA, 2007.

[6] P. Y. Ufimtsev, *Fundamentals of the Physical Theory of Diffraction*. Second Edition, John Wiley & Sons, Inc., Hoboken, New Jersey, USA, 2014.

[7] M. A. K. Hamid, "Diffraction coefficient of a conducting wedge loaded with a cylindrical dielectric slab at the apex," *IEEE Trans. Antennas Propagat.*, vol. AP-21, pp. 398-399, May 1973.

[8] A. Elsherbeni and M. Hamid, "Diffraction by a wide double wedge with rounded edges," *IEEE Trans. Antennas Propagat.*, vol. AP-33, pp. 1012-1015, Sep. 1985.

[9] W. Hallidy, "On uniform asymptotic Green's function for the perfectly conducting cylinder tipped wedge," *IEEE Trans. Antennas Propagat.*, vol. AP-33, no. 9, pp. 1020-1025, Sep. 1985.

[10] K. M. Mitzner, K. J. Kaplin, and J. F. Cashen, "How scattering increases as an edge is blunted," In the book: H. N. Kriticos and D. L. Jaggard (Editors), *Recent Advances in Electromagnetic Theory*. Springer, 1990.

[11] E. N. Vasiliev, V. V. Solodukhov, and A. I. Fedorenko, "The integral equation method in the problem of electromagnetic waves diffraction by complex bodies," *Electromagnetics*, vol. 11, no. 2, pp. 161-182, Oct. 2007.

[12] I. G. Yarmakhov, "Investigation of diffraction of electromagnetic waves at edges of perfectly conducting and impedance wedges with a rounded edge," (in Russian - *Radiotekhnika I Elektronika,* vol. 36, no. 10, pp. 1887-1895, 1991) *J. Commun. Technol. Electron.*, vol. 49, no. 4, pp. 379, 2004.

[13] M. A. Christou, A. C. Polycarpou, and N. C. Papanicolau, "Soft polarization diffraction coefficient for a conducting cylinder-tipped wedge," *IEEE Trans. Antennas Propagat.*, vol. AP-58, no. 12, pp. 4082-4085, Dec. 2010.

[14] C. A. Balanis, L. Sevgi, and P. Y. Ufimtsev, "Fifty years of high frequency diffraction," *Int. Journal RF Microwave Computer-Aided Eng.*, vol. 23, no 4, pp. 394-402, July 2013.

[15] P. Y. Ufimtsev, "The 50-year anniversary of the PTD: Comments on the PTD's origination and development," *IEEE Antennas Propagat. Mag.*, vol. 55, no. 3, pp. 18-28, June 2013.

[16] F. Hacivelioglu, L. Sevgi, and P. Y. Ufimtsev, "Electromagnetic wave scattering from a wedge with perfectly reflecting boundaries: Analysis of asymptotic techniques," *IEEE Antennas Propagat. Mag.*, vol. 53, pp. 232-253, June 2011.

[17] G. Cakir, L. Sevgi, and P. Y. Ufimtsev, "FDTD modeling of electromagnetic wave scattering from a wedge with perfectly reflecting boundaries: Comparisons against analytical models and calib-ration," *IEEE Trans. Antennas Propagat.*, vol. AP-60, no. 7, pp. 3336-3342, July 2012.

[18] F. Hacivelioglu, M. A. Uslu, and L. Sevgi, "A Matlab-based simulator for the electromagnetic wave scattering from a wedge with perfectly reflecting boundaries," *IEEE Antennas Propagat. Mag.*, vol. 53, no. 6, pp. 234-243, Dec. 2011.

[19] M. A. Uslu and L. Sevgi, "Matlab-based virtual wedge scattering tool for the comparison of high frequency asymptotics and fdtd method," *Appl. Comput. Electromagn. Soc. J.*, vol. 27, no. 9, pp. 697-705, Sep. 2012.

[20] G. Apaydin and L. Sevgi, "A novel wedge diffraction modeling using method of moments (mom)," *Appl. Comput. Electromagn. Soc. J.*, vol. 30, no. 10, pp. 1053-1058, Oct. 2015.

[21] M. A. Uslu, G. Apaydin, and L. Sevgi, "Double tip diffraction modeling: finite difference time domain vs. method of moments," *IEEE Trans. Antennas Propagat.*, vol. AP-62, no. 12, pp. 6337-6343, Dec. 2014.

[22] F. Hacivelioglu, L. Sevgi, and P. Y. Ufimtsev, "Wedge diffracted waves excited by a line source: exact and asymptotic forms of fringe waves," *IEEE Trans. Antennas Propagat.*, vol. AP-61, no. 9, pp. 4705-4712, Sep. 2013.

[23] A. K. Bhattacharyya, "Scattering by a right-angled penetrable wedge: A stable hybrid solution (tm case)," *Appl. Comput. Electromagn. Soc. J.*, vol. 5,

no. 3, 1990.

[24] T. Ikiz and M. K. Zateroglu, "Diffraction of obliquely incident plane waves by an impedance wedge with surface impedances being equal to the intrinsic impedance of the medium," *Appl. Comput. Electromagn. Soc. J.*, vol. 26, no. 3, pp. 199-205, Mar. 2011.

[25] G. Apaydin, L. Sevgi, and P. Y. Ufimtsev, "Fringe integral equations for the 2-D wedge with soft and hard boundaries," *Radio Science*, vol. 61, no. 9, pp. 4705-4712, Sep. 2016.

[26] G. Apaydin and L. Sevgi, "Two dimensional non-penetrable wedge scattering problem and a Matlab-based fringe wave calculator," *IEEE Antennas Propagat. Mag.*, vol. 58, no. 2, pp. 86-93, Apr. 2016.

[27] P. Y. Ufimtsev, "Fast convergent integrals for nonuniform currents on wedge faces," *Electromagnetics*, vol. 18, no. 3, pp. 289-313, May-June 1998. Corrections in *Electromagnetics*, vol. 19, no. 5, pp. 473, 1999.

Gökhan Apaydin received the Ph.D. degree from Bogazici University, Istanbul in 2007. He was with Bogazici University from 2001 to 2005; the University of Technology Zurich from 2005 to 2010; Zirve University, Gaziantep from 2010 to 2016; and he was a Visiting Associate Professor at the Department of ECE, University of Illinois at Urbana–Champaign, IL, USA, in 2015. He has been involved with complex electromagnetic problems and systems. His research interests include analytical and numerical methods (FEM, MoM, FDTD) in electromagnetics (especially on electromagnetic computation of wave propagation, diffraction modeling, and related areas).

Levent Sevgi received the Ph.D. degree from Istanbul Technical University (ITU), and Polytechnic Institute of New York University, Brooklyn, in 1990. Prof. Leo Felsen was his Advisor. He was with ITU (1991-1998); the Scientific and Technological Council of Turkey–Marmara Research Institute, Gebze/Kocaeli (1999-2000); Weber Research Institute/Polytechnic University in New York (1988-1990); the Scientific Research Group of Raytheon Systems, Canada (1998-1999); the Center for Defense Studies, ITUVSAM (1993-1998) and (2000-2002); the Department of ECE, UMASS Lowell, MA (2012-2013) for his sabbatical term; and Doğuş University (2001-2014). Since 2014, he has been with Okan University, Istanbul. He has been involved with complex electromagnetic problems and systems for ~ 30 years.

Pyotr Ya. Ufimtsev received the Ph.D. degree in Radio Engineering from the Central Research Radio Engineering Institute of the Defense Ministry, Moscow in 1959, and the Dr.Sc. degree in Theoretical and Mathematical Physics from St. Petersburg University in 1970. He was with the Institute of Radio Engineering and Electronics of the Academy of Sciences, Moscow; the Moscow Aviation Institute; Northrop-Grumman Corp., CA; the University of California at Los Angeles, and the University of California at Irvine. Among his fundamental results are the theory of scattering from black objects, the physical theory of diffraction, and the discovery of new physical phenomena related to surface waves in absorbing materials.

A Diffraction Ray Tracing Method Based on Curved Surface Ray Tube for Complex Environment

Dan Shi, Na Lv, and Yougang Gao

School of Electronic Engineering
Beijing University of Posts and Communications, Beijing, 100876, China
shidan@buptemc.com

Abstract ─ A self-adaptive ray tracing method for predicting radio propagation based on the curved surface ray tube (CSRT) model is proposed in this paper. The CSRT model is implemented in the ray tracing method to reduce the unnecessary consume compared with the four-ray tube model in complex environments. Both the theoretical calculation and the practical simulation were applied to verify the high efficiency of the CSRT model. The radio wave propagation in a complex scene was calculated by the CSRT model and the four-ray tube model, and the theoretical analytical result demonstrated that the CSRT model achieved a speed up of 4 times compared to the four-ray tube model. Moreover, the wave propagations in several different environments were simulated with our developed software based on the CSRT and four-ray tube tracing method, and the comparisons of the simulation time spent by the two methods proved the high efficiency of the CSRT model. In addition, the correct prediction of the propagation paths and E-field also validates the accuracy of the CSRT model.

Index Terms ─ CSRT model, four-ray tube, radio wave propagation, ray tracing.

I. INTRODUCTION

In recent years, wave propagation prediction in the electrically large environment has been studied in an extensive published literature. A considerable interest has been shown in the ray tracing algorithm researches combined with the uniform theory of diffraction (UTD) [1-6]. Compared with the high accuracy but time-consuming reverse algorithm, the time-saving shooting and bouncing ray (SBR) method [7-12] has attracted attentions widely.

A ray tracing method based on the geometrical optics (GO) theory was presented to predict reflection and refraction rays [13-15]. A center-ray tube model was used in [14], which set one ray as the center of a ray cone and predicted the propagation of electromagnetic waves by only tracing the center ray of the tube. Since the wavefront of a center-ray tube is a circle or an ellipse, it overlaps with another wavefront when it is used to cover the spherical surface. Moreover, the radius of the receiving ball also determines the accuracy, and this model may produce abundant repeated paths. The lateral-ray tube model used in [5-8,14] is a good solution to the overlapping problem. The icosahedron model [7,8] and point source launching four-ray tube model [5,6,14] can cover the spherical wavefront seamlessly and without overlapping. Since the models mentioned before cannot be applied to trace diffraction rays, a segment source launching four-ray tube model combined with the UTD was proposed in [5,6]. This model solved the difficulties of the point source launching ray tube in tracing diffraction paths, and the cylindrical wavefront can be covered seamlessly and without overlap. Nevertheless, the segment source launching four-ray tube model cannot deal with complex crossing situations with the terrain and may produce much extra expending. Thus, a triangular wavefront ray tube model has been mentioned in the paper [16], but there are not detailed descriptions about the features and its application in tracing processing.

On this basis, a three-ray curve surface ray tube (CSRT) model is presented in this paper, and the tracing process is introduced in detail using this model. The CSRT model can be applied to predict the propagation of the diffraction rays. Compared with the segment source launching four-ray tube model (hereinafter referred as four-ray tube model), the CSRT model can deal with more general situations accurately with less consumptions. Thus, the CSRT model can provide accurate prediction outcomes with high efficiency in more general environments.

Section II gives a detailed definition of the three-ray CSRT model, and proves the efficiency improvement of the CSRT model in theory compared with the four-ray tube model. In Section III, different intersection situations with the terrain triangle facets by using the CSRT are listed. The description of how the tracing method runs is described in Section IV. Section V shows several simulation results of different terrains, and discusses the results compared between the three-ray CSRT model and the four-ray tube model tracing method. In Section VI, a

conclusion is drawn.

II. COMPARISONS BETWEEN THE FOUR-RAY TUBE MODEL AND THE THREE-RAY CSRT MODEL

The four-ray tubes launched by edges are shown in Fig. 1 (a). Every two adjacent rays of the four-ray tubes determining a ray tube are in the same plane, which meets the characteristic of the conventional lateral-ray tube. The four-ray tube model is suitable to calculate the wave propagation in the simple city environments. The buildings in city models are usually assumed to be cubes (Fig. 1 (b)), and if the four-ray tube model partly crosses with a building, the wavefront of the tube ABCD will be divided into two quadrilaterals. However, only the wavefront BCFE can produce a reflection ray tube. Since the edges of two buildings are parallel, the rays IE and JF are in the same plane. So, rays IE, IB, JC and JF can form a new four-ray tube for reflection.

(a)   (b)
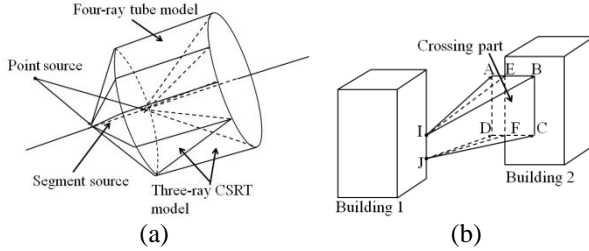
Fig. 1. (a) The four-ray tubes and three-ray CSRTs launching model. (b) The four-ray tube model in the city environment.

However, for the complex environment, the terrain is often represented as closely spaced triangular surface. The situations of the ray tube crossing with a terrain become more complex. In Fig. 2, the wavefront of the four-ray tube launched from the diffraction edge is divided into two parts. Nevertheless, the intersecting part of the wavefront cannot produce one or several four-ray tubes. Thus, the popular solution is to assume the whole tube will reflect from the plane of the terrain triangular. The part to complete the four-ray tube wavefront does not produce real rays, so rays in this part belong to the unnecessary redundancy. When the reflection ray tube crosses with the terrain again, the intersecting situations become more complex, and the consumptions increase significantly. Many paths which do not exist will be counted in the result.

In Fig. 2, the edge AB is the mirror edge of the diffraction edge of the terrain triangle, and the point O is the crossing point of line AC and line BE, which is regarded as the virtual launching point of this four-ray tube.
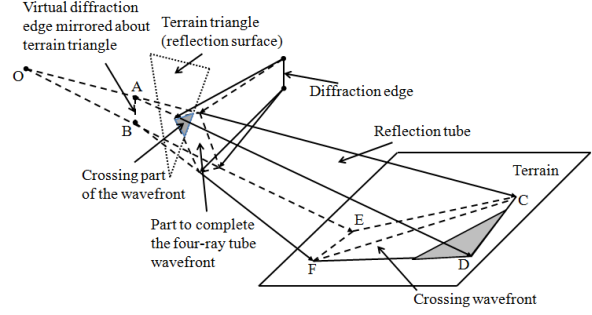

Fig. 2. The four-ray tube reflects on the terrain triangle and crosses with the terrain.

Parameters in Fig. 2 can be expressed as $OA = H_1$, $OB = H_2$, $AC = L_{11}$, $AD = L_{12}$, $BE = L_{21}$, $BF = L_{22}$, $AB = W$, $\angle AOB = \theta$, $\angle CAD = \angle EBF = \alpha$. Use z to represent the length of the segment CF. According to the geometric principle, z can be calculated by the Equation (1):

$$z = \sqrt{x_4{}^2 + x_1 x_2 + \frac{x_2(x_3{}^2 - x_2{}^2)}{x_2 - x_1}}, \quad (1)$$

where

$$\begin{cases} x_1 = \frac{W(L_{11} + H_1)}{H_1} \\ x_2 = \frac{W(L_{22} + H_2)}{H_2} \\ x_3 = \sqrt{\frac{H_2{}^2 L_{11}{}^2}{H_1{}^2} + L_{22}{}^2 - \frac{2H_2 L_{11} L_{22}}{H_1} \cos \alpha} \\ x_4 = \sqrt{\frac{H_1{}^2 L_{22}{}^2}{H_2{}^2} + L_{11}{}^2 - \frac{2H_1 L_{11} L_{22}}{H_2} \cos \alpha} \end{cases} \quad (2)$$

The sides of the quadrilateral CDFE are supposed that $CD = y_1$, $DF = y_2$, $EF = y_3$, $CE = y_4$, and the value of them can be calculated with Equation (3):

$$\begin{cases} y_3 = \sqrt{L_{11}{}^2 + L_{12}{}^2 - 2L_{11} L_{12} \cos \alpha} \\ y_2 = \sqrt{(L_{12} + H_1)^2 + (L_{22} + H_2)^2 - 2(L_{12} + H_1)(L_{22} + H_2) \cos \theta} \\ y_3 = \sqrt{L_{21}{}^2 + L_{22}{}^2 - 2L_{21} L_{22} \cos \alpha} \\ y_4 = \sqrt{(L_{11} + H_1)^2 + (L_{21} + H_2)^2 - 2(L_{11} + H_1)(L_{21} + H_2) \cos \theta} \end{cases} \quad (3)$$

The area of the wavefront CDEF is expressed as S_f. Hence,

$$S_f = \sqrt{p_1(p_1 - y_1)(p_1 - y_2)(p_1 - z)} + \sqrt{p_2(p_2 - y_3)(p_2 - y_4)(p_2 - z)}, \quad (4)$$

where

$$\begin{cases} p_1 = \frac{1}{2}(y_1 + y_2 + z) \\ p_2 = \frac{1}{2}(y_3 + y_4 + z) \end{cases} \quad (5)$$

If the area of every terrain triangle is a, the crossing situation cannot be processed directly when the area of the wavefront of a ray tube is larger than a. So, the ray tube should be subdivided into several new ray tubes with smaller wavefront, and the number of the new ray tubes for every subdivision is c. Provided that every subdivision time is t_1 and the intersection time of every

ray tube is t_2, the processing time of this ray tube for the intersection T_f can be expressed as follows:

$$T_f = \left\lceil \frac{ln\left\lceil \frac{S_f}{a} \right\rceil}{ln\, c} \right\rceil t_1 + \left\lceil \frac{S_f}{a} \right\rceil t_2. \qquad (6)$$

However, since the ratio of the crossing part of the wavefront on the terrain triangle to the completed wavefront is r, the ratio of the area of the shadow on the quadrilateral CDFE to the area of the wavefront CDFE is also r. So, only the rays crossing with the shadow part in the four-ray tube are real rays produced by reflection.

To reduce the unnecessary cost, we define a CSRT model in which every two adjacent rays in a ray tube are not required to be in the same plane. So the profile of a CSRT could be a curve surface. All the rays in the CSRT model must be launched by a same diffraction edge, and there will be a common virtual point source for them. In this paper, the three-ray CSRT model is introduced.

The three-ray CSRT model is produced by connecting the opposite vertex of the quadrilateral wavefront to divide the four-ray tube into two ray tubes with triangular wavefront (Fig. 1 (a)), so the wavefront of the three-ray CSRTs launched from an edge can also cover the cylindrical diffraction wavefront. The CSRT model in Fig. 3 is launched from diffraction edge AB. Supposing that the rays AC and BD are in the same plane, so the ray AE is in the different plane with ray BD. The profile ABDE is a curve surface consisted of the rays launched from the edge AB to the line DE. For all the rays in this tube, there must be a common virtual launch point before the diffraction. Combined with the UTD, diffraction rays in CSRT launched by edge AB will never cross with each other during the propagation process (except the points on the edge AB). So there will be no rays passing through the curve surface and go into another ray tube, which proves the three-ray CSRT model to be appropriate for wave propagation prediction.
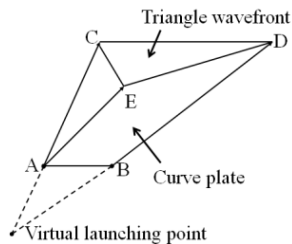

Fig. 3. The CSRT model.

The CSRT model has no strict requirements on whether the adjacent rays are in the same plane. So when a three-ray CSRT intersects with the terrain triangles, no matter what the shape of the intersection wavefront is, it always can be divided into some triangle wavefronts. Thus, all the rays in reflection three-ray tubes are real rays produced by reflection.

If the CSRT model is used in Fig. 2, only the crossing part will reflect. The crossing part of the wavefront of the CSRT and the terrain is the shadow part exactly. So the area of the wavefront of the CSRT S_{CSRT} is:

$$S_{CSRT} = rS_f, \qquad (7)$$

and the handling time T_{CSRT} of the CSRT method can be calculated as follows:

$$T_{CSRT} = \left\lceil \frac{\ln\left\lceil \frac{S_{CSRT}}{a} \right\rceil}{\ln\, c} \right\rceil t_1 + \left\lceil \frac{S_{CSRT}}{a} \right\rceil t_2. \qquad (8)$$

So, the time ratio of the four-ray tube and the three-ray CSRT is indicated as:

$$\eta = \frac{T_f}{T_{CSRT}}. \qquad (9)$$

The parameters and the constants in the Equations (1) - (8) are assumed as the following values: $H_1 = H_2 = 10$ m, $L_{11} = L_{21} = 10000$ m, $L_{12} = L_{22} = 1000\,m$, $W = 10\,m$, $\theta = \pi/3$, $\alpha = \pi/6$, $r = 1/4$, $a = 100\,m^2$, $c = 4$. It can be calculated that $T_f = 10t_1 + 438831t_2$, $T_{CSRT} = 9t_1 + 109708t_2$. Since that t_1 is very small and can be ignored when compared with t_2, it is concluded that $\eta \approx 4$.

Thus, the calculation efficiency of the three-ray CSRT model has been increased by 4 times compared with the four-ray tube model in the above scenario. It is an efficient way with the CSRT model for ray tracing process in the complex terrain.

III. DIFFRENT SITUATIONS OF RAY TUBE CROSSING WITH THE TERRAIN

When a CSRT crosses with terrain triangles, there will be several different crossing situations for the wavefront of the ray tube. The three-ray CSRT model can self-adaptively deal with the situations as follows.

A. Completely crossing

When the three-ray CSRT model intersects with a terrain triangle completely (Fig. 4 (a)), all the rays in the tube will reflect from this triangle. It just needs to obtain the reflection rays of the three rays AC, AD and BE to form the new reflection three-ray CSRT. At the same time, it is also necessary to get mirror point O' of O about the terrain triangle as well as mirror edge A'B'. O' and A'B' will be applied to the next tracing step as virtual launching point and virtual launching edge.

B. Partly crossing with a terrain triangle

When the ray tube partly intersects with a terrain triangle, different treatments will be applied to different situations of intersection. If the wavefront of the intersecting part is triangular, it only needs to find the diffraction points of the vertexes of the triangular wavefront and to restructure the three-ray CSRT. For the new CSRT, a reflection ray tube can be produced according to the steps of Subsection A. However, if the

wavefront of the intersecting part is not a triangle, the ray tube should be segmented. The polygon wavefront can be divided into several triangular wavefronts. In Fig. 4 (b), the wavefront of the crossing part is an irregular polygon DEGH. The irregular polygon wavefront is divided into two triangular DEH and EGH by connecting points H and E. Find the diffraction points A and G of the new vertexes of wavefronts H and G on the edge AB, and two CSRTs determined by rays AH, AD, BE and rays AH, FG, BE are formed. The reflection ray tubes of this two new CSRTs can be produced based on the treatment in Subsection A.
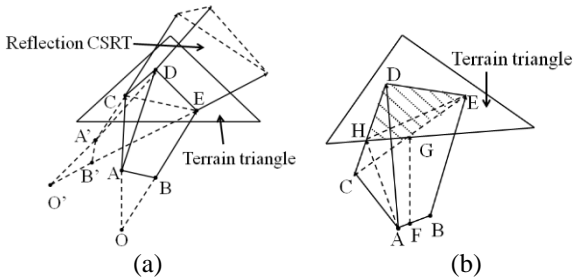
Fig. 4. (a) Completely crossing with terrain triangle. (b) Partly crossing with a terrain triangle.

C. Intersecting with adjacent terrain triangles

When the ray tube intersects with two adjacent terrain triangles (Fig. 5 (a)), the wavefronts CFG and DEGF are on two terrain triangles, so the two wavefronts can be treated as method in Subsection B respectively.
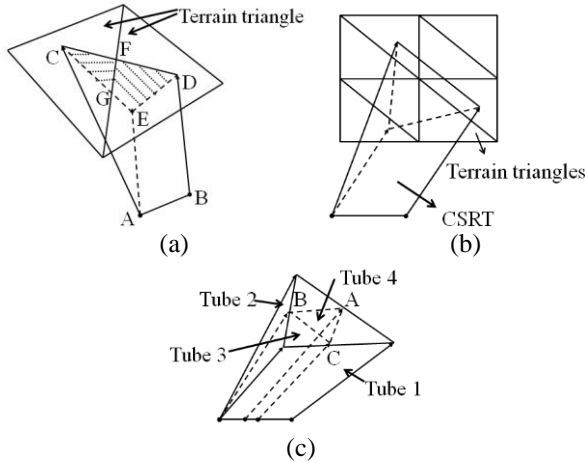
Fig. 5. (a) Crossing with two terrain triangle. (b) Crossing with several terrain triangles. (c) Subdivide ray tube.

D. Intersecting with several terrain triangles

If the ray tube intersects with several terrain triangles (Fig. 5 (b)), since the terrain triangles are not closely associated, it is difficult to determine the specific

situations of intersection usually. To reduce the complexity of crossing situations, it is necessary to get the ray tube segmented. First, we suppose a wavefront of the three-ray CSRT, and then get the midpoints of each edge of it (Fig. 5 (c)). Connection of the midpoints A, B and C will divide the triangle wavefront into four triangles. Next, we get the launching points of these three points on the launching edge, so the ray tube will be segmented into four new three-ray CSRTs with smaller wavefronts.

IV. RAY TRACING PROCESS

The three-ray CSRT model proposed in this paper is mainly used to trace diffraction rays. So the actual ray tracing process considering transmission and reflection should combine this model with the point source launching three-ray tube model. For simplification, this paper only considers the situations in which only one diffraction and multiple reflections occur. The flow chart of the ray tracing is shown as Fig. 6.
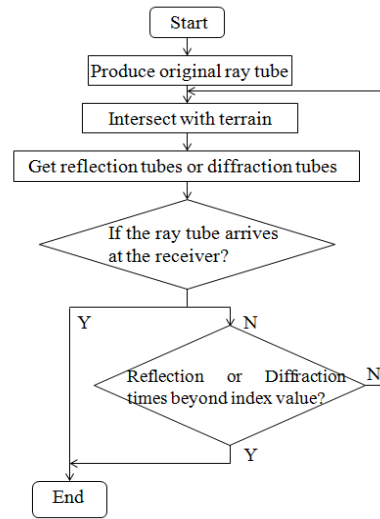

Fig. 6. The flow chart of the ray tracing.

A. Produce initial ray tube

The initial point source launching three-ray rubes are generated through the icosahedron method proposed by [8]. During the process of tracing, all the ray tubes will have triangular wavefronts and same crossing situations with the terrain triangles. So different kinds of ray tubes can be processed in a unified way.

B. Diffraction and reflection

The initial ray tubes or the high order reflection ray tubes will diffract from the crossing lines of the terrain triangles if the lines are diffraction edges, so the three-ray CSRTs will be produced. Besides, the other parts of these ray tubes crossing with terrain will reflect from the terrain and produce reflected ray tubes.

C. Judgment of the reception

During the ray tracing, it should be determined whether the ray tube illuminates the receiver. The ray tube illuminates the receiver when the receiver is in the area covered by the ray tube and the ray tube does not cross with other terrain triangles before arriving it.

V. SIMULATIONS AND COMPARISONS

The simulation software was developed by putting the ray tracing process based on the CSRT model and the four-ray tube model into the codes. Simulation results of several different terrains using this software are displayed in this part. The typical terrain formed by several terrain triangles and the actual complex terrain from the electric map were both investigated.

In Fig. 7, there are two parallel diffraction edges in the terrain. A transmitter (Tx (17.86, 576.55, 223.46)) and a receiver (Rx (330.89, 269.15, 172.70)) were placed on the terrain. The distance between the Tx and the Rx is 441.65 m. The paths simulated by the tracing methods based on the CSRT model and the four-ray tube model are exactly same, which are shown in Fig. 7. There are 7 paths totally, which are in accord with the theoretical result obviously. From Fig. 7 we can see that several diffraction paths are included, which prove that the CSRT model works well in predicting diffraction paths.
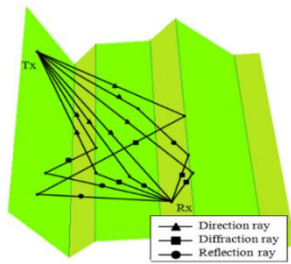

Fig. 7. Terrain with parallel diffraction edges.

The terrain in Fig. 8 is same as that in Fig. 7. The only difference is that one of the diffraction edges in Fig. 8 is rotated so that the two diffraction edges are not parallel. All the 5 possible paths are predicted and displayed in Fig. 8. The method based on the CSRT model is accurate and applicable in different diffraction environment.
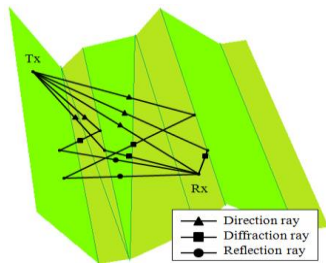

Fig. 8. Terrain with nonparallel diffraction edges.

Table 1 shows the computational time and E-field at the point of Rx in four different environments simulated by the CSRT model tracing method and the conventional four-ray tube model tracing method. The excitation frequency is 1000 MHz. In the Table 1, the Terrain 3 and the Terrain 4 are both actual environment cut from the real electric map. The size of the Terrain 3 is 2×2.2 km^2 (from 42°19'26.6035"N and 82°50'25.8125"E to 42°18'25.7818"N and 82°52'4.7458"E), and the distance between the Tx and the Rx was 609.63 m. The size of the Terrain 4 is 9.5×10 km^2 (from 42°21'31.6139"N and 82°48'28.3466"E to 42°16'44.1722"N and 82°55'40.7631"E) and the distance between the Tx and Rx is 439.60 m.

Table 1: The comparison of calculation time and E-field

Scenario	Computational Time(s)		E-field (V/m)		
	The CSRT Model	The Four-Ray Tube Model	The CSRT Model	The Four-Ray Tube Model	Error
Fig. 7 (0.75×0.56km^2)	90	91	2.23	2.2	1.36%
Fig. 8 (0.75×0.56km^2)	116	112	1.86	1.86	0
Terrain 3 (2×2.2km^2)	1003	1683	0.95	1.01	5.94%
Terrain 4 (9.5×10km^2)	8090	9523	1.54	1.62	4.94%

The complexity of the scenarios in the Table 1 increases with the increase of the terrain size. The results show that the four-ray tube model tracing method and the CSRT model tracing method use similar computational time when they are applied in the simple scenarios in Fig. 7 and Fig. 8. However, as the scenarios become more complex, the CSRT model tracing method spent less computational time. The errors of the E-field at the point of Rx between the CSRT model and the four-ray tube model are also listed in the Table 1. The average error is only 3.06%, which proves the high accuracy of the CSRT model tracing method.

VI. CONCLUSION

This paper introduced a three-ray CSRT model, which is suitable for the diffraction calculation in ray tracing. The CSRT model is accurate and has great advantages over the segment source launching four-ray rube model in efficiency.

The algorithm presented in this paper just considers one diffraction and multiple reflections. In practice, the CSRT model can be used to calculate high order diffraction paths. When the CSRT model is used to produce high order diffraction ray tubes, the rays in new tubes may cross with others, so it is necessary to do some special treatment which can be studied in the next steps.

REFERENCES

[1] H.-W. Son and N.-H. Myung, "A deterministic ray tube method for microcellular wave propagation prediction model," *IEEE Trans. Antennas Propagat.*, vol. 47, no. 8, pp. 1344-1350, 1999.

[2] S. Y. Tan, M. Y. Tan, and H. S. Tan, "Multipath delay measurements and modeling for interfloor wireless communications," *IEEE Trans. Veh. Technol.*, vol. 49, no. 4, pp. 1334-1341, 2000.

[3] C. Oestges, B. Clerckx, L. Raynaud, and D. Vanhoenacker-Janvier, "Deterministic channel modeling and performance simulation of micro-cellular wide-band communication systems," *IEEE Trans. Veh. Technol.*, vol. 51, no. 6, pp. 1422-1430, 2002.

[4] G. Carluccio and M. Albani, "An efficient ray tracing algorithm for multiple straight wedge diffraction," *IEEE Trans. Antennas Propagat.*, vol. 56, no. 11, pp. 3534-3542, 2008.

[5] C. Saeidi, A. Fard, and F. Hodjatkashani, "Full three-dimensional radio wave propagation pre-iction model," *IEEE Trans. Antennas Propagat.*, vol. 60, no. 5, pp. 2462-2471, 2012.

[6] C. Saeidi, F. Hodjatkashani, and A. Fard, "New tube-based shooting and bouncing ray tracing method," *Proc. IEEE ATC*, Hai Phong, Vietnam, pp. 269-273, Oct. 12-14, 2009.

[7] S.-H. Chen and S.-K. Jeng, "SBR image approach for radio wave propagation in tunnels with and without traffic," *IEEE Trans. Veh. Technol.*, vol. 45, no. 3, pp. 570-578, 1996.

[8] S.-H. Chen and S.-K. Jeng, "An SBR/image approach for radio wave propagation in indoor environments with metallic furniture," *IEEE Trans. Antennas Propagat.*, vol. 45, no. 1, pp. 98-106, 1997.

[9] Y. B. Tao, H. Lin, and H. J. Bao, "Adaptive aperture partition in shooting and bouncing ray method," *IEEE Trans. Antennas Propagat.*, vol. 59, no. 9, pp. 3347-3357, 2011.

[10] H. Ling, R. Chou, and S. Lee, "Shooting and bouncing rays: Calculating the RCS of an arbitrarily shaped cavity," *IEEE Trans. Antennas Propagat.*, vol. 37, pp. 194-205, 1989.

[11] R. Burkholder and P. Pathak, "Computing the time domain EM scattering from large open-ended cavities using the SBR and GRE ray shooting methods," *in 9th Annual Review of Progress in Applied Computational Electromagnetics*, pp. 602-617, 1993.

[12] J. M. Baden and V. K. Tripp, "Ray reversal in SBR RCS calculations," *in 31st International Review of Progress in Applied Computational Electromagnetics*, pp. 1-2, 2015.

[13] S. Y. Seidel and T. S. Rappaport, "Site-specific propagation prediction for wireless in-building personal communication system design," *IEEE Trans. Veh. Technol.*, vol. 43, pp. 879-891, Nov. 1994.

[14] C.-F. Yang, B.-C. Wu, and C.-J. Ko, "A ray-tracing method for modeling indoor wave propagation and penetration," *IEEE Trans. Antennas Propagat.*, vol. 46, no. 6, pp. 907-919, 1998.

[15] G. Liang and H. L. Bertoni, "A new approach to 3-D ray tracing for propagation prediction in cities," *IEEE Trans. Antennas Propagat.*, vol. 46, no. 6, pp. 853-863, 1998.

[16] P. Bernardi, R. Cicchetti, and O. Testa, "An accurate UTD model for the analysis of complex indoor radio environments in microwave WLAN systems," *IEEE Trans. Antennas Propagat.*, vol. 52, no. 6, pp. 1509-1520, 2004.

Dan Shi received her Ph.D. degree in Electronic Engineering from BUPT in Beijing, China in 2008. Now she is an Associate Professor in Beijing University of Posts and Telecommunications. Her research interests include electromagnetic environment and electromagnetic computation.

Na Lv received her Bachelor degree in Communication Engineering from BUPT in Beijing, China in 2015. Now she is studying for Master degree in Beijing University of Posts and Telecommunications in Beijing, China.

Yougong Gao received his B.S. degree in Electrical Engineering from National Wuhan University, China in 1950. He is now a Professor and Ph.D. Supervisor in Beijing University of Posts and Telecomm-unications, China.

A GPU Implementation of a Shooting and Bouncing Ray Tracing Method for Radio Wave Propagation

Dan Shi, Xiaohe Tang, Chu Wang, Ming Zhao, and Yougang Gao

School of Electronic Engineering
Beijing University of Posts and Telecommunications, Beijing, 100876, China
shidan@buptemc.com

Abstract ─ Shooting and bouncing ray tracing method (SBR) is widely adopted in radio wave propagation simulations. Compared with the center-ray tube model, the lateral-ray tube model is more accurate but more time consuming. As a result, we use graphics processing unit (GPU) to accelerate the lateral-ray tube model. In this paper, we proposed a GPU-Based shooting and bouncing lateral-ray tube tracing method that is applied to predicting the radio wave propagation. The numerical experiment demonstrates that the GPU-based SBR can significantly improve the computational efficiency of lateral-ray tube model about 16 times faster, while providing the same accuracy as the CPU-based SBR. The most efficient mode of transferring the data of triangle faces is also discussed.

Index Terms ─ Compute unified device architecture (CUDA), graphics processing unit (GPU), radio wave propagation, ray tracing, shooting and bouncing ray (SBR).

I. INTRODUCTION

In the past few decades, electromagnetic environment (EME) simulation technology has been growing in its popularity, for it is significant both for military use and for civil use. As a result, various computational electromagnetic methods have been applied in this field. Among all kinds of computational methods, the shooting and bouncing ray (SBR) [1, 2] tracing method is a high frequency asymptotic one for calculating the radio wave propagation through environments with regions of reflecting surfaces, diffracting edges and so on [3]. At present, there are several models proposed, which have their own characteristics. Tube creating can be categorized into two different schemes using center-ray tubes (a ray is shot from the center of the patch wavefront) or lateral-ray tubes (rays are shot from vertices of the patch wavefront), depending on the number of rays chosen to build a tube. The ray cone is a kind of center-ray tube. When the rays transmitted are treated as ray cones, overlap and double counting are unavoidable because of the spherical wavefront during the propagation process

[4-7]. But regular polygons such as triangles, squares and hexagons can completely cover an area without leaving gaps or existing overlaps. Using lateral-ray tube tracing methods can get a more accurate result than using center-ray tube tracing methods. However, the cost of tracing lateral-ray tubes is much higher than tracing center-ray tubes [8]. Therefore, we propose to use the graphics processing unit (GPU) to accelerate the shooting and bouncing lateral-ray tube method.

It is obvious that ray tracing is well suitable for parallel processing due to the independence of rays [9]. Carr et al. first implemented the ray-triangle intersection on the GPU in 2002 [10]. Tao used center-ray tube model to trace the valid tubes in the radar cross section (RCS) prediction on the GPU in 2010 [11]. In this paper, abandoning the inaccurate center-ray tube model, we use the lateral-ray tube model and fully implement the shooting and bouncing lateral-ray tube tracing method on the GPU.

This paper is organized as follows. Section II discusses the method of GPU-Based shooting and bouncing lateral-ray tube tracing. In Section III, modeling and implementation details is introduced. In Section IV, the results and discussion are given. Last section is the conclusion.

II. GPU-BASED SBR

GPU is a specialized device that has many cores working together. Typically, every 32 threads compose a warp which is the basic executing unit of the GPU, and the 32 threads execute the same instruction on different data simultaneously [12]. This effectively reduces the memory access delay by 32 times.

In software, a typical compute unified device architecture (CUDA) program consists of two parts. One part is the CPU codes that control the process of the whole program, and the other part is the GPU part that does the parallel work [13]. A function that executes on the GPU is typically called a "kernel" [14].

The procedure of the GPU-Based shooting and bouncing lateral-ray tube tracing method is divided into three steps. They are, generating original ray tubes,

reflecting calculation, and diffracting calculation. Among all the steps, reflecting calculation and diffracting calculation executes their kernels separately. The details of these steps are discussed in Section II-A through Section II-C.

A. Generating lateral-ray tubes from a transmitter

The transmitter is modeled as a point source, and for purpose of considering all possible angles of departure of rays, a regular icosahedron is inscribed inside the unit sphere. To achieve better resolution, each face of the icosahedron is tessellated into N equal segments where N is the tessellation. Rays are launched through icosahedron vertices and at the intersection points of tessellated triangle faces. Figure 1 shows an example with N = 32, which is used in our model. This method of launching the source rays provides wavefronts that completely subdivide the surface of the unit sphere with nearly equal shape and area [4]. An original ray tube is composed of three adjacent rays as Fig. 1 illustrates.
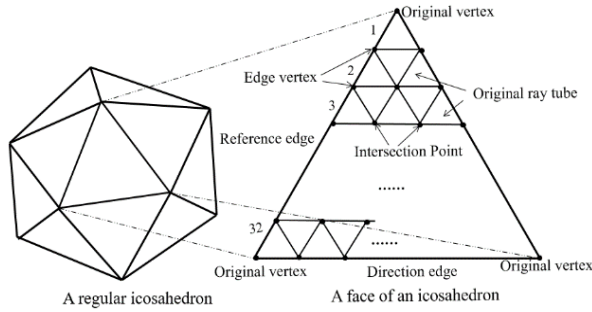
Fig. 1. A regular icosahedron and tessellation of icosahedron face.

B. Intersection tests and reflecting calculation

The CUDA program traces all original ray tubes synchronously. Parallelism is introduced by running main threads scheduling child thread that accomplishes the calculation, and each child thread shows up as a separate process.

The heart of the matter is to distribute the computation to over ten thousand of individual, controllable, and analogous threads. Since every thread is supposed to perform almost the same task, the distribution appears particularly significant, which signifies that we should ensure every distributed computation process resembles each other so that a universal kernel function (consistent input and output, same calculation formula, etc.) can be the template for every child thread. Therefore, we assign a CUDA thread to a single ray tube. A thread merely traces one single ray tube, which ensures the independence and the similarity of different CUDA threads.

The most time-consuming part is the intersection tests of ray tubes as follows:

1) Calculating the reflection point

Any point on the ray can be represented as $\vec{O} + t\vec{r}$ (where $\vec{O}$ represents the original point of the ray, $\vec{r}$ represents the direction vector of the ray, t represents the distance coefficient, if $t > 0$, then it represents the point is in the positive direction) as Fig. 2 shows, and any point inside a triangle face can be represented as $u\overrightarrow{AB} + v\overrightarrow{AC} + \vec{A}$ (where u and v represent the distance coefficient of $\overrightarrow{AB}$ and $\overrightarrow{AC}$, if $0 < u < 1$, $0 < v < 1$, $0 < u + v < 1$, then it represents the point is inside the triangle ABC as Fig. 3 shows:

$$\vec{O} + t\vec{r} = u(\vec{B} - \vec{A}) + v(\vec{C} - \vec{A}) + \vec{A}, \qquad (1)$$

$$t\vec{r} - u(\vec{B} - \vec{A}) - v(\vec{C} - \vec{A}) = \vec{A} - \vec{O}. \qquad (2)$$

Let $\alpha_1 = \vec{r}$, $\alpha_2 = \vec{B} - \vec{A}$, $\alpha_3 = \vec{C} - \vec{A}$, $\beta = \vec{A} - \vec{O}$, then,

$$\alpha_1 t - \alpha_2 u - \alpha_3 v = \beta.$$

Let $d = |\alpha_1 \ \alpha_2 \ \alpha_3|$, if $d \neq 0$, on the basis of Cramer's Rule [15]:

$$t = \frac{|\beta \ \alpha_2 \ \alpha_3|}{d}, u = \frac{|\alpha_1 \ \beta \ \alpha_3|}{d}, v = \frac{|\alpha_1 \ \alpha_2 \ \beta|}{d}.$$
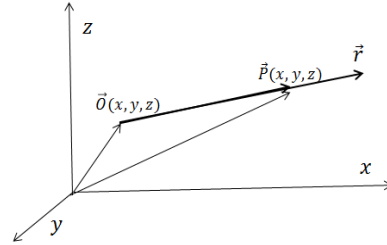$$\text{If } 0 < u < 1, \ 0 < v < 1 \quad 0 < u + v < 1. \qquad (3)$$

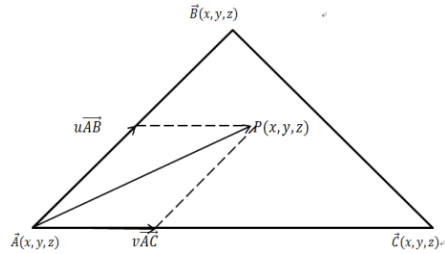Fig. 2. Point $\vec{P}$ on a ray $\vec{r}$.

Fig. 3. Point $\vec{P}$ inside a triangle ABC.

Then it represents the intersection point is in the positive direction of the ray and inside the triangle face as well, where t represents the distance between the original point and the reflection point. Loop the computation with all faces, then compare t, intersection point with minimum t value is the reflection point and go to step 2). However, if the result does not meet (3), it represents that the ray has not intersected with the buildings or terrains, and step 2) is supposed to be skipped.

2) Calculating the reflection vector

As is shown in Fig. 4, $\vec{i}$ is the normalized incident vector, $\vec{r}$ is the normalized reflection vector, and $\vec{n}$ is the normal vector of a triangle face. Angle of incidence equals to the angle of reflection, therefore quadrangle MONQ is a rhombus, so $OQ = 2OP$. On basis of step 1), the coordinate of O is deterministic.

Solve the equation to calculate $\vec{r}$:

$$\vec{r} = \vec{i} - 2\overrightarrow{PO} = \vec{i} - 2(\vec{i} \cdot \vec{n})\vec{n}, \qquad (4)$$

where $\vec{n} = \frac{\overrightarrow{AB} \times \overrightarrow{AC}}{|\overrightarrow{AB} \times \overrightarrow{AC}|}$, $\vec{A}$, $\vec{B}$, $\vec{C}$ are the vertices of a triangle face.

3) Case analysis

If neither of a ray of the ray tube has an intersection point (case 0), this ray tube is discarded. If some or all three rays have intersection points (case 1, 2, 3, 4 and 5), it is necessary to consider all kinds of reflection and diffraction cases based on the coordinate of intersection points:

0. three rays do not intersect a building;
1. three rays intersect the same face of a building;
2. one rays intersect a face of a building while the other two do not;
3. two rays intersect the same face of a building while the other one does not;
4. two rays intersect two adjacent face of a building while the other one does not;
5. two rays intersect the same face of a building while the other one intersects an adjacent face of a building.
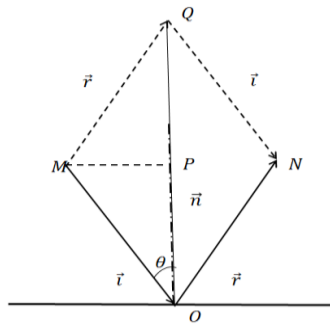

Fig. 4. A ray $\vec{i}$ intersects with a plane.

We mainly consider six cases above. It is obvious that the reflection exists in all cases except case 0 while diffraction does not exist in case 0 and 1. Figure 5 shows five cases of ray tubes intersecting the building faces. As for case 2, 3, 4, 5, each thread will calculate the coordinates of diffraction edges.

GPU specializes in tedious repetitive numerical calculation and is weak in dealing with complicated logic structure; hence it is reasonable to run highly intensive computational task on the GPU like solving equations in step 1) and 2). Parallel numerical calculation indicates that when the amount of incident ray tubes is large and the formulas are complex, the acceleration effect is particularly obvious compared with CPU serial programs.
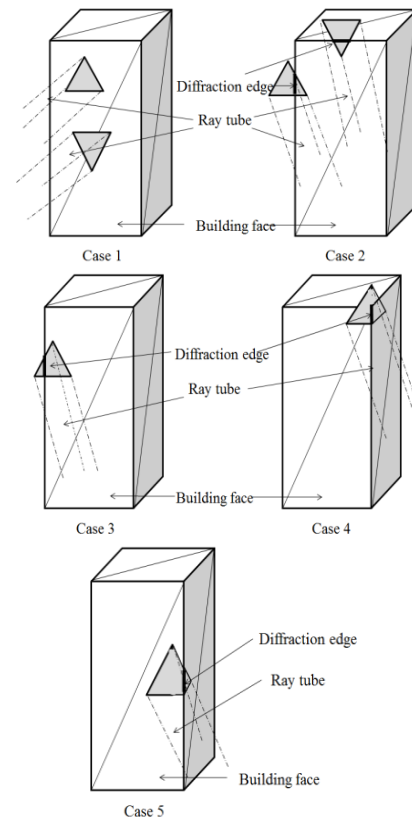

Fig. 5. Five cases that ray tubes intersect with building faces.

C. Generating diffracting rays

Once the wavefront of a ray tube illuminates an edge of two adjacent faces and the two adjacent faces make up a wedge, this ray tube will generate diffraction rays. The following paragraphs will show the procedure.

A single GPU thread represents an incident ray tube to be diffracted. Based on the incident ray tube and the diffraction edge, we can get an original point of the incident ray tube and two intersections of the wavefront of the incident ray tube with diffraction edge. Then, two virtual incident rays are created. Each of them generates a group of diffraction rays. We need to specify the count N of the generated diffraction rays. Suppose the dihedral angle of the two adjacent faces, which can make up a wedge, is θ. The cross section of the circular cone, which is a sector, can be divided into N-1 parts with the angle of $\frac{360-\theta}{N-1}$. As a result, the N-1 parts are able to construct N-1 ray tubes of which the wavefront is a quadrangle, as is shown in Fig. 6. Considering the consecutive thread ID, we can get three arrays, A[i], B[i] and R[i]. Among

the three arrays, A[i] and B[i] contain the diffraction rays to be generated, and the other one R[i] contains the diffraction ray tubes which consist of the diffraction rays in the first two arrays. As is shown in Fig. 7, we use i to represent the ray tube number. The relationship between diffraction rays and diffraction ray tubes is also shown. Besides, the ray tube number i is in a loop from (idx * N) to (idx+1) * N, in which idx means thread ID.

Different with original ray tubes and reflection ray tubes, the diffraction ray tubes are quadrangle ray tubes, which means each lateral-ray tube consist of four rays.
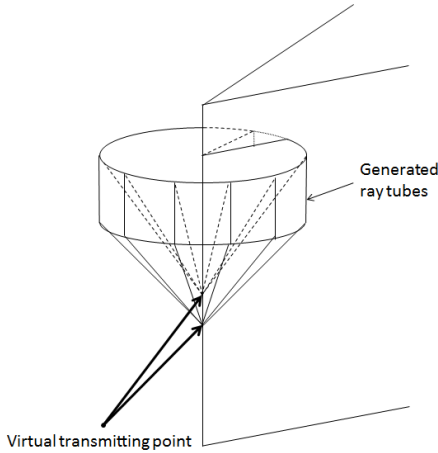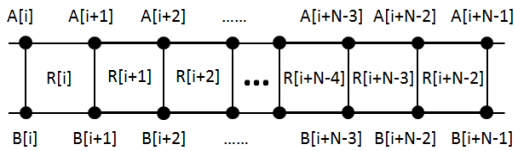

Fig. 6. Generating ray tubes from diffracting edge.

Fig. 7. Data structure of diffraction rays and ray tubes.

III. MODELING AND IMPLEMENTATION

To verify the efficiency of the proposed GPU-based shooting and bouncing lateral-ray tube tracing method, a CPU-based version is also implemented for comparison. A model is established, and several numerical examples are tested. The GPU hardware used in this research is Quadro K620 of Compute Capability 5.0, with 2 GB of memory. The CPU hardware used in this research is Intel(R) Xeon(R) CPU E5-2603 v3 @ 1.60 GHz with 6 cores. Our implementation runs atop Windows 7 with the CUDA Toolkit 7.5. As all future NVIDIA GPUs will support CUDA, the proposed GPU-based SBR is scalable across future generations.

CUDA provides a simple and general C/C++ language interface to the programmers and the programming on GPU does not have much difference from using application programming interfaces.

The GPU-based shooting and bouncing lateral-ray

tube tracing method is applied to a sample environment. There are 4 buildings set on the terrain. All the buildings are with the same height, which is 100 m above the terrain. The entire model is made up of 19650 triangle faces. The material parameter of the buildings is $\varepsilon_r = 15$, $\sigma = 0.015$. The material parameter of the ground is $\varepsilon_r = 25$, $\sigma = 0.02$. Considering the architecture of the transmitter is a regular icosahedron, we can estimate the complexity according to the subdivision coefficient. In this sample, we set the subdivision coefficient to 32. As a result, 20480 original triangle ray tubes are generated from the transmitter. There are 2 groups of receivers. One is made up of receivers ranging from (0, 0, 50) to (0, 160, 50) with a 20 - m step. The other group is made up of receivers ranging from (0, 0, 20) to (0, 0, 100) with a 10 - m step. The modeling is shown in Fig. 8.
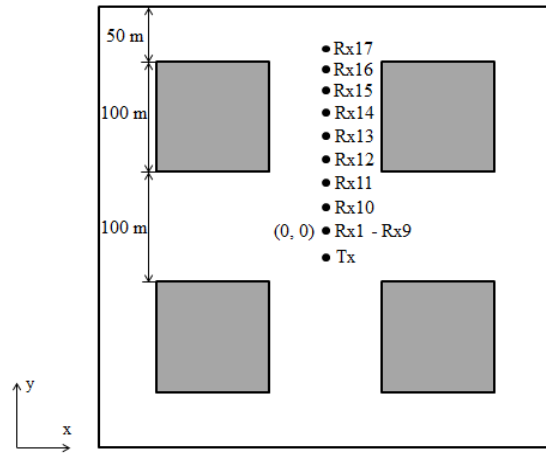

Fig. 8. A sample model of propagation environment.

The data of the terrain and the buildings are imported from the electronic map. All the data necessary in the experiment including the terrain and buildings are saved in the global memory. In CUDA programming, the number of blocks and threads per block is specified by the programmer, and each thread has a unique thread ID and block ID to identify the unique data assigned to each thread. As a result, each lateral-ray tube can be specified through thread ID and block ID. In our experiment, considering the 20480 original triangle ray tubes, the maximum block size and the thread count in per block in our implementation is 32×640. In addition, because of the limited device memory, we cannot transfer all the triangle faces data into the GPU. We resolve this problem by transferring the data in batches.

IV. RESULTS AND DISCUSSION

Last part we introduced the modeling, knowing that there are 19650 triangle faces and 20480 original triangle ray tubes. Figure 9 and Fig. 10 show the E field vs. receiver distance and E field vs. receiver height. Both

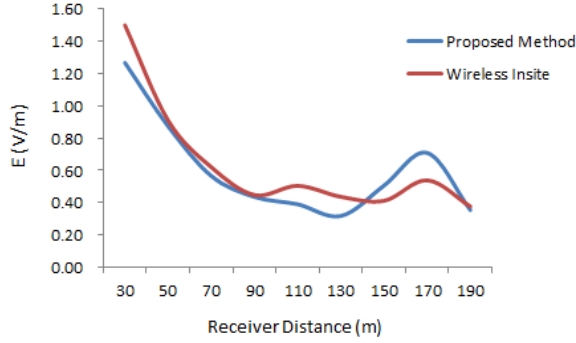are compared with the commercial electromagnetic simulation software Wireless Insite.

Fig. 9. Comparison of E field vs. receiver distance with proposed method and Wireless Insite simulation.

In Fig. 9, the heights of the transmitter and the receivers are all 50 m. Since the distance between the transmitter and the receivers varies from 30 m to 190 m with a 20 - m step, the E field decreases in general. However, under the influence of the building reflection, the E field decreases slowly even grows a little when the distance becomes longer and longer.
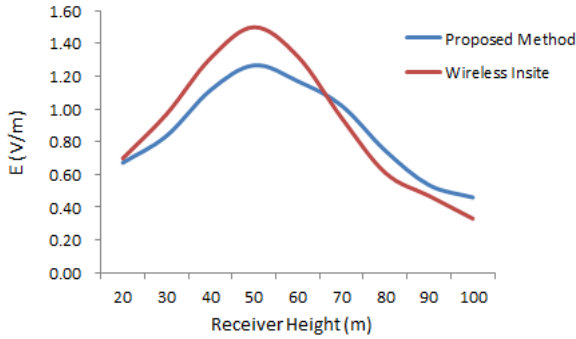

Fig. 10. Comparison of E field vs. receiver height with proposed method and Wireless Insite simulation.

In Fig. 10, the height of the transmitter is 50 m. The horizontal distance between the transmitter and all the receivers is 30 m. Since the height of the receivers varies from 20 m to 100 m with a 10 - m step, the distance between the transmitter and the receivers decreases at first and then increases with the receiver height. As a result, the electric field increases at first for the receiver becomes closer to the transmitter. However, for the receivers above 50 m, the electric field decreases with the increase of receiver height.

From the Table 1, we can get the information that the execution speed on the GPU is more than 16 times higher than CPU.

Table 1: Comparisons between execution time for CPU and GPU

Type	Time
Executing on CPU	140122 ms
Executing on GPU	8706 ms

Below we will put emphasis on analyzing the factors which affect the executing time.

The executing time on the CPU is as follow:

$$t_{CPU} = \frac{N}{f_{CPU}} \times \frac{1}{C_{CPU}} \times \frac{1}{\eta}, \tag{5}$$

where N represents the data scale inputted, f_{CPU} represents the CPU frequency and C_{CPU} represents the CPU's capability of calculation, η represents the efficiency of the algorithm.

We pay more attention to the factors which affect the executing time on the GPU. The formula is shown as follow:

$$t_{GPU} = t_{kernel} + t_{memcpy}$$
$$= t_n \times \lfloor \frac{N}{n} \rfloor + t_{N \bmod n} + t_m \times \lceil \frac{N}{n} \rceil, \tag{6}$$
$$t_n = \frac{n}{f_{GPU}} \times \frac{1}{C_{GPU}} \times \frac{1}{\eta} + n \times a, \tag{7}$$
$$t_0 = 0, \tag{8}$$

where t_{GPU} represents the total execution time on the GPU, t_{kernel} represents the execution time cost in the kernel functions, t_{memcpy} represents the time spent on copying data from the GPU to the CPU, N represents the data scale inputted, n represents the data scale inputted per time, $\lfloor \frac{N}{n} \rfloor$ represents rounding down to $\frac{N}{n}$, $\lceil \frac{N}{n} \rceil$ represents rounding up to $\frac{N}{n}$, t_n represents the computation time with n triangle faces transferred, t_m represents the time spent on copying the data once, f_{GPU} represents the GPU frequency, C_{GPU} represents the GPU's capability of calculation, η represents the efficiency of the algorithm, and a is a constant which affects the speed of copying memory changing with different GPUs.

Because of the limited GPU memory, we cannot copy all the data from the CPU to the GPU. As a result, we should divide the data into several parts. Then we copy each part from the CPU to the GPU. We do not copy the second part of the data until the first part of the data has been calculated. So do the rest parts of the data. This is the reason why $\frac{N}{n}$ is in the formula. The GPU frequency influences the memory clock rate so the frequency is higher the more time is saved. Additionally, the capability of the GPU is stronger, the more time is saved.

In the formula (6), $\frac{N}{n}$ is decided by programmers. In our experiment, N depends on the count of triangle faces and the count of original ray tubes. We divide all the 19626 triangle faces into several groups. Meanwhile, we test the time of the intersection test which is the most

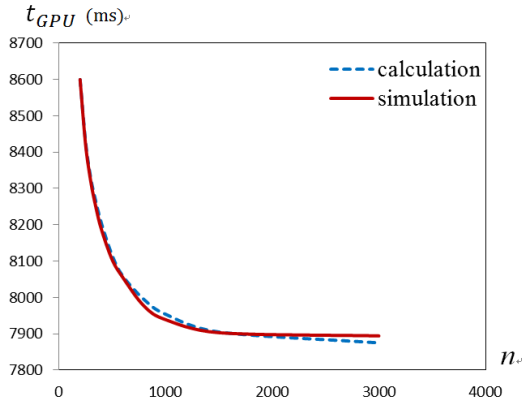time-consuming part of the whole experiment. As is shown in Fig. 11.

Fig. 11. Computation time on the GPU predicted and measured.

In the formula (6), as the n grows, $t_n \times \lfloor \frac{N}{n} \rfloor + t_{N \bmod n}$, which is t_{kernel}, does not change. t_m changes slightly, too. So the formula (6) mainly depends on $\lceil \frac{N}{n} \rceil$. Therefore, we should try our best to get the biggest n to enhance the efficiency. We treat $n = 200$ as a basic unit. Then we predict the calculation time by the formula (6), as is shown in Fig. 11. For our GPU, the biggest n is up to 4500. If $n > 4500$, there will not be enough space to save the data. So in the example of the comparisons of the CPU and the GPU, the n of the GPU is chosen as 4500.

For the efficiency of algorithm, we can use the shared memory to store the triangle face information instead of global memory to save time. Proper distribution way of blocks and threads also reduces the total execution time. In addition, improvement of access mode can increase the operation efficiency, too.

V. CONCLUSION

This paper mainly introduced a GPU-Based shooting and bouncing lateral-ray tube tracing method that is applied to predicting the radio wave propagation. This method can be applied in electrically large scenes which is time-consuming. Then we discussed the most efficient mode of transferring the data of triangle faces, which is a necessary part in the shooting and bouncing ray tracing algorithm. The results proved that the method can greatly reduce the computation time. Moreover, this proposed method can be implemented on the future GPU devices which support the CUDA programming.

REFERENCES

[1] H. Ling, R. C. Chow, and S. W. Lee, "Shooting and bouncing rays: Calculating the RCS of an arbitrarily shaped cavity," *IEEE Trans. Antennas Propag.*, vol. 37, no. 2, pp. 194-205, 1989.

[2] J. Baldauf, S. W. Lee, L. Lin, S. K. Jeng, S. M. Scarborough, and C. L. Yu, "High frequency scattering from trihedral corner reflectors and other benchmark targets: SBR vs. experiments," *IEEE Trans. Antennas Propag.*, vol. 39, no. 9, pp. 1345-1351, 1991.

[3] F. Weinmann, "UTD shooting-and-bouncing extension to a PO/PTD ray tracing algorithm," *Applied Computational Electromagnetics Society Journal*, vol. 24, no. 3, pp. 281-293, June 2009.

[4] S. Y. Seidel and T. S. Rappaport, "Site-specific propagation prediction for wireless in-building personal communication system design," *IEEE Trans. Veh. Technol.*, vol. 43, pp. 879-891, Nov. 1994.

[5] S. Chen and S. Jeng, "An SBR/image approach for radio wave propagation in indoor environments with metallic furniture," *IEEE Trans. Antennas Propagat.*, vol. 45, pp. 98-106, Jan. 1997.

[6] C. Yang, B. Wu, and C. Ko, "A ray-tracing method for modeling indoor wave propagation and penetration," *IEEE Trans. Antennas Propagat.*, vol. 46, pp. 907-919, June 1998.

[7] H. Suzuki and A. S. Mohan, "Ray tube tracing method for predicting indoor channel characteristic map," *Electron. Lett.*, vol. 33, no. 17, pp. 1495-1496, 1997.

[8] C. Saeidi, F. Hodjatkashani, and A. Fard, "New tube-based shooting and bouncing ray tracing method," *Proc. IEEE ATC*, Hai Phong, Vietnam, pp. 269-273, Oct. 12-14, 2009.

[9] A. Capozzoli, O. Kilic, C. Curcio, and A. Liseno, "The success of GPU computing in applied electromagnetics," *Applied Computational Electromagnetics Society Express Journal*, vol. 1, no. 4, pp. 113-116, Apr. 2016.

[10] N. A. Carr, J. D. Hall, and J. C. Hart, "The ray engine," in *Proc. Graphics Hardware'02*, pp. 37-46, Sep. 2002.

[11] Y. Tao, H. Lin, and H. Bao, "GPU-based shooting and bouncing ray method for fast RCS prediction," *IEEE Trans. Antennas Propagat.*, vol. 58, no. 2, pp. 494-502, Feb. 2010.

[12] H. Meng and J. Jin, "Acceleration of the dual-field domain decomposition algorithm using MPI–CUDA on large-scale computing systems," *IEEE Trans. Antennas Propagat.*, vol. 62, no. 9, pp. 4706-4715, Sep. 2014.

[13] K. Wang and Z. Shen, "A GPU-based parallel genetic algorithm for generating daily activity plans," *IEEE Trans. on Intelligent Transportation Systems*, vol. 13, no. 3, pp. 1474-1480, Sep. 2012.

[14] Z. Shen, K. Wang, and F.-H. Zhu, "Agent-based traffic simulation and traffic signal timing optimization with GPU," in *Proc. 14th Int. IEEE Conf.*

Intell. Transp. Syst., pp. 145-150, 2011.

[15] G. Cramer, "Introduction à l'Analyse des lignes Courbes algébriques," (in French). *Geneva: Europeana.*, pp. 656-659, 1750. Retrieved 2012-05-18.

Dan Shi received her Ph.D. degree in Electronic Engineering from Beijing University of Posts and Telecommunications in Beijing, China in 2008. Now she is an Associate Professor in Beijing University of Posts and Telecommunications. Her research interests include electromagnetic compatibility, electromagnetic environment, and electromagnetic computation. She is Chair of IEEE EMC Beijing chapter, Vice Chair of URSI E Commission in China, and General Secretary of EMC section of China Institute of Electronics.

Xiaohe Tang received his Bachelor degree in Telecommunication Engineering from University of Shanghai for Science and Technology in Shanghai, China in 2015. Now he is studying for Master degree in Beijing University of Posts and Telecommunications in Beijing, China. His research interests include electromagnetic compatibility and electromagnetic environment.

Chu Wang received his Bachelor degree in Electronic and Information Engineering from Xidian University in Xi'an, China in 2015. Now he is studying for Master degree in Beijing University of Posts and Telecommunications in Beijing, China. His research interests include electromagnetic compatibility and electromagnetic environment.

Ming Zhao received his Bachelor degree in Computer Science and Technology Department from Beijing University of Posts and Telecommunications in Beijing, China in 2015. Now he is studying for Master degree in Beijing University of Posts and Telecommunications in Beijing, China. His research interests include electromagnetic compatibility and electromagnetic environment.

Yougang Gao received his B.S. degree in Electrical Engineering from National Wuhan University, China in 1950. He was a Visiting Scholar in Moscow Technical University of Communication and Information in Russia from 1957 to 1959. He is now a Professor and Ph.D. Supervisor in Beijing University of Posts and Telecommunications, China. He has been an Academician of International Information Academy of UN since 1994. He was once the Chairman of IEEE Beijing EMC Chapter and Chairman of China National E-Commission for URSI. He became an EMP Fellow of US Summa Foundation since 2010.

An Optimized Microwave Absorber Geometry Based on Wedge Absorber

Ibrahim Catalkaya [1] and Sedef Kent [2]

[1] Informatics Institute
Istanbul Technical University, Istanbul, 34469, Turkey
catalkaya@itu.edu.tr

[2] Department of Electronics and Communications Engineering
Istanbul Technical University, Istanbul, 34469, Turkey
kents@itu.edu.tr

Abstract ─ Low reflectivity of microwave absorbers is important to improve the performance of anechoic chamber measurements. The shape of the absorber as well as the material used are among the main components to provide desired low reflection performance. Pyramidal and wedge-shaped absorbers are two of the most well-known microwave absorber types. We discuss the effect of a convex shape on reflection performance of microwave absorbers and show that convex shape structure has significantly performance by absorbing most of the electromagnetic energy of the incident wave. We used a concavity theorem based design method to obtain a function for a convex shape. Absorbing structures have been analyzed by using the periodic moment method (PMM). An optimization method is employed to find coefficients of the convex function, which provides better absorption performance than the wedge type absorber. Reflection performances of the wedge and convex absorbers for the 2-12 GHz frequency band are compared. Their reflection performances at 2 GHz for different angles of incidence are presented. An important implication of this study is that the alternative absorber shapes other than the wedge shape are demonstrated by using simple mathematical methods to have the optimal reflection characteristics.

Index Terms ─ Anechoic chamber, electromagnetic scattering, electromagnetic wave absorption, microwave absorber, periodic moment method, periodic structures wedge diffraction.

I. INTRODUCTION

Unwanted or stray electromagnetic signal radiation such as electromagnetic interference (EMI), which usually radiate from electronic devices, can be a serious threat to living beings and cause faults on other electronics devices located nearby when radiation is strong [1-3]. Therefore, detection of them is very important. Microwave absorbers are used to eliminate these signals in microwave applications [4]. Many electronic systems are evaluated by using absorbers [5]. They are essential components for performing electromagnetic compatibility (EMC), EMI, radar cross section and antenna radiation pattern measurements accurately in a chamber instead of open field [1,4,6-10]. This chamber is called an "anechoic chamber" and is used to simulate a free space environment [4,11]. Microwave absorbers have dielectric or magnetic losses to absorb electromagnetic waves. The absorption capability of an absorber is depended on permittivity and permeability properties of the absorber material [12]. Absorbed electromagnetic waves are attenuated and their energy transformed into heat energy [4,13]. The two main categories of absorbers according to the working mechanism are resonating and graded (non-resonating) absorber structures [14]. Absorbers are used inside anechoic chamber surfaces (wall, ceiling, floor) to minimize reflection of incident electromagnetic waves and to perform measurements [14-18]. Absorbers having low reflectivity are preferable to trap most of the incident electromagnetic waves. Thus, almost perfect free space conditions are obtained in a chamber [6,19]. Various factors such as the electrical properties of the absorber material have an essential role in absorption performance of microwave absorbers [16]. The relative permittivity (dielectric constant) of the material used in an absorber is one of the most important factors [20]. It is a measure of the electrostatic energy stored in the material and affects the propagation speed of electromagnetic wave in the material [15,21].

The shape of the absorber used in the chamber also has significant importance on absorption performance in addition to other factors [22]. There are many types of absorber having different shapes, such as pyramidal, wedge, convoluted, among many others. The wedge-shaped absorber is one of the most well-known type which is also commonly used for EMC/EMI measurements [23,24]. Its wedge shape provides a suitable impedance match from free space to the base of the absorber [16].

Gradually impedance transition acts as an impedance matching network in order to have minimum amount of reflected EM wave [25]. On the other hand, while wedges are larger compared to a wavelength, incident EM waves are reflected numerous times between the sides of adjacent wedges before being reflected back [16]. Thus, a significant portion of its energy is absorbed upon each reflection due to the wedge-shape [26]. At higher frequencies, diffraction due to edges of wedge absorber contribute electric field significantly, which effects absorption performance of the absorber [27]. Therefore, numerical analysis of such structures need to take diffraction into account and Method of Moments (MoM) is one of techniques that can effectively incorporate such effects as well [28-30].

Here, we discuss obtaining an absorber shape by using a methodology that provides better impedance matching. Alternatively, obtaining a shape that will provide many bounces of an EM wave between sides of wedges before reflecting back.

Impedance transition of the wedge-shape absorber varies linearly from free space to the base of the absorber. For better impedance transition and multiple reflections between the sides of wedges, increasing of height of the wedge absorber is required. However, absorber height limits usable measurement space of the chamber and restricts usage of absorbers in small and semi-anechoic chambers [31,32]. Increasing available measurement space of the anechoic chamber is possible by using different absorber shapes that have the same or better absorption performance with lower height. Using nonlinear (curved) absorber shapes instead of a wedge type helps to improve the performance of the EMI/EMC measurements and available space in the chamber [32]. In addition, nonlinear absorber shapes provide smoother nonlinear impedance transition and/or many more reflections between the wedge sides [32].

Within this framework, the contribution of this study is proposing a method to obtain surface functions for absorbers that have better absorption performance than a wedge-shape absorber. Scattered electric fields from absorber structures have been analyzed by using the PMM. Reflection values of the plane electromagnetic wave that is E-field polarized along the axes of the absorber structure (TM case) are calculated. Since the TM case reflection performances are worse than the TE case performances, the scope of the study is limited for the TM case only [27].

Organization of the paper is as follows: Analyzing periodic absorber structures by using PMM is briefly explained to provide a background, followed by a discussion of the reflection performance and impedance transition relation. Then, a general method is proposed to obtain surface functions of the periodic structure by using the concavity theorem. Obtaining second order convex polynomial functions is demonstrated as a simple example. Numerical results of the wedge and convex absorber structures are presented in the results section, and finally conclusions given in the following section.

II. METHODS

A. Analyzing periodic absorber structures

Reflection performances of periodic absorber structures illuminated by a plane wave can be obtained by employing the PMM. Assuming that a TM polarized plane electromagnetic wave which has $e^{j\omega t}$ time dependency is incident upon singly-periodic structure having a period "L". Spectral domain expression of scattered E-field from structure is given by a well-known equation [33]:

$$E^s(x, y) = -(j\frac{k^2}{2L}) \sum_{p=-\infty}^{\infty} \iint (\varepsilon_r - 1)E_0(x', y') \frac{e^{-j(x-x')\beta_{1p}} . e^{-j|y-y'|\gamma_{1p}}}{\gamma_{1p}} dx'dy', \tag{1}$$

where

$$\beta_1 = ks_x, \ \beta_{1p} = \beta_1 + p\frac{2\pi}{L}, \ \gamma_{1p} = \sqrt{k^2 - \beta_{1p}^2}. \tag{2}$$

Since the vector sum of the scattered and incident electric field vectors is equal to the total electric field at any point as given in expression (3), the scattered field can be calculated by using PMM:

$$E = E^i + E^s. \tag{3}$$

PMM is based on dividing a cross section of the reference element into small size cells and calculating the scattered field by solving linear independent algebraic equations. The size of cells is selected in order to be small enough to consider dielectric constant and electric field density in each cell to be constant. A detailed explanation of the PMM is given in study [32].

MATLAB code is developed based on PMM in order to obtain reflection performances. Since MATLAB performs vector and matrix operations efficiently, complex matrix operations are calculated rapidly.

B. Reflection performance and impedance transition relation

Microwave absorbers need a smooth transition from air into the absorber in order to enhance impedance matching and complete absorption of the wave inside the absorber in order to achieve the desired low reflectivity properties [34,35]. Wedge or pyramidal-shaped absorbers have linear surfaces and they have good reflection performances because of linear impedance matching between air and absorber. Reflection performances of absorbers that have non-linear surfaces and impedance matching properties are different. Comparison of the reflection performances of the absorbers that have wedge, concave and convex surfaces are shown in Fig. 1 to specify the differences between them. The reflection performance of a wedge-shaped absorber is better than a concave-shaped one, and a convex-shaped absorber has the best reflection performance. A convex-shaped

absorber also has smoother impedance transition than both of concave-shaped and wedge-shaped absorbers. It is possible to obtain better impedance transitions by changing parameters of the related convex surface function such as polynomial functions, power function, exponential function etc.
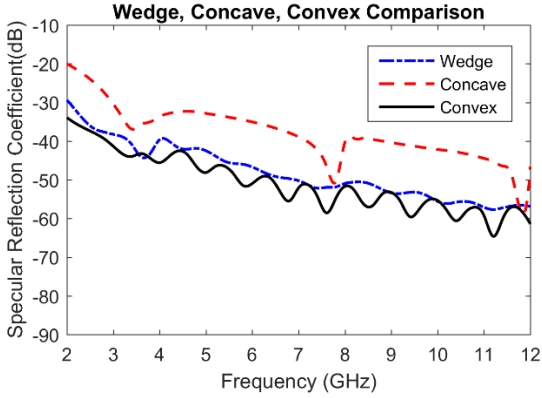

Fig. 1. Comparison of the reflection performances of absorbers that have wedge, concave and convex surfaces.

C. Design of convex shape 1-D microwave absorber function

Assume that the cross-section of the reference element of any lossy structure at the origin of the x-y plane, which has period "L". It consists of two symmetrical half parts in the interval $[-L/2,L/2]$. Finding the function for the half in the interval $[0,L/2]$ as a function of "x" defines the symmetrical half of the reference element in the interval $[-L/2,0]$.

Any function $f(x)$, which has a second derivative at each point in the interval $[0,L/2]$ and meets the $f'''(x)>0$ condition in this interval, is a convex (or concave upward) function according to the concavity theorem. Boundary values of the function are $f(0)=h$ and $(L/2)\geq0$. Where "h" is height of the reference element. Several convex functions such as polynomial functions, power function, exponential function etc... could be observed to satisfy conditions of the concavity theorem. Second order convex polynomial functions, as an example, are one of the simplest such functions for which determine coefficients.

A second order convex polynomial function $f(x)$ which has a constant positive second derivative value, $f'''(x)=a$ in the interval $[0,L/2]$ is shown in the expression below:

$$f(x) = \frac{a}{2}x^2 + bx + h. \qquad (4)$$

A convex function with a local minimum point outside the interval $[0,L/2]$, is shown in expression (5) and satisfies the $f(0)=h$ and $f(L/2)=0$ boundary conditions. It is a decreasing function. The condition for the first order derivative at the point $(L/2,0)$ is $-2h/L\leq f'(L/2)\leq0$. Thus, the condition for "a" values is $0\leq a\leq 8h/L^2$,

$$f(x) = \frac{a}{2}x^2 + \left(-\frac{aL}{4} - \frac{2h}{L}\right)x + h. \qquad (5)$$

For a convex function, which has its local minimum point (x_m, y_m) inside the interval $[0,L/2]$, is shown in expression (6). It satisfies $f(x_m)=0$ and $f''(x_m)=0$ conditions. Thus, $a\geq8h/L^2$ for "a" values are obtained by using these conditions,

$$f(x) = \frac{a}{2}x^2 - \sqrt{2ah}x + h. \qquad (6)$$

Various convex periodic surface functions with different absorption performances satisfying the concavity theorem can be derived by using different second derivative functions.

D. Periodic structure based on second order convex polynomial function

Absorber structure configuration based on second order convex polynomial function is designed as an example by adding 2 inches of base thickness. Constrained nonlinear optimization method is used to obtain the "a" value indicated in expressions (5) and (6). Optimized convex functions provide the best reflection result. Reflection values of several frequencies along 2-12 GHz frequency band are calculated. Reflection values at these frequencies are limited to be better than a predetermined limit value. This limit value is determined to satisfy the stated condition. The average value of them is considered as the objective function for optimization.

The absorption performance of the structure with the obtained "a" value by using optimization as shown in the Fig. 2 (b).
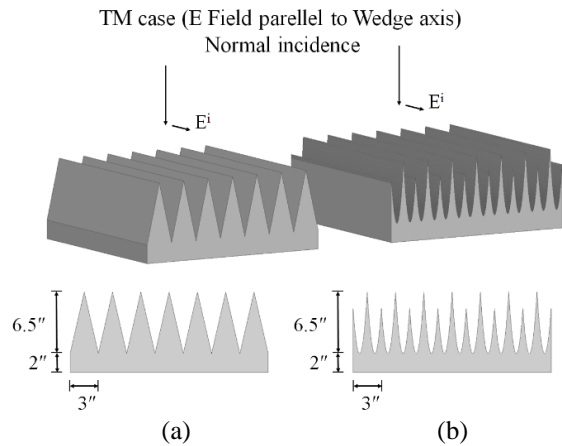

Fig. 2. Dimensions of the compared periodic structures: (a) wedge structure, and (b) second order convex polynomial function based structure.

The "a" value indicated in expressions (5) and (6) is obtained as $a=20.7439$ for the analyzed structure. The local minimum of the function is inside the interval $[0,L/2]$ which is seen in Fig. 2 (b). This "a" value provides the best absorption performance for TM mode plane electromagnetic wave normal incident case.

Total calculation time of the PMM is an important factor while performing optimization and reflection calculations. The Conjugate Gradients Squared Method with precondition is used in MATLAB PMM code to enhance calculation time while calculating matrix inverses.

III. RESULTS & DISCUSSION

Reflection coefficients of the wedge type and designed convex absorber structures are calculated by using PMM. Interpolation is used before plotting graphs of the reflection performances to obtain smooth curves. The base width of the periodic structures is three inches, base thickness is two inches and wedge height is 8.5 inches. The dielectric constant of the black wedge material shown in studies [27,32] has been used for PMM calculations.

Dimensions (base widths, base thicknesses and wedge heights) based on the black wedge absorber in studies [27,32] are used for analysis of the wedge type absorber in this study to validate developed MATLAB PMM code. The specular reflection coefficient versus frequency plot of the black wedge absorber shown in Fig. 73 on page 117 in study [27] is obtained with extended frequency band (2-12 GHz frequency band instead of 2-8 GHz). Same base widths, base thicknesses and wedge heights with the wedge type absorber are used for analysis of the designed absorber to compare their reflection performances.

Comparison of the reflection performances are shown in Fig. 3. Absorber structures are illuminated by normally incident TM mode plane electromagnetic wave at the 2-12 GHz frequency range with a step of 0.1 GHz. By comparing the wedge type and convex absorber structures, the results in the figure show a significant improvement in performance for the designed convex absorber structure relative to the wedge type. It has almost 17 dB better reflection performance, which is -46 dB, at 2 GHz. It also provides better reflection more than 14 dB at several frequencies such as 2.4 GHz, 6.6 GHz and 10 GHz. Its reflection values at 3.7 GHz, 8.1 GHz and 12 GHz frequencies are not more than reflection values of the wedge absorber.

It is clear that the proposed absorber has a sharper geometry than conventional wedge absorbers. It also has more edges. Therefore, edge diffraction has much more dominant effects on the absorption performance of the proposed absorber. On the other hand, for arbitrary shaped parametric surfaces, it is not straightforward to formulate absorption performance which includes diffraction effects. In this context, the basis of this research is optimizing absorption performance through incorporating diffraction effects numerically.

Figure 4 shows the reflection coefficient versus the angle of incidence for the wedge type and convex absorber structures at 2 GHz. The convex absorber structure

provides reflection performance of -46 dB for normal incidence case. Its performance is almost 17 dB better than the wedge absorber, which has approximate -29 dB reflection performance. The convex absorber structure also provides better reflection performance values for the oblique incidence case than the wedge type. For a 70 degrees angle of incidence, while the wedge type provides approximately a -7 dB reflection value, the convex absorber structure gives -9.3 dB reflection performances. It has almost a 2 dB better value than the wedge type. The convex absorber has almost a 10 dB better reflection performance for angles of incidence of less than 30 degrees.
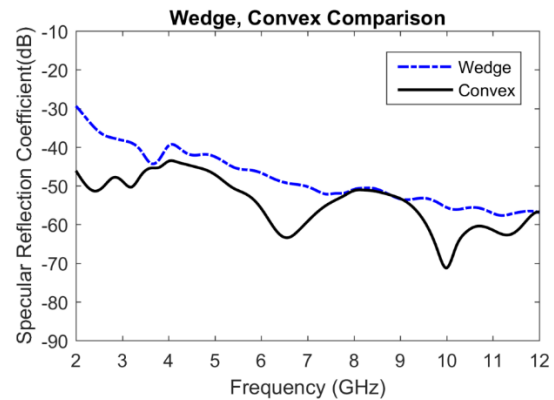

Fig. 3. Comparison between the wedge type and convex absorber structures for the 2-12 GHz frequency range.
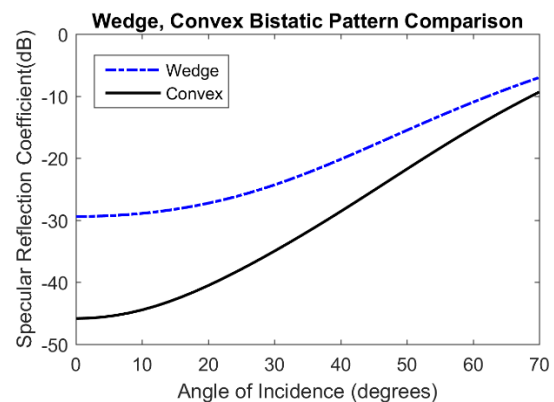

Fig. 4. Comparison of the bistatic pattern performances for the wedge type and convex absorber structure.

IV. SUMMARY & CONCLUSIONS

A design method for obtaining absorber geometry for better reflection performance, among the wedge types has been explained in this study. The concavity theorem is used to obtain convex function for determining absorber geometry. Absorber structure configuration based on second order convex polynomial function is designed as an example. The range of the unknown

parameters of the function are calculated by using boundary conditions. Optimization is used to obtain specific values of the parameters of the function which give optimum results. By considering the optimized parameters of the function associated with the boundary conditions of the periodic structure, absorption performance values for the total frequency range have been calculated. Also, reflection values versus angle of incidence are obtained. Comparison of the reflection performances of the absorber structures have been presented.

A designed convex absorber structure has significantly better absorption performance and it is an ideal absorber to enhance measurements at low signal levels. It can be used to increase the available measurement space of the chamber. For a wide frequency range, a designed absorber structure has better performance than the wedge type for both, the normal and oblique incidence cases.

In terms of manufacturing of absorbers, non-wedge shape of absorbers as design in this study can be produced with CNC controlled foam cutting equipment for smaller quantities. They can be produced with mould fabrication for mass production. However, a single cut through a foam block with foam cutting technique and obtaining two similar absorber panel to maximize factory production cannot be performed because of non-complementary geometry of non-wedge shapes. Thus, small amount of unused material is wasted during production.

The results of experimental works based on theoretical studies presented in this work are planned to be verified as future studies. Calculation of unknown parameters of the higher order functions and design of absorber structures will be discussed in a future study as well.

REFERENCES

[1] B. K. Chung, *EMI/EMC Chamber Design, Measurement, and Instrument*. Handbook of Antenna Technologies, Z. N. Chen, Ed., Singapore: Springer Singapore, pp. 1-23, 2014.

[2] K. Hirose, "Electromagnetic wave absorber," *US Patent 9263802*, 2016.

[3] D. Wan, S. W. Bie, J. Zhou, H. Xu, Y. Xu, and J. Jiang, "A thin and broadband microwave absorber based on magnetic sheets and resistive FSS," *Progress In Electromagnetics Research C*, vol. 56, pp. 93-100, 2015.

[4] L. Zahid, M. F. A. Malek, C. E. Meng, L. W. Wen, L. Y. Seng, A. Z. Abdullah, N. S. M. Noorpi, N. M. Mokhtar, and M. A. Jusoh, "Performance of sugarcane bagasse and rubber tire dust microwave absorber in ku band frequency," *Theory and Applications of Applied Electromagnetics*, pp. 207-214, Springer, 2015.

[5] L. Pometcu, A. Sharaiha, R. Benzerga, and P. Pouliguen, "Straight wedge absorber geometry optimization for normal and oblique incidence," *Antennas and Propagation Conference (LAPC), 2014, Loughborough*, pp. 633-636, 2014.

[6] G. Dash and L. Ampyx, "How rf anechoic chambers work," *Glen Dash at alum. Mit. edu, 2005 Ampyx LLC*, 2005.

[7] C. L. Holloway and E. F. Kuester, "A low-frequency model for wedge or pyramid absorber arrays-II: Computed and measured results," *IEEE Transactions on Electromagnetic Compatibility*, vol. 36, pp. 307-313, Nov. 1994.

[8] E. F. Kuester and C. L. Holloway, "A low-frequency model for wedge or pyramid absorber arrays-I: Theory," *IEEE Transactions on Electromagnetic Compatibility*, vol. 36, pp. 300-306, Nov. 1994.

[9] H. Nornikman, P. J. Soh, A. A. H. Azremi, and M. S. Anuar, "Performance simulation of pyramidal and wedge microwave absorbers," *2009 Third Asia International Conference on Modelling & Simulation*, vols. 1 and 2, pp. 649-654, 2009.

[10] X. C. Tong, *Advanced Materials and Design for Electromagnetic Interference Shielding*. CRC Press, 2016.

[11] W. Tang, R. Yang, and Y. Hao, "Compression of a pyramidal absorber using multiple discrete coordinate transformation," *Optics Express*, vol. 22, pp. 9033-9047, 2014.

[12] T. Shami, H. B. Baskey, A. K. Dixit, R. Kumar, and S. Kumar, "Multicomponent lightweight ultra wide band electromagnetic absorbers for X band frequency region," *2015 Communication, Control and Intelligent Systems (CCIS)*, pp. 73-76, 2015.

[13] H. Abdullah, L. M. Kasim, M. N. Taib, N. M. Noor, N. A. Ismail, A. Ahmad, N. M. Kasim, N. R. Ahmad, and A. R. Razali, "Multilayer performance of green biomass coated pyramidal hollow microwave absorber," *Advanced Computer and Communication Engineering Technology*, pp. 1175-1185, Springer, 2016.

[14] A. Fallahi and A. Enayati, "Modeling pyramidal absorbers using the fourier modal method and the mode matching technique," *IEEE Transactions on Electromagnetic Compatibility*, vol. 58, pp. 820-827, June 2016.

[15] T. Aoyagi, H. Kurihara, K. Takizawa, and Y. Hirai, "Effects of incident directions on reflection coefficients of pyramidal electromagnetic wave absorber," *2014 International Symposium on Electromagnetic Compatibility, Tokyo (EMC'14/Tokyo)*,

pp. 278-281, 2014.

[16] A. Azman, A. Salleh, M. A. Aziz, M. Suaidi, and F. Malek, "Study of simulation design pyramidal microwave absorber with different relative permittivity," *Journal of Convergence Information Technology*, vol. 10, p. 20, 2015.

[17] I. Catalkaya and S. Kent, "Analysis of multiple wedges electromagnetic wave absorbers," *Progress In Electromagnetics Research M*, vol. 26, pp. 1-9, 2012.

[18] M. F. B. A. Malek, E. M. Cheng, O. Nadiah, H. Nornikman, M. Ahmed, M. Z. A. Abdul Aziz, A. R. Othman, P. J. Soh, A. A. A.-H. Azremi, A. Hasnain, and M. N. Taib, "Rubber tire dust-rice husk pyramidal microwave absorber," *Progress in Electromagnetics Research-PIER*, vol. 117, pp. 449-477, 2011.

[19] B. K. Chung and H. T. Chuah, "Modeling of RF absorber for application in the design of anechoic chamber," *Journal of Electromagnetic Waves and Applications*, vol. 18, pp. 81-82, 2004.

[20] T. Saitoh, Y. Hirai, H. Kurihara, and M. Yanagawa, "Electromagnetic wave absorber and electromagnetic wave anechoic room," *US Patent 20150340766*, 2015.

[21] A. Enayati and A. Fallahi, "Pyramidal absorbers investigation of higher orders of diffraction," *ATMS 2015*, Bangalore, India, 2015.

[22] H. Nornikman, F. Malek, P. J. Soh, A. A. H. Azremi, F. H. Wee, and A. Hasnain, "Parametric studies of the pyramidal microwave absorber using rice husk," *Progress in Electromagnetics Research-Pier*, vol. 104, pp. 145-166, 2010.

[23] J. Lee, M. Yoo, and S. Lim, "A study of ultra-thin single layer frequency selective surface microwave absorbers with three different bandwidths using double resonance," *IEEE Transactions on Antennas and Propagation*, vol. 63, pp. 221-230, Jan. 2015.

[24] H. Nornikman, P. J. Soh, A. A. H. Azremi, F. H. Wee, and M. F. Malek, "Investigation of an agricultural waste as an alternative material for microwave absorbers," *PIERS 2009 Moscow Vols. I and II, Proceedings*, pp. 1287-1291, 2009.

[25] H. Severin, "Nonreflecting absorbers for microwave radiation," *IRE Transactions on Antennas and Propagation*, vol. 4, pp. 385-392, 1956.

[26] W. Emerson, "Electromagnetic wave absorbers and anechoic chambers through the years," *IEEE Transactions on Antennas and Propagation*, vol. 21, pp. 484-490, 1973.

[27] C. F. Yang and W. D. Burnside, "Periodic moment method solutions for scattering from arrays of lossy dielectric bodies," *Ph.D. Dissertation*, Ohio State University, 1992.

[28] G. Apaydin and L. Sevgi, "A novel wedge diffraction modeling using method of moments (MoM)," *Applied Computational Electromagnetics Society Journal*, vol. 30, pp. 1053-1058, Oct. 2015.

[29] O. Ozgun and L. Sevgi, "Comparative study of analytical and numerical techniques in modeling electromagnetic scattering from single and double knife-edge in 2d ground wave propagation problems," *Applied Computational Electromagnetics Society Journal*, vol. 27, pp. 376-388, May 2012.

[30] M. A. Uslu and L. Sevgi, "Matlab-based virtual wedge scattering tool for the comparison of high frequency asymptotics and FDTD method," *Applied Computational Electromagnetics Society Journal*, vol. 27, pp. 697-705, Sep. 2012.

[31] M. J. Park and S. S. Kim, "Design of wide bandwidth pyramidal microwave absorbers using ferrite composites with broad magnetic loss spectra," *Electronic Materials Letters*, vol. 12, pp. 610-614, Sep. 2016.

[32] C. F. Yang, W. D. Burnside, and R. C. Rudduck, "A periodic moment method solution for TM scattering from lossy dielectric bodies with application to wedge absorber," *IEEE Transactions on Antennas and Propagation*, vol. 40, pp. 652-660, June 1992.

[33] J. Richmond, "Scattering by a dielectric cylinder of arbitrary cross section shape," *IEEE Transactions on Antennas and Propagation*, vol. 13, pp. 334-341, 1965.

[34] R. C. Rudduck, W. D. Burnside, and C. F. Yang, "Serrated electromagnetic absorber," *US Patent 5208599*, 1993.

[35] K. Walther, "Reflection factor of gradual-transition absorbers for electromagnetic and acoustic waves," *IRE Transactions on Antennas and Propagation*, vol. 8, pp. 608-621, 1960.

Ibrahim Catalkaya received the B.E. degree in Electronics and Communication Engineering from the Istanbul Technical University (ITU), Istanbul, Turkey, in 1992, and the M.S. degree in Engineering Management from the Marmara University, Istanbul, Turkey, in 2005. He joined Ericsson, Turkey, in 1995. He has held Lecturing position at the ITU, Istanbul, Turkey, in 2006.

He has been involved with many communication infrastructure projects since 1993 in Turkey. His research interests cover the numerical methods in electromagnetics.

Sedef Kent was born in Istanbul, Turkey. She received the B.E., M.E., and Ph.D. degrees from Istanbul Technical University (ITU), Turkey, in 1982, 1984, and 1990, respectively. Since 1984, she has been with the Department of Communication and Electronics, Faculty of Electrical-Electronics Engineering, ITU, where she is currently a full time Professor. Her main areas of research interest are microwave circuit design, electromagnetics and inverse problems, remote sensing and SAR systems.

A Novel AGEI Solution of Parabolic Equation for EM Scattering Problems

Shifei Tao

Department of Electrical and Computer Engineering
Northeastern University, Boston, 02115, USA
s.tao@neu.edu

Abstract ─ Parabolic equation (PE) has been widely used for EM propagating and scattering problems for its high efficiency. By using the finite differential (FD) method, the calculation can be taken in a series of transverse planes in a marching manner. In this paper, the alternating group explicit iterative (AGEI) method is applied to solve the alternating direction implicit based parabolic equation (ADI-PE). As a result, the CPU time can be further saved when compared with the CN-PE and ADI-PE methods. Numerical results are shown for demonstrating the accuracy and efficiency.

Index Terms ─ Alternating group explicit iterative (AGEI) method, electromagnetic scattering, parabolic equation.

I. INTRODUCTION

The rigorous numerical methods, such as the Finite Difference Time Domain (FDTD), the Method of Moment (MoM) and the Finite Element Method (FEM) are widely used for electromagnetic analysis. However, a huge number of computational resources are needed with the number of unknowns increasing, thus the efficiency will become low. On the other hand, the high frequency methods have low accuracy with few computational resources. The parabolic equation (PE) [1-11] is an approximation of the wave equation, which can give encouraging accuracy with limited computational resources. Therefore, the PE method takes a bridge between rigorous numerical methods and high frequency methods.

By using the finite differential (FD) method along the paraxial direction, the calculation can be taken plane by plane. As a result, the computational resources can be saved largely. There are several methods that have been used to solve the parabolic equation, such as the Split-Step Fourier Transform (SSFT) [1], the Crank-Nicolson (CN) [2-4], the Alternate Direction Implicit (ADI) [5-7], and the Alternate Group Explicit (AGE) [8-9, 20]. Moreover, several kinds of high-order approximations have been introduced to get the wide-angle prosperities [10-11, 19]. Furthermore, some other numerical algorithms, including the Method of Moment

(MoM) [12-13], the Geometrical Theory of Diffraction (GTD) [14], and other techniques [15-16] are combined with the PE method, which broaden the application of the PE method. It should be noted here that the PE can only model the object does not undergo large changes in direction. Moreover, the objects, which are small compared to the wavelength, cannot be simulated by PE method. Since the creeping waves cannot be captured by the PE method.

The implicit FD methods are widely used for their simplicity, stability and efficiency [2-7]. The CN scheme is one of the most popular implicit FD methods [2-4]. Nevertheless, a huge computer resource is required with the electrical size of the targets increasing. Then the ADI method is proposed to accelerate the calculation of the PE method [8-9]. By using the ADI scheme, the fields in any transverse plane can be calculated line by line, which reduce the computation complexity by solving the unknowns in one dimension. On the other hand, the explicit FD methods can achieve high computational efficiency, but may result in instability. Therefore, the development of methods with both the high efficiency and stability has a practical significance.

In this paper, the ADI-based parabolic equations are derived firstly. In this way, a series of tridiagonal matrix equations are needed to be solved in each transverse plane. Then the alternating group explicit iterative (AGEI) method [17-18] is used to solve these equations. As a result, all the unknown fields in each transverse plane can be computed explicitly without solving any matrix equation. Therefore, the CPU time can be saved significantly than the traditional ADI-PE method. Several numerical examples are given to demonstrate the accuracy and efficiency of the proposed AGEI-PE method.

II. THEORY AND FORMULATIONS

A. ADI-PE method

Considering a PEC object illuminated by a plane wave in free space, a reduced function associated with a field component is introduced as follows:

$$u(x, y, z) = e^{-ikx} E(x, y, z), \tag{1}$$

where k is the wave number.

The standard forward parabolic equation can be obtained via substituting Equation (1) into the wave equation and factorization,

$$\frac{\partial u}{\partial x} = -ik(1 - \sqrt{Q})u , \qquad (2)$$

where Q is the pseudo-differential operator, which can be expressed as:

$$Q = \frac{1}{k^2}\left(\frac{\partial^2}{\partial y^2} + \frac{\partial^2}{\partial z^2}\right) + n^2 . \qquad (3)$$

Equation (2) is one order differential along the x axis. The FD scheme along the paraxial direction can be easily applied, and the calculation can be taken plane by plane.

The ADI-PE can be derived directly from the CN-PE as indicated in [5-6]. The matrix form of the ADI-PE is:

$$\left[-\frac{ir_y}{4k} \quad 1+\frac{ir_y}{2k} \quad -\frac{ir_y}{4k}\right]\begin{bmatrix} u_{j-1,k}^{n+1/2} \\ u_{j,k}^{n+1/2} \\ u_{j+1,k}^{n+1/2} \end{bmatrix} =$$

$$\left[\frac{ir_z}{4k} \quad 1-\frac{ir_z}{2k} \quad \frac{ir_z}{4k}\right]\begin{bmatrix} u_{j,k-1}^{n} \\ u_{j,k}^{n} \\ u_{j,k+1}^{n} \end{bmatrix} , \qquad (4)$$

$$\left[-\frac{ir_z}{4k} \quad 1+\frac{ir_z}{2k} \quad -\frac{ir_z}{4k}\right]\begin{bmatrix} u_{j,k-1}^{n+1} \\ u_{j,k}^{n+1} \\ u_{j,k+1}^{n+1} \end{bmatrix} =$$

$$\left[\frac{ir_y}{4k} \quad 1-\frac{ir_y}{2k} \quad \frac{ir_y}{4k}\right]\begin{bmatrix} u_{j-1,k}^{n+1/2} \\ u_{j,k}^{n+1/2} \\ u_{j+1,k}^{n+1/2} \end{bmatrix} , \qquad (5)$$

where $r_y = \Delta x / \Delta y^2$, $r_z = \Delta x / \Delta z^2$, $u_{j,k}^n$ denotes the reduced scattered field at the point of $(n\Delta x, j\Delta y, k\Delta z)$.

As a result, there is an intermediate plane introduced between the n th and n+1 th planes with less unknowns. Moreover the scattered fields can be calculated line by line. Finally, a series of tridiagonal matrices are to be solved by the ADI-PE method in each transverse plane.

B. AGEI solution of ADI-PE

Both the Equations (4) and (5) are tridiagonal matrix equations. Therefore, they can be solved by using the AGEI scheme. Suppose the impedance matrix can be written as:

$$A = \begin{bmatrix} a & b & & & & \\ b & a & b & & & \\ & b & a & b & & \\ & & & \ddots & & \\ & & & b & a & b \\ & & & & b & a \end{bmatrix} . \qquad (6)$$

It should be noted that $a=1+\dfrac{ir_y}{2k}$, $b=-\dfrac{ir_y}{4k}$ for Equation (4), and $a=1+\dfrac{ir_z}{2k}$, $b=-\dfrac{ir_z}{4k}$ for Equation (5). Then the impedance matrix is split into two parts, which can be expressed as:

$$A = G_1 + G_2$$

$$= \begin{bmatrix} \frac{a}{2} & & & & \\ & \frac{a}{2} & b & & \\ & b & \frac{a}{2} & & \\ & & & \ddots & \\ & & & & \frac{a}{2} & b \\ & & & & b & \frac{a}{2} \end{bmatrix} + \begin{bmatrix} \frac{a}{2} & b & & & \\ b & \frac{a}{2} & & & \\ & & \ddots & & \\ & & & \frac{a}{2} & b \\ & & & b & \frac{a}{2} \\ & & & & & \frac{a}{2} \end{bmatrix} , \qquad (7)$$

Then the impedance matrix equation to be solved can be simplified as:

$$Au = (G_1 + G_2)u = f . \qquad (8)$$

Furthermore, the following equivalent matrix equations can be obtained:

$$(\lambda I + G_1)u = (\lambda I - G_2)u + f , \qquad (9)$$

or

$$(\lambda I + G_2)u = (\lambda I - G_1)u + f . \qquad (10)$$

At last, an alternating group explicit iterative (AGEI) method is applied to (8),

$$\begin{cases} (\lambda I + G_1)v^{k+1} = (\lambda I - G_2)u^k + f \\ (\lambda I + G_2)u^{k+1} = (\lambda I - G_1)v^{k+1} + f \end{cases} , \qquad (11)$$

where $k = 0,1,2...$, λ is the Peaceman-Rachford constant.

More specifically, the iterative method can be rewritten as:

$$\begin{cases} v^{k+1} = (\lambda I + G_1)^{-1}\left[(\lambda I - G_2)u^k + f\right] \\ u^{k+1} = (\lambda I + G_2)^{-1}\left[(\lambda I - G_1)v^{k+1} + f\right] \end{cases} . \qquad (12)$$

Substitute v^{k+1} into the second matrix equation,

then the following result can be obtained:

$$u^{k+1} =$$

$$(\lambda I + G_2)^{-1}(\lambda I - G_1)(\lambda I + G_1)^{-1}(\lambda I - G_2)u^k + R$$
$$= (\lambda I + G_2)^{-1}(\lambda I - G_1)(\lambda I + G_1)^{-1}(\lambda I - G_2)u^k + \qquad (13)$$
$$[(\lambda I + G_2)^{-1}(\lambda I - G_1)(\lambda I + G_1)^{-1} + (\lambda I + G_2)^{-1}]f$$

For the first line of u^{k+1}, the calculation can be taken as:

$$u_1^{k+1} = t^2\left[(\lambda^2 - \frac{a^2}{4})^2 + b^2(b^2 + a\lambda - \frac{a^2}{2})\right]u_1^k$$
$$+ t^2\left(-2\lambda b(\lambda^2 - \frac{a^2}{4})\right)u_2^k + 2t^2\lambda b^2(\lambda - \frac{a}{2})u_3^k , \qquad (14)$$
$$- 2t^2\lambda b^3 u_4^k + r_1$$

where

$$r_1 = (\lambda - \frac{a}{2})[\left(\lambda + \frac{a}{2}\right)^2 - b^2]tf_1$$
$$- b(\lambda^2 - \frac{a^2}{4} + b^2)tf_2 + 2\lambda b^2 tf_3 \qquad (15)$$

$$t = \frac{1}{\left(\lambda + \frac{a}{2}\right)^2 - b^2} . \qquad (16)$$

For the second line of u^{k+1}, the calculation can be taken as:

$$u_2^{k+1} = (-b)\frac{2\lambda(\lambda^2 - \frac{a^2}{4})(\lambda + \frac{a}{2}) + 2ab^2\lambda}{\lambda + \frac{a}{2}}t^2 u_1^k$$

$$+ \frac{(\lambda - \frac{a}{2})[(\lambda + \frac{a}{2})^2[\lambda^2 - \frac{a^2}{4} + 2b^2] - b^2]}{\lambda + \frac{a}{2}}t^2 u_2^k , \qquad (17)$$

$$- 2\lambda b\left(\lambda^2 - \frac{a^2}{4}\right)t^2 u_3^k\, 2\lambda b^2\left(\lambda + \frac{a}{2}\right)t^2 u_4^k + r_2$$

where

$$r_2 = \left[(\lambda - \frac{a}{2})\frac{\left(\lambda + \frac{a}{2}\right)^2 - b^2}{\lambda + \frac{a}{2}}(-bt) - (\lambda - \frac{a}{2})\right]f_1$$

$$+ \left[(\lambda + \frac{a}{2})(\lambda^2 - \frac{a^2}{4} + b^2) - b\right]tf_2 \qquad . \qquad (18)$$

$$+ (\lambda + \frac{a}{2})(-2\lambda b)tf_3$$

Similarly, for $i=3, 5, 7, 9, \ldots$, the solution can be expressed as:

$$u_i^{k+1} = 2\lambda b^2 t^2\left(\lambda + \frac{a}{2}\right)u_{i-2}^k - 2\lambda bt^2\left(\lambda^2 - \frac{a^2}{4}\right)u_{i-1}^k$$

$$+ t^2(\lambda^2 - \frac{a^2}{4} + b^2)^2 u_i^k - 2\lambda bt^2(\lambda^2 - \frac{a^2}{4} + b^2)u_{i+1}^k , \qquad (19)$$

$$+ 2\lambda b^2 t^2(\lambda - \frac{a}{2})u_{i+2}^k + r_i$$

$$u_{i+1}^{k+1} = -2\lambda b^3 t^2 u_{i-2}^k - 2\lambda bt^2(\lambda^2 - \frac{a^2}{4} + b^2)u_{i-1}^k$$

$$+ (\lambda^2 - \frac{a^2}{4} + b^2)^2 t^2 u_i^k - 2t^2\lambda b\left(\lambda^2 - \frac{a^2}{4}\right)u_{i+1}^k , \qquad (20)$$

$$+ 2\lambda b^2 t^2\left(\lambda + \frac{a}{2}\right)u_{i+2}^k + r_{i+1}$$

where

$$r_i = (\lambda + \frac{a}{2})(-2\lambda bt)f_{i-2} + \left[(\lambda + \frac{a}{2})(\lambda^2 - \frac{a^2}{4} + b^2)\right]tf_{i-1}$$

$$- \left(b(\lambda^2 - \frac{a^2}{4} + b^2) - \lambda - \frac{a}{2}\right)tf_i + \left(2\lambda b^2 - b\right)tf_{i+1} \qquad , \qquad (21)$$

$$r_{i+1} = 2\lambda b^2 tf_{i-2} - \left[b(\lambda^2 - \frac{a^2}{4} + b^2) + (\lambda - \frac{a}{2})\right]tf_{i-1}$$

$$+ \left[(\lambda + \frac{a}{2})(\lambda^2 - \frac{a^2}{4} + b^2) - b\right]tf_i \qquad . \qquad (22)$$

$$+ (\lambda + \frac{a}{2})(-2\lambda b)tf_{i+1}$$

It should be noted that the Peaceman-Rachford constant is set to be 0.5 for all the numerical results.

C. Implementation aspects

The three scalar parabolic equations of x, y, z, directions are coupled through the inhomogeneous boundary conditions. For the conducting targets, the tangential component of the total field equals zero on the surface of the scattering target. Moreover, the divergence-free condition is used for the unicity [2]. In each transverse plane, the perfectly matched layer (PML) is introduced to truncate the computational domain. The computation begins before the scattering target and stops beyond it. Finally, the scattering properties can be obtained by applying the near-far field conversion. Furthermore, the full bistatic RCS result are calculated by several rotating PE runs.

Then the RCS in direction (θ, ϕ) along polarization t can be written as:

$$\sigma_t(\theta, \phi) =$$
$$\frac{k^2\cos^2\theta}{\pi}\left|\int_{-\infty}^{\infty}\int_{-\infty}^{\infty}ue^{ikx_0}\cdot te^{-ik\sin\theta(y\cos\phi + z\sin\phi)}dydz\right|^2 , \qquad (23)$$

where u is the reduced scattered fields in the last transverse plane for a specified frequency.

III. NUMERICAL RESULTS

At first, the electromagnetic scattering from a PEC cylinder with 5 m radius and 6 m height is considered at the frequency of 300 MHz. The paraxial direction is along the x axis and the incident angle is fixed at $\theta_{inc} = 90°$, $\phi_{inc} = 0°$. There are totally 60 transverse planes to be calculated with 150×150 nodes in each transverse plane. The range steps are set to be 0.1 m. As shown in Fig. 1, the bistatic RCS results are compared between the MoM accelerated by the multilevel fast multipole method (MLFMM) and the proposed AGEI-PE method. There is a good agreement between them. Moreover, as shown in Table 1, both the comparisons of both the memory requirement and the CPU time are made among the MoM, CN-PE, ADI-PE and AGEI-PE methods. It can be seen that higher efficiency can be achieved for the proposed AGEI-PE method when compared with other methods.
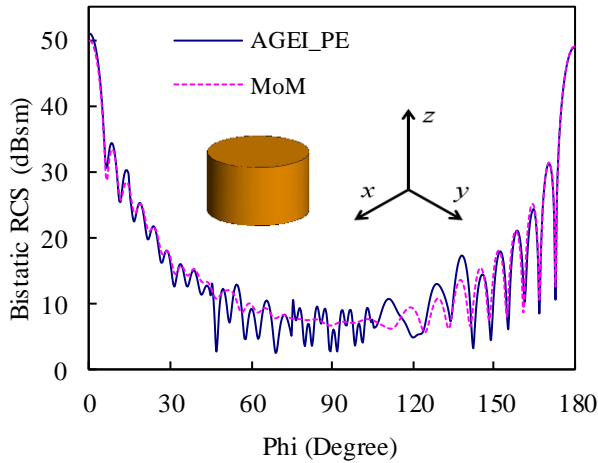

Fig. 1. Bistatic RCS result for the PEC cylinder.

Table 1: Comparisons of computational resources among the MoM, CN-PE, ADI-PE and AGEI-PE methods for the PEC cylinder

	Memory (MB)	CPU Time (s)
MoM	562	3958
CN-PE	515	475
ADI-PE	105	273
AGEI-PE	91	120

Secondly, the analysis is taken for a PEC block

at the frequency of 300 MHz with the length of 8 m. The incident angle is fixed at $\theta_{inc} = 90°$, $\phi_{inc} = 0°$. In this example, the range steps are chosen to be 0.1 m. As a result, there are 40 transverse planes to be calculated with 150×150 nodes in each transverse plane. As shown in Fig. 2, the bistatic RCS curves of the PEC block are compared between the MoM accelerated by MLFMM and the proposed AGEI-PE method. There is a good agreement between them. Additionally, as shown in Table 2, the computational resources are compared among the MoM, CN-PE, ADI-PE and AGEI-PE methods.
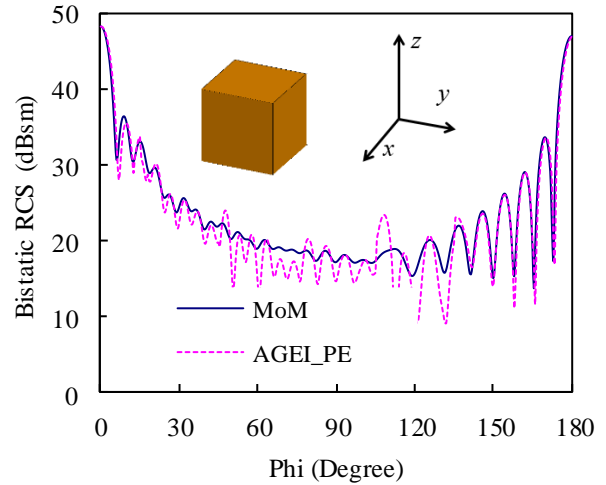

Fig. 2. Bistatic RCS result for the PEC block.

Table 2: Comparisons of computational resources among the MoM, CN-PE, ADI-PE and AGEI-PE methods for the PEC clock

	Memory (MB)	CPU Time (s)
MoM	667	7648
CN	559	586
ADI	127	348
AGEI	119	147

At last, a complicated model is considered, an aircraft at the frequency of 5 GHz. The incident angle is fixed at $\theta_{inc} = 90°$, $\phi_{inc} = 0°$. There are 167 transverse planes to be calculated with the range steps of 0.06 m and 100×100 nodes in each transverse plane. As shown in Fig. 3, the full bistatic RCS results are given. It can be found that the proposed AGEI-PE method can be used as an efficient tool to analyze the electromagnetic scattering from arbitrary structures.
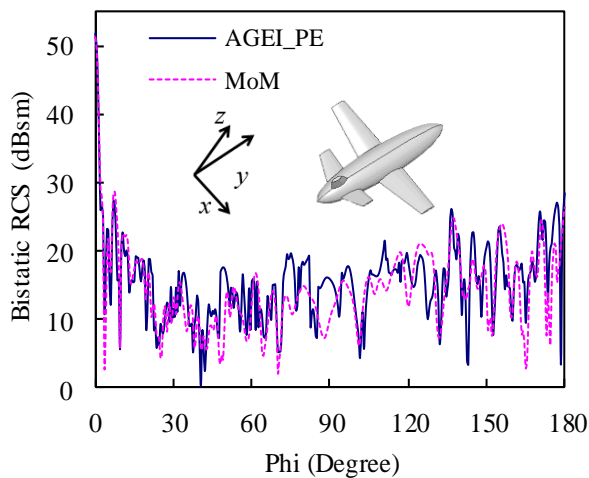
Fig. 3. Bistatic RCS result for the PEC aircraft.

IV. CONCLUSION

An AGEI solution of ADI-PE is proposed in the paper. By splitting the tridiagonal matrix into two parts and proper transformation, the matrix equations of ADI-PE method can be solved explicitly. Moreover, the proposed AGEI-PE method is easily to be paralleled. In this way, high computational efficiency can be achieved with encouraging accuracy. Numerical results are given to demonstrate the accuracy and efficiency of the proposed AGEI-PE scheme.

REFERENCES

[1] R. Janaswamy, "A curvilinear coordinate-based split-step parabolic equation method for propagation predictions over terrain," *IEEE Trans. Antennas and Propagation*, vol. 46, no. 7, pp. 1089-1098, 1998.

[2] A. A. Zaporozhets and M. F. Levy, "Bistatic RCS calculations with the vector parabolic equation method," *IEEE Trans. Antennas and Propagation*, vol. 47, no. 11, 1999.

[3] Z. He and R. S. Chen, "Fast analysis of wideband scattering from electrically large targets with time-domain parabolic equation method," *Computer Physics Communication*, vol. 200, pp. 139-146, 2016.

[4] M. F. Levy, "Parabolic equation methods for electromagnetic wave propagation," London: *The Institution of Electrical Engineers*, 2000.

[5] R. Martelly and R. Janaswamy, "Modeling radio transmission loss in curved, branched and rough-walled tunnels with the ADI-PE method," *IEEE Trans. Antennas and Propagation*, vol. 58, no. 6, pp. 2037-2045, 2010.

[6] Z. He, Z. H. Fan, D. Z. Ding, and R. S. Chen, "Efficient radar cross-section computation of electrically large targets with ADI-PE method," *Electronics Letters*, vol. 51, no. 4, pp. 360-362, 2015.

[7] Z. He, Z. H. Fan, D. Z. Ding, and R. S. Chen, "GPU-accelerated ADI-PE method for the analysis of EM scatterings," *Electronics Letters*, vol. 51, no. 21, pp. 1652-1654, 2015.

[8] D. J. Evans and A. R. B. Abdullah, "Group explicit method parabolic equations," *Inter. J. Computer Math.*, vol. 14, pp. 73-105, 1983.

[9] D. J. Evans and M. S. Sahimi, "The solution of nonlinear parabolic partial differential equations by the alternating group explicit (AGE) method," *Computer Methods in Applied Mechanics and Engineering*, vol. 84, no. 1, pp. 15-42, 2009.

[10] Z. He and R. S. Chen, "A wide-angle ADI-PE method for EM scattering from electrically large targets," *Electromagnetics*, vol. 36, iss. 2, pp. 94-101, 2016.

[11] M. D. Collins, "A split-step pad solution for the parabolic equation method," *J. Acoust. Soc. Am.*, vol. 93, iss. 4, pp. 1736-1742, 1993.

[12] Z. He, Z. H. Fan, D. Z. Ding, and R. S. Chen, "A vector parabolic equation method combined with MLFMM for scattering from a cavity," *Applied Computational Electromagnetics Society Journal*, vol. 30, no. 5, pp. 496-502, 2015.

[13] Z. He, T. Su, and R. S. Chen, "Vector parabolic equation method for the scattering from PEC objects in half-space," *Applied Computational Electromagnetics Society Journal*, vol. 30, no. 8, pp. 877-883, 2015.

[14] R. Janaswamy, "Path loss predictions in the presence of buildings on flat terrain: A 3D vector parabolic equation approach," *IEEE Trans. Antennas Propag.*, vol. 51, no. 8, pp. 1716-1729, 2003.

[15] Z. He and R. S. Chen, "A vector meshless parabolic equation method for three-dimensional electromagnetic scatterings," *IEEE Transactions on Antennas and Propagation*, vol. 63, no. 6, pp. 2595-2603, 2015.

[16] Z. He, Z. H. Fan, and R. S. Chen, "Spectral element method based parabolic equation for EM scattering problems," *Waves in Random and Complex Media*, vol. 26, iss. 1, pp. 80-88, 2016.

[17] N. Bildik and G. Avci, "On the solution of Poisson equation by alternating group explicit iterative method," *Applied Mathematics and Computation*, vol. 166, no. 2, pp. 411-425, 2005.

[18] R. B. Kellogg, "An alternating direction method for operator equations," *SIAM J. Soc. Indust. Appl. Math.*, vol. 12, no. 4, pp. 848-854, 1964.

[19] Z. He and R. S. Chen, "A wide-angle ADI-PE method for EM scattering from electrically large targets," *Electromagnetics*, vol. 36, iss. 2, pp. 94-101, 2016.

[20] Z. He and R. S. Chen, "A novel parallel parabolic equation method for electromagnetic scatterings," *IEEE Transactions on Antennas and Propagation*, vol. 64, no. 11, pp. 4777-4784, 2016.

Shifei Tao was born in Anhui, China, in 1987. He received the B.Sc. degree in Communication Engineering and Ph.D. degree in EM Field and Microwave Technique from Nanjing University of Science and Technology (NUST), Nanjing, Jiangsu, China, in 2008 and 2014, respectively.

Since 2017, he has been with Nanjing University of Science and Technology, where he works as an Assistant Professor. From 2015 to 2016, he was a Postdoctoral Research Associate in Electric and Computer Engineering in Northeastern University, Boston, USA. His current research interests are in the computational electromagnetics, antennas, electromagnetic scattering and radiation.

Design, Modeling, and Numerical Characteristics of the Plasmonic Dipole Nano-Antennas for Maximum Field Enhancement

Thi Thanh Kieu Nguyen [1], Quang Minh Ngo [2], and Truong Khang Nguyen [3,4,*]

[1] Faculty of Engineering, Binh Thuan Province Vocational College, Binh Thuan, Vietnam

[2] Institute of Materials Science, Vietnam Academy of Science and Technology
18 Hoang Quoc Viet, Cau Giay, Hanoi, Vietnam

[3] Division of Computational Physics, Institute for Computational Science
Ton Duc Thang University, Ho Chi Minh City, Vietnam

[4] Faculty of Electrical and Electronics Engineering, Ton Duc Thang University, Ho Chi Minh City, Vietnam
*nguyentruongkhang@tdt.edu.vn

Abstract ─ In this paper, we investigate the near-field enhanced optical absorption and far-field radiation characteristics of plasmonic dipole nano-antenna with different geometries which are rectangular, square, circular, and ellipse dipoles. Localized E-field enhancement at the excitation gap and reflection profile in an infinite 2D array of each nano-antenna are characterized and optimized at the resonant frequency of 375 THz, which corresponds to the incident wavelength of 800 nm. Numerical results show that the ellipse nano-antenna produces the most enhanced electric field at the excitation gap whereas the circular nano-antenna yields the best reflection and far-field radiation characteristics. This research is useful for the researchers and designers in choosing appropriate plasmonic dipole nano-antennas when incorporating with a photoconductive antenna for terahertz radiation enhancement.

Index Terms ─ Absorption, far-field power pattern, localized electric field, nano-antenna, reflection, surface plasmon resonance.

I. INTRODUCTION

The interaction of light with plasmonic nano-structures has constituted a central research topic in current science and engineering and has been finding several interesting applications in nanophotonic technology [1–4]. Two main demands for existing and emerging nano-optical applications are an optical spot beyond the diffraction limit and a high transparent efficiency. Plasmonic nano-antennas can concentrate the excitation light beam based on the localized surface plasmon resonance and thus can be used in the nano-optical system because of their ability to obtain a very small optical spot. In addition, the enhanced intensity of light confinement into a high index substrate can be achieved by asymmetric scattering due to surface plasmon excited on metallic nanostructures. Consequently, plasmonic nano-antenna can provide high transmission efficiency for practical applications. Recent reports on applications of plasmonic nano-antennas include sensitive photodetection [5], plasmon-emitting diode [6, 7], photovoltaic devices [8], surface enhanced Raman spectroscopy [9], bio-sensing [10], terahertz photoconductive antenna [11–13], etc.

To maximize the field enhancement in the high field region of the optical nano-antenna, which is well-known as the most important parameter to characterize the performance of the nano-antenna, parameters such as antenna geometry, dielectric loading, as well as the polarization of incident light have to be carefully optimized and fined-tune [14, 15]. The optical properties of different types of nano-antennas for the enhancement of fluorescence of molecules have been discussed and demonstrated over the last decades [16–21]. However, a detailed comparison of nano-antennas having different geometries in term of near-field optical absorption and far-field radiation characteristics is still lack in the literature. Therefore, the aim of this paper is to provide such a detailed study and comparison. Four plasmonic dipole nano-antennas with different geometries are chosen for the study and comparison; they are rectangular dipole, square dipole, circular dipole, and ellipse dipole. Absorption and reflection profiles of each nano-antenna are characterized and optimized at the resonant frequency of 375 THz which corresponds to the incident wavelength of 800 nm. The paper is organized as follows: Section 2 presents the nano-antenna geometries and simulation approach; Section 3 presents the results and discussion; Section 4 gives a

conclusion.

II. GEOMETRY AND MODELLING OF THE NANO-ANTENNAS

Figure 1 shows the geometry of the four nano-antennas under examination in the side and top views. Both the four dipoles and the ground are made of gold. The dipole nano-antenna and the ground are separated by a SiO$_2$ substrate which having a thickness of T. The widths and the lengths of the rectangular dipole are designated as W_R and L_R, while those of the square dipole are W_S and L_S, those of the circular dipole are W_C and L_C, and those of the ellipse dipole are W_E and L_E, respectively. The SiO$_2$ thicknesses of each nano-antenna are denoted as T_R, T_S, T_C, T_E whereas the periodicities of each nano-antenna in their arrays are denoted as P_R, P_S, P_C, P_E for the rectangular, square, circular, and ellipse dipoles, respectively. The excitation gap and the gold metal thickness of each nano-antenna are g and $T_{Au} = 25$ nm, respectively. Design parameters of the four antennas for the optimized localized E-field and reflection coefficient at the desired frequency of 375 THz are as follows: for the rectangular dipole ($g = 10$ nm, $W_R = 35$ nm, $L_R = 174$ nm, $T_R = 100$ nm, $P_R = 550$ nm); for the square dipole ($g = 10$ nm, $W_S = 78$ nm, $L_S = 166$ nm, $T_S = 40$ nm, $P_S = 600$ nm); for the circular dipole ($g = 10$ nm, $W_C = 94$ nm, $L_C = 198$ nm, $T_C = 60$ nm,

$P_C = 590$ nm); for the ellipse dipole ($g = 10$ nm, $W_E = 40$ nm, $L_E = 190$ nm, $T_E = 70$ nm, $P_E = 570$ nm).

In this paper, a full-wave electromagnetic simulator Microwave Studio by CST based on Finite Integration Technique (FIT) was used to analyze the characteristics of the nano-antennas [22]. Figure 2 (a) shows the model to study the localized E-field response at the excitation gap of the dipoles in which the excitation source is a plane wave incident from the top with an electric field amplitude of 1 V/m and with a polarization along the main axis, i.e., x-axis, of the nano-antennas. To detect the localized E-field, a probe was placed in the gap between the dipole arms and oriented along the x-axis. This simulation model also allows calculating the far-field power patterns of the nano-antennas. The transmission/reflection coefficient of the nano-antenna was studied by using a unit cell model that employed a two-Floquet-port model with electric and magnetic boundary conditions enforced along the $\pm x$ and $\pm y$ directions, seen in Fig. 2 (b). The Au metal and SiO$_2$ substrates used in the simulation can be defined in the material library of the CST MWS software. Figure 3 shows the electric dispersion curves of Au and SiO$_2$ within the frequency range of interest, i.e., 200 THz - 500 THz which these close to the measured values in the previously reported studies [23, 24].
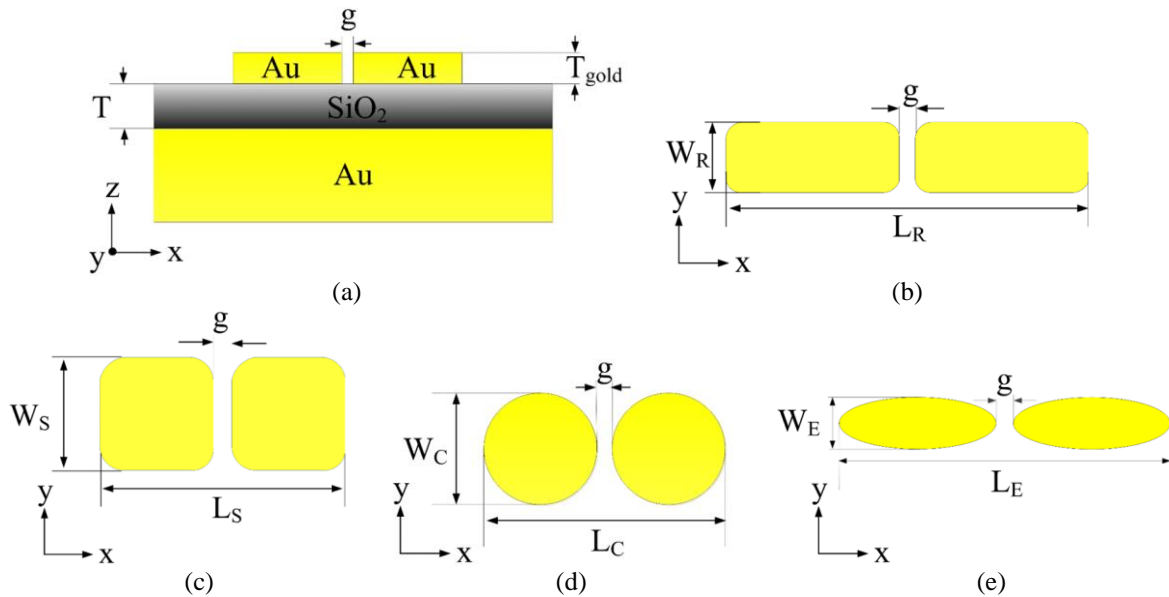

Fig. 1. (a) Side view of the nano-antennas; (b-e) geometries of the rectangular dipole, square dipole, circular dipole, and ellipse dipole.
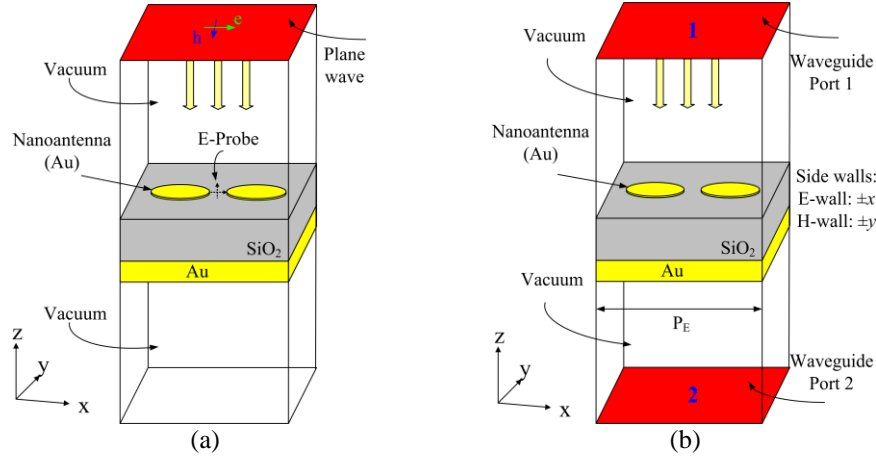
Fig. 2. Simulation models: (a) to calculate the localized E-field and far-field power pattern, and (b) to calculate the reflection coefficient of an infinite 2D array.
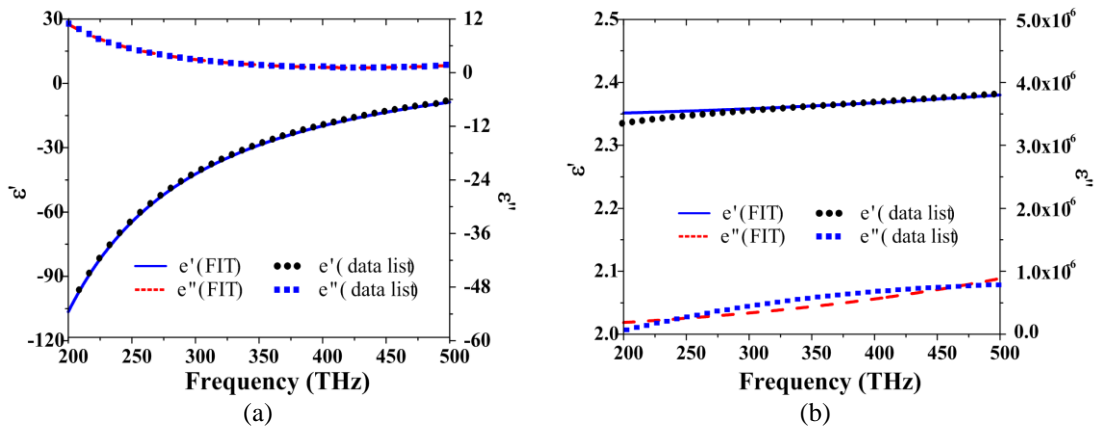

Fig. 3. Dispersion curves of: (a) gold and (b) SiO$_2$ in the frequency of interest from 200 THz to 500 THz.

III. RESULTS AND DISCUSSION

We select the ellipse dipole nano-antenna to investigate the frequency response on the design parameters (g, T_E, L_E, and P_E) since other three nano-antennas was observed to behave identically. It is noted that in this parameter study, one parameter was varied whereas others were fixed. In addition, hereinafter F_{peak} denotes the frequency where occurring the maximum localized electric field E_{peak}. Figure 4 (a) shows that the excitation gap, g, strongly influences the electric field confinement. The narrower the g is, the lower the resonant frequency occurred, and the significantly better the localized E_{peak} presented. Maximum E_{peak} could reach to approximately 400 V/m when g decreases to 7 nm. For the optimized design, we chose $g = 10$ nm because of the two reasons: first, if $g = 10$ nm, the resonant frequency occurring the maximum E_{peak} was mostly close to the desired frequency of 375 THz; second, if g is so small, we would encounter a short circuit problem after the fabrication process. Figure 4 (b) shows that when the thickness of the SiO$_2$ layer T_E

changed, both F_{peak} and E_{peak} significantly changed, and clearly demonstrated a resonance behavior. When T_E increased from 20 nm to 100 nm with a step of 20 nm, F_{peak} increased, reached a maximum value, and then decreased and similarly for E_{peak}. At $T_E = 70$ nm, F_{peak} was mostly close to the desired frequency of 375 THz, and E_{peak} reached the maximum value. This behavior is interesting, which was proven in [14] and said that the distance from the nano-antenna to the reflective surface (Au ground) must be selected to satisfy the resonance condition if we consider the SiO$_2$ substrate layer as an Fabry-Perot resonator cavity.

Figure 4 (c) shows that when L_E increased, F_{peak} decreased, which follows the theory that the antenna length is inversely proportional to its operating frequency. We can calculate the effective wavelength according to the formula as:

$$\lambda_{eff} = \frac{\lambda_0}{\sqrt{\varepsilon_{eff}}} = \frac{c}{f_0 \sqrt{\varepsilon_{eff}}}, \qquad (1)$$

where c is the speed of light (3×10^8 m/s), f_o is the

resonant frequency (~ 375 THz), and ε_{eff} the effective dielectric constant of SiO_2 (~ 2.4). Accordingly, the effective wavelength is approximately 510 nm. In theory, the antenna has a length of about a half of the effective wavelength ($L_{total} \sim \lambda_{eff}/2 \sim 260$ nm) will present the first resonance mode. The resulted nano-antenna length in our simulation is approximately of 200 nm which is shorter than the theoretically predicted length. This can be attributed to an increase of the effective permittivity of the whole structure due to the presence of the reflecting mirror Au. When we consider the localized E-field, the total length of the nano-antennas also influenced the E_{peak}. The value of $L_E = 190$ nm exhibited the maximum E_{peak} of 150 V/m at the F_{peak} of 374 THz. Figure 4 (d) shows that if the width P_E of the SiO_2 layer, i.e., the periodicity in a 2D infinite array, increased, the resonant

frequency decreased, however E_{peak} at the gap increased. The increased width of the semiconductor layer resulted in an increase of the effective permittivity of the whole structure. For the desired resonant frequency around the 375 THz, P_E was chosen to be 570 nm. It can be seen that this parameter is the least influence factor on either E_{peak} or F_{peak}. By investigating the design parameter study of the ellipse geometry, we can conclude that the excitation gap area significantly influenced the localized E-field, while the dipole length decided the resonant frequency of the nano-antennas. More importantly, the thickness of the semiconductor layer must be appropriately chosen to obtain the additional E-field enhancement thanks to the mechanism similar to a Fabry-Perot resonant cavity. These characteristics are identical for the rectangular, square, and circular dipoles.
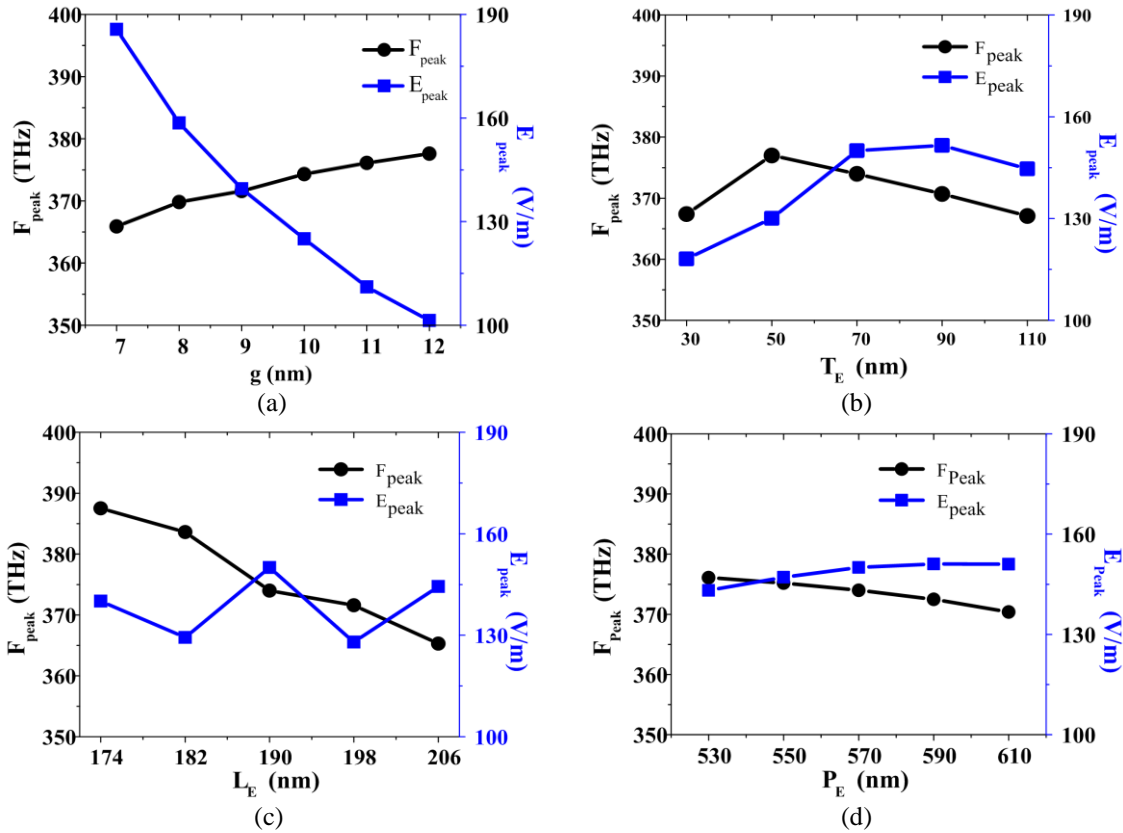

Fig. 4. Parameter study in terms of F_{peak} and E_{peak} of the ellipse dipole: (a) gap between dipole arms, (b) SiO_2 thickness, (c) total dipole length, and (d) lateral size of the SiO_2 substrate.

Figure 5 shows the localized E-field checked at the excitation gap, and the reflection coefficient checked for a 2D infinite array of the four nano-antennas. The optimized results show that the localized E-field of the rectangular dipole was 110.3 V/m at 374.9 THz, while that of the square dipole was 92.2 V/m at 372.8 THz, that of the circular dipole was 125 V/m at 374.3 THz, and that of the ellipse dipole was 150 V/m at 374 THz,

seen in Fig. 5 (a). It should be noted that the incident E-field was chosen of 1 V/m. All the four nano-antennas produced a significantly enhanced localized E-field at the gap between the dipole arms. The ellipse dipole produced the highest localized E-field while the square dipole presented the lowest value. In the perspective of the reflection coefficient, the behavior was different. The reflection coefficient of the rectangular dipole was

about 0.19 whereas that of the square dipole, circular dipole and ellipse dipole were about 0.28, 0.11, and 0.25, respectively, seen in Fig. 5 (b) (refer to Table 1). Therefore, the circular dipole produced the best reflection characteristic while the square dipole presented the worst case. It is obvious that the resonant frequency F_{peak}, the frequency occurring E_{peak}, almost coincided with the frequency occurring the minimum reflection coefficient. This indicates that the four nano-antenna structures operate well at the desired frequency of 375 THz and thereby maximizing the incident light absorption efficiency.

Figures 6 and 7 respectively present the near-field distribution and the far-field power patterns of the four

nano-antennas at their resonant frequencies. The field was mostly distributed in the excitation gaps and at the dipole ends as in a conventional RF dipole. It is obvious that the circular dipole exhibited the best power patterns with the least back radiation in comparison with the three remains. Generally, the ellipse dipole nano-antenna produces the best localized E-field enhancement at the excitation gap whereas the circular dipole nano-antenna yields the best reflection and far-field radiation characteristics. In other words, the circular nano-antenna should be chosen regarding the far-field radiated power while the ellipse nano-antenna should be chosen for the demand of highly localized E-field.
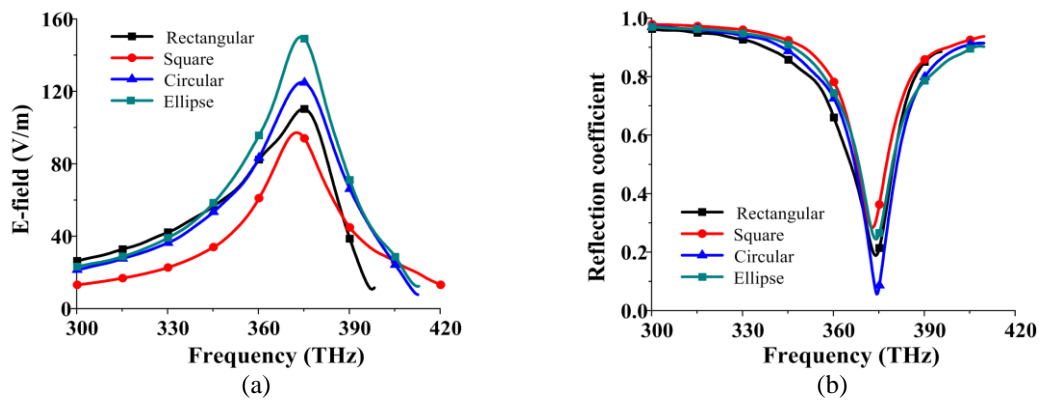

Fig. 5. (a) Localized E-field and (b) reflection coefficient as a function of frequency of the four nano-antennas.
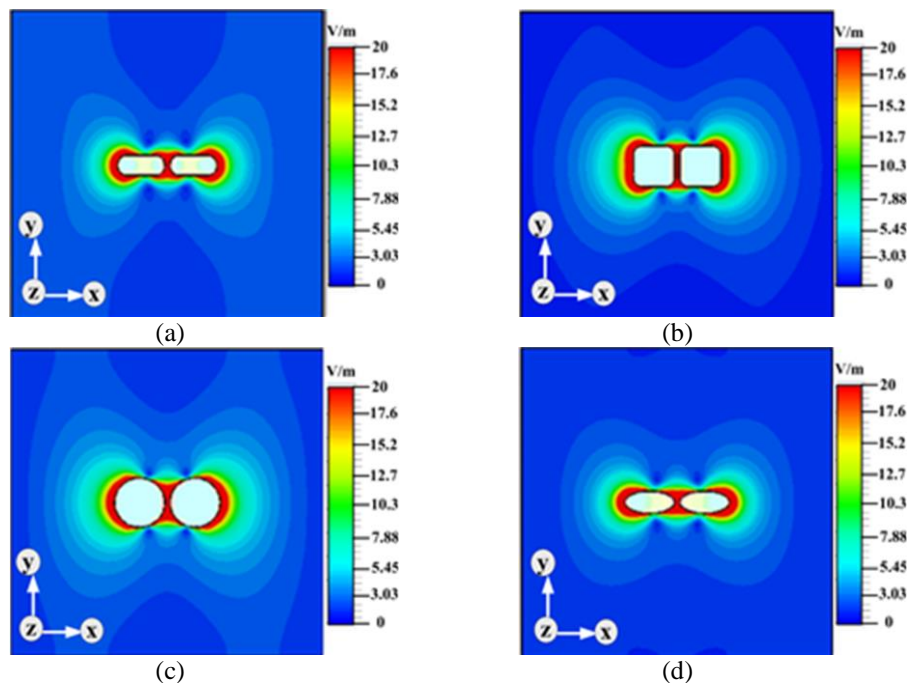

Fig. 6. Field distributions checked at the resonant frequencies of the four nano-antennas: (a) rectangular, (b) square, (c) circular, and (d) ellipse dipoles. The resonant frequencies for each nano-antenna can be refered in Table 1.
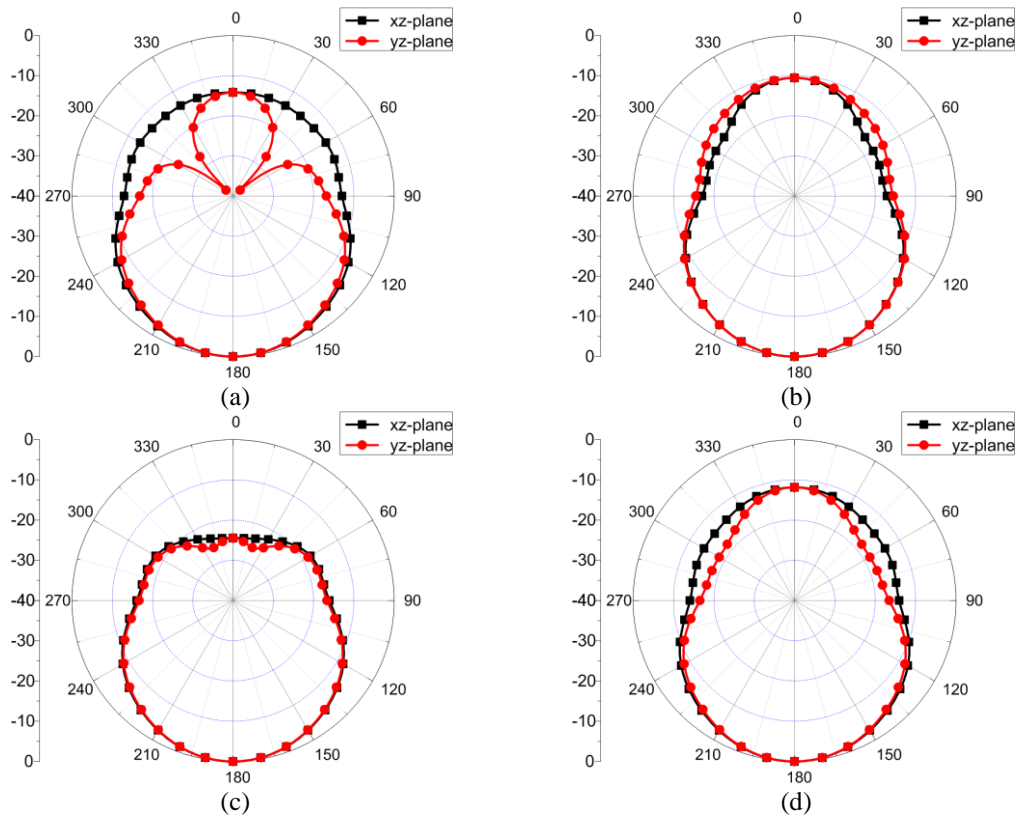
Fig. 7. Normalized far-field E-patterns calculated at the resonant frequencies of the four nano-antennas: (a) rectangular, (b) square, (c) circular, (d) ellipse dipoles. The resonant frequency for each nano-antenna can be referred in Table 1.

Table 1: Optimized results of the four nano-antennas

Geometry	Resonant Frequency F_{peak} (THz)	Localized E-field E_{peak} (V/m)	Reflection Coefficient
Rectangular	374.9	110.3	0.19
Square	372.8	92.2	0.28
Circular	374.3	125.0	0.11
Ellipse	374	150	0.25

IV. CONCLUSION

We have investigated and compared the performance of plasmonic nano-antennas for different geometries such as rectangular, square, circular, and ellipse dipoles. The excitation gap area significantly influenced the localized E-field enhancement, while the dipole length decided the resonant frequency of the nano-antennas. More importantly, the thickness of the semiconductor layers must be appropriately chosen to obtain the additional E-field enhancement thanks to the mechanism similar to a Fabry-Perot resonant cavity. The optimized results show that the ellipse dipole exhibits its outstanding performance regarding the localized E-field enhancement, whereas the circular dipole yields its outstanding performance in terms of the reflection coefficient and the far-field power pattern. This study could be useful for the incorporation of an array of such plasmonic nano-antennas at the active area of

photomixer/photoconductive antenna for an efficiency improvement.

REFERENCES

[1] C. Zhou, Y. Fainman, and Y. Sheng, "Applications of nano-optics," *Appl. Opt.*, vol. 50, no. 31, pp. N1-NO1, 2011.

[2] J. Wei, *Nonlinear Super-Resolution Nano-Optics and Applications*. Springer, 2015.

[3] A. Fratalocchi, C. M. Dodson, R. Zia, P. Genevet, E. Verhagen, H. Altug, and V. J. Sorger, "Nano-optics gets practical," *Nat. Nanotechnol.*, vol. 10, no. 1, pp. 11-15, 2015.

[4] J. Chao, Y. Lin, H. Liu, L. Wang, and C. Fan,

"DNA-based plasmonic nanostructures," *Mater. Today*, vol. 18, no. 6, pp. 326-335, 2015.

[5] C. Chakraborty, R. Beams, K. M. Goodfellow, G. W. Wicks, L. Novotny, and A. N. Vamivakas, "Optical antenna enhanced graphene photo-detector," *Appl. Phys. Lett.*, vol. 105, no. 24, p. 241114, 2014.

[6] D. M. Koller, A. Hohenau, H. Ditlbacher, N. Galler, F. Reil, F. R. Aussenegg, A. Leitner, E. J. W. List, and J. R. Krenn, "Organic plasmon-emitting diode," *Nat. Photonics*, vol. 2, no. 11, pp. 684-687, 2008.

[7] M. S. Eggleston, K. Messer, L. Zhang, E. Yablonovitch, and M. C. Wu, "Optical antenna enhanced spontaneous emission," *Proc. Natl. Acad. Sci.*, vol. 112, no. 6, pp. 1704-1709, 2015.

[8] S.-K. Kim, X. Zhang, D. J. Hill, K.-D. Song, J.-S. Park, H.-G. Park, and J. F. Cahoon, "Doubling absorption in nanowire solar cells with dielectric shell optical antennas," *Nano Lett.*, vol. 15, no. 1, pp. 753-758, 2014.

[9] I. Maouli, A. Taguchi, Y. Saito, S. Kawata, and P. Verma, "Optical antennas for tunable enhancement in tip-enhanced Raman spectroscopy imaging," *Appl. Phys. Express*, vol. 8, no. 3, p. 32401, 2015.

[10] A. Singh, J. T. Hugall, G. Calbris, and N. F. van Hulst, "Fiber-based optical nanoantennas for single-molecule imaging and sensing," *J. Light. Technol.*, vol. 33, no. 12, pp. 2371-2377, 2015.

[11] S.-G. Park, K. H. Jin, M. Yi, J. C. Ye, J. Ahn, and K.-H. Jeong, "Enhancement of terahertz pulse emission by optical nanoantenna," *ACS Nano*, vol. 6, no. 3, pp. 2026-2031, 2012.

[12] M. Jarrahi, "Advanced photoconductive terahertz optoelectronics based on nano-antennas and nano-plasmonic light concentrators," *Terahertz Sci. Technol. IEEE Trans.*, vol. 5, no. 3, pp. 391-397, 2015.

[13] A. Jooshesh, V. Bahrami-Yekta, J. Zhang, T. Tiedje, T. E. Darcie, and R. Gordon, "Plasmon-enhanced below bandgap photoconductive terahertz generation and detection," *Nano Lett.*, vol. 15, no. 12, pp. 8306-8310, 2015.

[14] H. Fischer and O. J. F. Martin, "Engineering the optical response of plasmonic nanoantennas," *Opt. Express*, vol. 16, no. 12, pp. 9144-9154, 2008.

[15] T. J. Seok, A. Jamshidi, M. Kim, S. Dhuey, A. Lakhani, H. Choo, P. J. Schuck, S. Cabrini, A. M. Schwartzberg, and J. Bokor, "Radiation engineering of optical antennas for maximum field enhancement," *Nano Lett.*, vol. 11, no. 7, pp. 2606-2610, 2011.

[16] F. J. González and G. D. Boreman, "Comparison of dipole, bowtie, spiral and log-periodic IR antennas," *Infrared Phys. Technol.*, vol. 46, no. 5, pp. 418-428, 2005.

[17] E. G. Mironov, Z. Li, H. T. Hattori, K. Vora, H. H. Tan, and C. Jagadish, "Titanium nano-antenna for high-power pulsed operation," *Light. Technol. J.*, vol. 31, no. 15, pp. 2459-2466, 2013.

[18] I. S. Maksymov, I. Staude, A. E. Miroshnichenko, and Y. S. Kivshar, "Optical Yagi-Uda nanoantennas," *Nanophotonics*, vol. 1, no. 1, pp. 65-81, 2012.

[19] E. G. Mironov, A. Khaleque, L. Liu, I. S. Maksymov, and H. T. Hattori, "Enhancing weak optical signals using a plasmonic Yagi-Uda nanoantenna array," *Photonics Technol. Lett. IEEE*, vol. 26, no. 22, pp. 2236-2239, 2014.

[20] D. K. Kotter, S. D. Novack, W. D. Slafer, and P. J. Pinhero, "Theory and manufacturing processes of solar nanoantenna electromagnetic collectors," *J. Sol. Energy Eng.*, vol. 132, no. 1, p. 11014, 2010.

[21] Z. Li, H. T. Hattori, and E. G. Mironov, "Charnia-like broadband plasmonic nano-antenna," *J. Mod. Opt.*, vol. 60, no. 10, pp. 790-796, 2013.

[22] CST Microwave Studio, CST GmbH, 2016. http://www.cst.com

[23] P. B. Johnson and R. W. Christy, "Optical constants of the noble metals," *Physical Review B*, vol. 6, Article ID 4370, 1972.

[24] E. Palik, *Handbook of Optical Constants of Solids*. vol. 1, Academic, New York, NY, USA, 1985.

Thi Thanh Kieu Nguyen received the B.S. degree in Computational Physics from Dalat University, Dalat City, Vietnam in 2008, and the M.S. degree in Radio Physics and Electronics – Engineering Physics from the University of Science, Vietnam National University, Ho Chi Minh City in 2015. She is currently Lecturer in Engineering Department, Binh Thuan Province Vocational College, Binh Thuan, Vietnam.

Quang Minh Ngo received the B.S. degree in Information and Communication Technology from Hanoi University of Science and Technology and the MSc. degree in Electronics and Telecommunications from VNU University of Engineering and Technology, Hanoi, Vietnam, in 2000 and 2005, respectively. In 2006, he was awarded the BK21 Doctoral Scholarship to study Electrical Engineering (Photonics) in the Nanophotonics

group at the Department of Electrical and Computer Engineering, Ajou University, Suwon, Korea where he received the Ph.D. degree on Feb. 2011. From Sep. 2000 until now, he is a Permanent Researcher of Institute of Materials Science (IMS), Vietnam Academy of Science and Technology (VAST), Hanoi, Vietnam. Since Mar. 2012, he has worked as a Leader of Micro- and Nano-Photonic Research Group at IMS. From Nov. to Dec. 2013, he worked at the Institute of Electronic Fundamental, Paris-Sud University, Orsay, France as a Visiting Professor. From Sep. 2014 to Sep. 2015 and from Feb. 2016 to Feb. 2017, he was a Visiting Scholar of Vietnam Education Foundation at the Department of Physics, Applied Physics and Astronomy, State University of New York at Binghamton, NY, United States and at the Department of Electrical and Electronic Engineering, University of Bristol, Bristol, United Kingdom, respectively. His research interests lie in understanding the theory, simulation and experiment of micro- and nano-photonic structures in the visible and near infrared spectral regions for optical devices, focused on the photonic crystals, plasmonics, and metamaterials. He serves as an active Reviewer for international journals including IEEE/OSA Journal of Lightwave Technology, Journal of Optical Society of America A (and B), Applied Optics, Journal of Applied Physics, Applied Physics Letters.

Truong Khang Nguyen received the B.S. degree in Computational Physics from the University of Science, Vietnam National University, Ho Chi Minh City in 2006, and the M.S. and Ph.D. degrees in Electrical and Computer Engineering from Ajou University in Suwon, Korea in 2013. From Oct. 2013 to Dec. 2014, he worked at Division of Energy Systems Research, Ajou Univerisity, Korea as a postdoctoral fellow. He is currently Head of Division of Computational Physics at Institute for Computational Science, Ton Duc Thang University in Ho Chi Minh City, Vietnam. He has written one chapter book in the area of THz antenna and filed one patent on THz stripline antenna. He serves as a Reviewer for international journals including Journal of Infrared, Millimeter, and Terahertz waves, Journal of Electromagnetic Waves and Applications, Progress in Electromagnetic Research, etc. He was awarded by Central Committee of the Vietnamese Student Association in 2012 and by Vietnamese Embassy in Korea in 2013 for Vietnamese Student in Korea with excellent research achievements. His current research interests include the design and analysis of microwave, millimeter-wave, terahertz wave, and nano-structured antennas.